

Figure 37.4. (A) An EELS spectrum displayed in logarithmic intensity mode. The zero loss is an order of magnitude more intense than the low-energy-loss portion, which is itself many orders of magnitude more intense than the small ionization edges, identified in the high-energy-loss range. The spectra can be acquired (B) serially or (C) in parallel. In serial collection, each of the energy channels accumulates counts for a given dwell time τ (typically 100 ms) before the next channel (energy range) is selected. In parallel collection, the complete spectrum is gathered simultaneously in all the available channels.

- A plastic scintillator located directly behind the slit receives an electron flux in time τ .
- The integrated electron current is converted to photons and amplified by a photomultiplier (PM) tube.

- After each dwell time, the total signal from the PM is then assigned to a channel corresponding to a specific energy loss, E , in a multichannel analyzer (MCA).

We've already discussed scintillator-PM systems of the sort used for SE detection in the SEM or STEM, or direct beam (BF) detectors in the STEM (see Chapter 7).

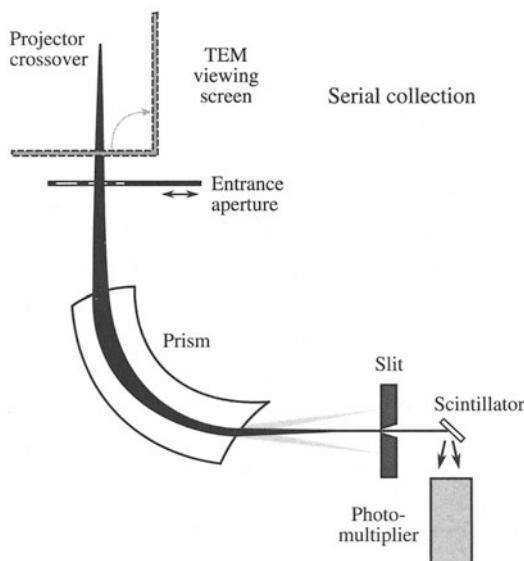
- They have a tremendous gain and therefore can handle a large intensity range.
- They show a rapid response to intensity changes and exhibit both low noise and a high detective quantum efficiency, or DQE.

The DQE is close to 1 under ideal conditions, although the absolute DQE of SEELS is very low (≈ 0.001) since most of the electrons are wasted at any single acquisition time. These factors are particularly important in EELS, because the spectrum intensity can vary by many orders of magnitude. However, the susceptibility of scintillators to beam damage also means that the intense low-energy part of the EELS spectrum can be a health danger to the scintillator. The Gatan systems give an unmistakable audible warning when the electron flux is too great. Even with careful operation the plastic scintillator in your SEELS will become damaged and, as a wise precaution, you should replace it every few months.

The spectrum display is built up in a serial manner, as we showed in Figure 37.4B. Typically, the MCA will have 1024 or 2048 channels. The display resolution can be selected from < 0.1 eV/channel to about 10 eV/channel, depending on how much of the spectrum you want to gather. For example, if you set the display resolution to 1 eV per channel, the entire EELS signal out to 1024 eV energy loss will be recorded. But even if you choose a short τ , e.g., 100 ms, it will still take you about 100 s to accumulate a full spectrum out to 1024 eV, and in 100 ms the total intensity in each channel is going to be small. In particular, the limited energy range that may be of interest to you will only have been sampled for a few seconds at best. So when you know what portion of the spectrum is of interest, you should restrict collection to fewer channels for a longer τ , or accumulate several spectra and add the intensities together in order to get satisfactory counting statistics across the full spectrum. We'll see later that you can influence the total intensity by your choice of operating mode.

During acquisition of a spectrum, the intensity changes by several orders of magnitude (see Figure 37.4A), and usually we are interested primarily in the low-intensity (high-energy-loss) part of the spectrum. Therefore, we have

A



B

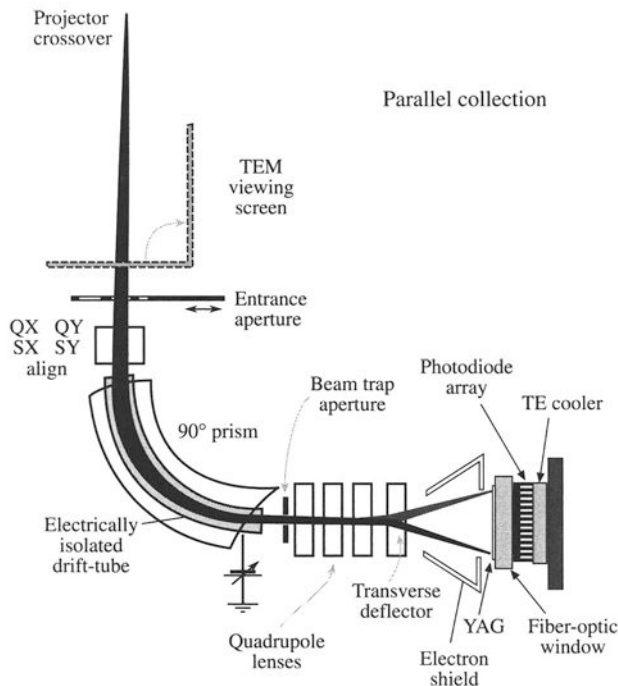


Figure 37.5. Comparison of EELS acquisition modes. (A) Serial collection of the spectrum through a slit onto a scintillator-PM system. (B) Parallel collection onto a YAG scintillator fiber-optically coupled to a thermoelectrically cooled (TE) semiconductor diode array. (Q = quadrupole, S = sextupole)

to change the display scale during SEELS spectrum collection in order to present a visible display of the low-intensity part of the spectrum. We can do this in one of two ways: either we increase τ by a factor of 10–100, or we electronically increase the gain of the scintillator-PM system by

some orders of magnitude and operate it in two different modes, as explained below.

For very high electron fluxes encountered in the zero-loss and low-energy-loss portion of the spectrum, we use “analog collection.” The total voltage generated at the exit of the PM can be related directly to the total electron current incident on the scintillator. Using a voltage-to-frequency (V/F) converter, this voltage is converted to a pulse that can be fed directly to the computer display. By changing the gain of the V/F converter we can handle electron fluxes in excess of $10^{10}/\text{s}$ (about 1 nA) with no problem. At this kind of incident current, the individual pulses overlap and are all integrated to give a continuous output. At the high-energy-loss end of the spectrum, where electron intensity is very low, the collection system can be changed to count the photon bursts generated by each electron, and this is termed “single-electron counting.” You throw a switch on the SEELS electronics control panel to change the detection mode at a given point (energy loss) in the serial collection, or you can change modes under software control, usually at the same energy in the spectrum where the display gain change occurs.

We will see that it is sometimes essential to record the spectrum over a wide range, say from zero to several hundred eV loss. In this case, the intense low-loss region must be gathered and displayed in the same spectrum as the less-intense high-loss region. A potential problem in this situation is that, even if the intense low-loss region does not physically damage the detector, it may cause it to glow and the glow persists for some time after the electrons hit the scintillator. So it is possible that while you are gathering the low-intensity part of the spectrum, the afterglow will contribute unwanted noise.

To avoid the afterglow, you should acquire all SEELS spectra in reverse-scan fashion. Start at the high loss, then go to the low-loss region, and finish at zero.

If the zero-loss peak is not required, then it is good practice to cease acquisition at about 5–10 eV to save the scintillator from the accumulated effects of high electron fluxes.

37.3.B. Parallel Collection

PEELS gathers the whole energy spectrum simultaneously and is much more efficient than SEELS. PEELS comprises a YAG scintillator coupled via fiber optics to a semiconductor photodiode array in the dispersion plane of the spectrometer, as shown in Figure 37.5B. The array consists of

1024 electrically isolated and thermoelectrically cooled silicon diodes, each about 25 μm across. These diode arrays show varying responses and exhibit specific artifacts, which we'll discuss in the next chapter.

The resultant spectrum accumulates across the whole energy range simultaneously, as we showed schematically back in Figure 37.4C. Rather than having a dwell time as in SEELS, we now have an integration time which can vary from a few msec to several hundred seconds. After integration, the whole spectrum is read out via an amplifier through an A/D converter and into an MCA system. Reasonable spectra can be acquired in a fraction of a second, making PEELS imaging a practical reality. We'll see more about this in Section 40.3.

The advantage of PEELS is that all regions of interest are gathered for the whole integration time, and not just some fraction of the acquisition time as in SEELS. Thus PEELS is much more efficient than SEELS, and its DQE is ~ 0.5 .

A quick warning: you can damage the YAG scintillator, particularly in intermediate-voltage microscopes. Ways to avoid this problem, especially for the intense zero-loss beam, are still being developed. Currently, the zero-loss beam intensity is attenuated or deflected off the scintillator if it is not required, or if the beam current exceeds 0.5 nA. While the SEELS system can handle intense signals, the PEELS diode array saturates at signal intensities of about 16,000 counts.

You must select an integration time that won't saturate the detector and then collect as many consecutive integrations as you need.

One other advantage of the PEELS system is that the scintillator shield is designed to act as a Faraday cup, and so you can use it to measure the total beam current. Usually, the beam is moved onto the shield whenever acquisition ceases, so a constant record of the beam current is available.

To summarize:

- SEELS detects one channel at a time; the detector is easy to optimize and simple to operate.
- PEELS detects the whole spectrum at one time, but the diode array is hard to optimize.
- PEELS exhibits artifacts, and has more complex electron optics, but is 2–3 orders of magnitude more efficient than SEELS with a relatively high DQE.

37.3.C. Spectrometer Dispersion

We define the dispersion as the distance in the spectrum (dx) between the positions of electrons differing by energy dE . It is a function of the strength of the magnetic field (which is governed by the strength (i.e., size) of the spectrometer magnet) and the energy of the incident beam, E_0 . In the commercial serial spectrometers, the radius of curvature (R) of electrons traveling on axis is about 200 mm, and for 100-keV electrons dx/dE is about 2 $\mu\text{m}/\text{eV}$. This dispersion, while small, is sufficiently large so as not to limit the energy resolution (see below). A serial-detection system can process the spectrum without any post-spectrometer magnifying lenses. For parallel collection this dispersion value is inadequate, and typically electrons with an energy range of about 15 eV would fall on each 25- μm -wide diode. Therefore, the dispersion plane has to be magnified $\sim 15\times$ before the spectrum can be detected with resolution closer to 1 eV. This magnification requires post-spectrometer lenses; 4 quadrupoles are used in the Gatan system. The dispersion should be linear across the diode array; you can check this by measuring the separation of a known pair of spectral features (e.g., zero loss and C K edge) as you displace the spectrum across the diode array.

You may wonder why we don't record the spectrum on film rather than collect it electronically. In fact, this was the first method used to detect electron spectra, but it is an analog method and photographic film does not have a linear response over the usual range of spectral intensities. Furthermore, the grain size of the photographic emulsion (10–20 μm) would limit energy resolution to about 5 eV unless the dispersion were increased, so photographic recording is no longer used.

37.3.D. Spectrometer Resolution

We define the energy resolution of the spectrometer as the FWHM of the zero-loss peak (see back in Figure 37.3). If you don't focus your spectrometer as we just described, then you won't get the best resolution. The best resolution you can get is determined by the type of electron source. As we discussed back in Chapter 5 (see Table 5.1), at ~ 100 keV a W source has the worst energy resolution (2.5 eV), and a LaB₆ is slightly better than W at 1.5 eV while a cold FEG gives the best value (0.3 eV). Because of the high emission current from thermionic sources, the energy resolution is in fact limited by electrostatic interactions between electrons at the filament crossover. This electron-electron interaction is called the Boersch effect. You can partially overcome this by undersaturating the filament and using only the electrons in the halo. Under these circumstances a LaB₆ source can attain a resolution below

1 eV, but at the expense of a considerable loss of signal, for which you can compensate by increasing the beam size and/or the C2 aperture.

The energy resolution decreases slightly as the energy loss increases, but it should be no worse than ~1.5 times the zero-loss peak width up to 1000-eV energy loss.

If you operate at higher voltage, you should also expect a degradation of energy resolution as the kV increases, approximately tripling from 100 kV to 400 kV.

Because the magnetic prism is so extremely sensitive, external magnetic fields in the microscope room may limit the resolution. You may see a disturbance to the spectrum directly if you sit in a metal chair and move around, or if you open metal doors into the TEM room. Remember, for comparison, that the energy resolution of XEDS is >100 eV.

For different EELS operations, different factors affect the resolution. In a SEELS system the resolution is most easily changed by adjusting the slit width. A larger slit width results in poorer energy resolution, but has the advantage of increasing the total current into the detection system. In a PEELS system optimum resolution requires a small projector crossover and a small (1 mm or 2 mm) entrance aperture. The resolution is degraded by choosing a larger entrance aperture because of off-axis beams; i.e., degradation is caused by a C_s effect for the lenses in the energy analyzing spectrometer. Similarly, the resolution may change as you deflect the zero-loss peak onto different regions of the photodiode, although this should not happen if the spectrometer optics are properly aligned.

37.3.E. Point-Spread Function

In a PEELS, you can reduce the magnification of your spectrum so that the zero-loss peak occupies only a single photodiode channel. Any intensity registered outside that single channel is an artifact of the detector system array and is called the point-spread function. This function acts to degrade the inherent resolution of the magnetic spectrometer. The zero-loss peak may spread on its way through the YAG scintillator and the fiber optics before hitting the photodiode. Figure 37.6 shows the point-spread function of a PEELS and clearly there is intensity well outside a single channel. This is important because this spreading broadens features in your spectrum, such as fine structure in ionization edges, and you need to remove it by deconvolution (see Section 39.6). The concept is essentially the same as the point-spread function we discussed for HRTEM.

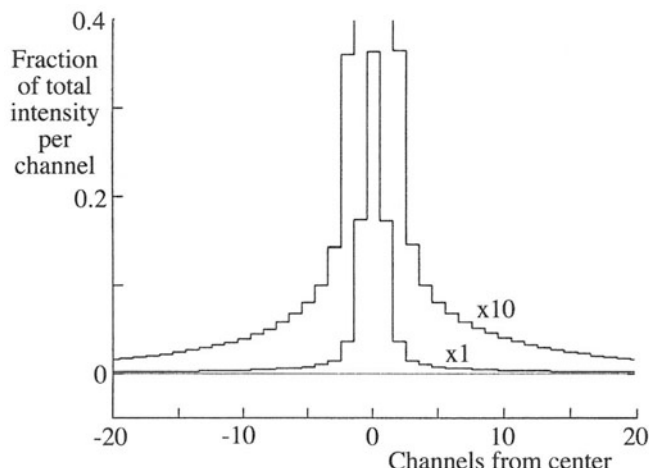


Figure 37.6. The point-spread function, showing the degradation of the intense well-defined zero-loss peak through spreading of the signal as it is transferred from the scintillator via the fiber-optic coupling to the photodiodes. The peak should occupy a single channel but is spread across several channels.

37.4. IMAGE AND DIFFRACTION MODES

When performing EELS in a TEM/STEM, you can operate in either of two modes, and the terminology for this is confusing. If you operate the TEM such that an image is present on the viewing screen, then the back focal plane of the projector lens contains a DP, and the spectrometer uses this pattern as its object. From the spectroscopists' viewpoint, therefore, this is termed "diffraction mode" or "diffraction coupling," but from the microscopists' viewpoint it is more natural to call this "image mode" since you are looking at an image on the screen. Conversely, if you adjust the microscope so a DP is projected onto the screen (which includes STEM mode in a TEM/STEM), then the spectrometer object plane contains an image, and the terminology is reversed.

The spectroscopist uses the term "image mode" or "image coupling" and the microscopist says "diffraction mode."

Both sets of terms appear in the literature, often without precise definition, so it can be rather confusing.

In this text "image mode" means an image is present on the TEM screen; i.e., we use the microscopists' terminology.

So your first step is to ensure that a focused image or DP is present on your TEM screen, and then the spectrum can be focused onto the dispersion plane.

37.4.A. Spectrometer Collection Angle

The collection semiangle of the spectrometer (β) is the most important variable in quantification, so you should know β for all your standard operating situations. If you do gather spectra with different β , it is difficult to make sensible comparisons without considerable post-acquisition processing. The detailed intensity variations in the spectrum depend on the range of electron scattering angles which are gathered by the spectrometer. Under certain circumstances, the effective value of β can be modified by the beam-convergence semiangle, α , but we'll discuss that when we talk about quantification in Chapter 39.

β is the semiangle subtended at the specimen by the entrance aperture to the spectrometer.

This definition is illustrated in Figure 37.7. The value of β is affected by the mode of microscope operation, and so we will describe how to measure β under different conditions that may be encountered.

Dedicated STEMs. In a basic DSTEM the situation is straightforward if there are no post-specimen lenses because, as shown in Figure 37.7, the collection angle can be calculated from simple geometry. Depending on the diameter (d) of the spectrometer entrance aperture and the distance from the specimen to the aperture (h), β (in radians) is given by

$$\beta \approx \frac{d}{2h} \quad [37.1]$$

This value is approximate and assumes β is small. Since h is not a variable, the range of β is controlled by the number and size of available apertures. Therefore, if h is ~ 100 mm, then for a 1-mm-diameter aperture, β is 5 mrad. If there are post-specimen lenses and apertures, the situation is similar to that in a TEM/STEM, as discussed below.

TEM-image mode. Remember that in image mode, a magnified image of the specimen is present on the viewing screen and the spectrometer object plane contains a DP. In contrast to what we just described for a dedicated STEM, the angular distribution of electrons entering the spectrometer aperture below the center of the TEM screen is *independent* of the entrance aperture size. This is because you can control the angular distribution of electrons contributing to any TEM image by the size of the objective aperture in the DP in the back focal plane of the objective lens. If you don't use an objective aperture, then the collection semiangle is very

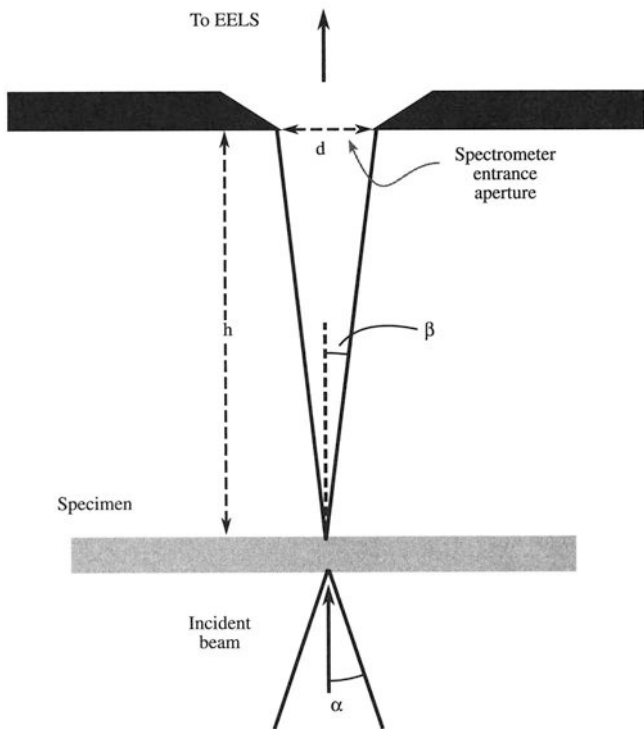


Figure 37.7. Schematic diagram showing the definition of β in a DSTEM in which no lenses exist between the specimen and the spectrometer entrance aperture.

large ($>\sim 100$ mrad) and need not be calculated accurately, because we'll see that small differences in a large β value do not affect the spectrum or subsequent quantification.

If, for some reason, you do wish to calculate β in image mode with no aperture inserted, you need to know the magnification of the DP in the back focal plane of the projector lens (which is the front focal plane of the spectrometer). This magnification may be described in terms of the camera length L of the DP, and this is given by

$$L \approx \frac{D}{M} \quad [37.2]$$

where D is the distance from the projector crossover to the recording plane and M is the magnification of the image in that plane. So if D is about 500 mm and the screen magnification is 10,000 \times , then L is 0.05 mm. Thus we can show that

$$\beta \approx \frac{r_0}{L} \quad [37.3]$$

where r_0 is the maximum radius of the DP in the focal plane of the spectrometer. Typically, r_0 is approximately 5 μm , and so β is 0.1 rads or 100 mrad which, as we just said, is so large that we rarely need to know it accurately. In fact, in TEM-image mode without an objective aperture,

if you just assume $\beta = 100$ mrad any calculation or quantification you do will be independent of β .

If you insert an objective aperture and you know its size and the focal length of the objective lens, then β can easily be calculated geometrically. To a first approximation, in a similar manner to equation 37.1 above, β is the objective aperture diameter divided by twice the focal length of the objective lens, as shown in Figure 37.8. For example, with a focal length of 3 mm and a 30- μm aperture, β is about 5 mrad.

If you insert an objective aperture, a normal BF image can be seen on the TEM screen and the information in the spectrum is related (with some considerable error) to the area of the image that sits directly above the spectrometer entrance aperture. We will return to this point in more detail in Section 37.4 when we discuss the spatial resolution of microanalysis. Remember also that with the objective aperture in, you cannot do XEDS. Therefore, simultaneous EELS and XEDS is not possible in this mode.

TEM/STEM diffraction mode. In diffraction (also STEM) mode, the situation is a little more complicated. Remember, the object plane of the spectrometer (the projector lens BFP) contains a low-magnification image of the specimen; so you see a DP on the screen and the same DP is in the plane of the spectrometer entrance aperture. Under these circumstances we control β by our choice of the spectrometer entrance aperture, as shown in Figure 37.9.

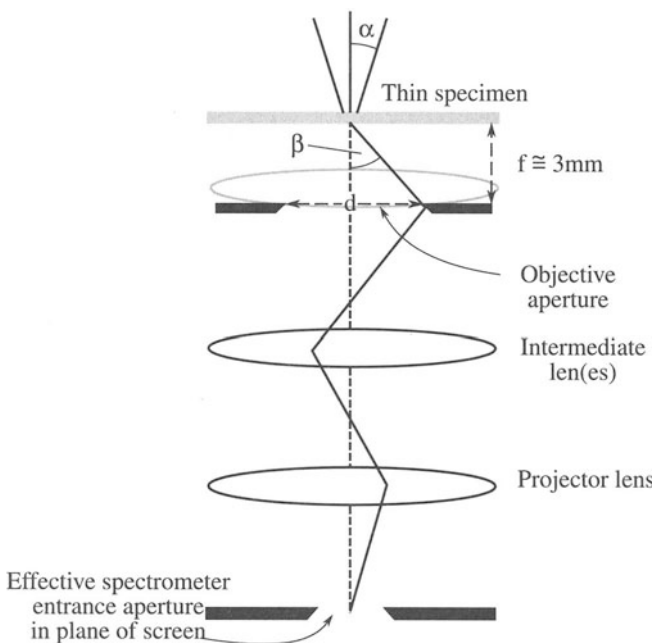


Figure 37.8. The value of β in TEM-image mode is governed by the dimensions of the objective aperture.

If a small objective aperture is inserted, it is possible that it may limit β ; the effective value of β at the back focal plane of the projector lens is β/M , where M is the magnification of the image in the back focal plane of the projector lens.

You have to calibrate β from the DP of a known crystalline specimen, as also shown in Figure 37.9. Knowing the size of the spectrometer entrance aperture, the value of β can be calibrated by twice the Bragg angle, $2\theta_B$, that separates the 000 spot and a known hkl disk. If the effective aperture diameter in the recording plane is d_{eff} and the distance b is related to the angle $2\theta_B$, as shown in Figure 5.8, so

$$\beta \approx \frac{d_{\text{eff}}}{2} \frac{2\theta_B}{b} \quad [37.4]$$

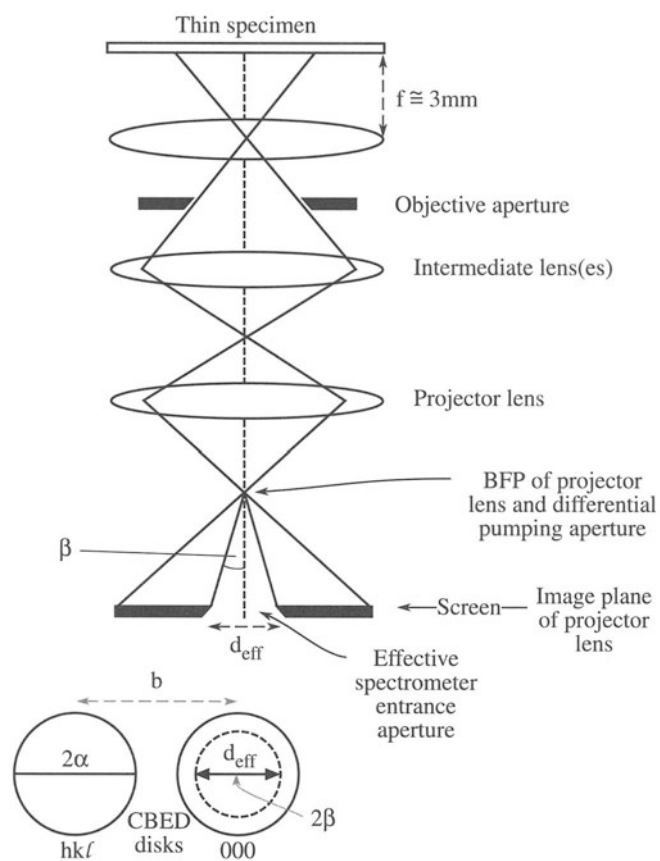


Figure 37.9. The value of β in TEM/STEM diffraction mode is determined by the effective diameter of the spectrometer entrance aperture (d_{eff}), projected into the plane of the diffraction pattern. The value of the d_{eff} can be calibrated by reference to a known diffraction pattern (below) in which d_{eff} can be related to $2\theta_B$.

The effective entrance aperture diameter d_{eff} at the recording plane is related to the actual diameter d by

$$d_{\text{eff}} = \frac{d D}{D_A} \quad [37.5]$$

where D is the distance from the projector crossover to the recording plane (remember, the film is not at the same height as the screen); D_A is the distance between the crossover and the actual entrance aperture. Alternatively, β can be determined directly if the camera length on the recording plane (L) is known, since

$$\beta = \frac{D d}{D_A L} \quad [37.6]$$

D_A is typically 610 mm for most Gatan PEELS systems, but D varies from microscope to microscope; you have control over d and L . For example, if D is 500 mm and L is 800 mm, then for the 5-mm entrance aperture, β is ~ 5 mrad.

If you choose a camera length such that the image of the specimen in the back focal plane of the spectrometer is at a magnification of $1\times$, then, in effect, you have moved the specimen to the object plane of the spectrometer. This special value of L is equal to the D , which you should know for your own microscope. Then β is simply the entrance aperture diameter divided by D_A (610 mm). Life will be much easier when all these calculations are incorporated in ELP (see Section 1.5).

In summary, the collection angle is a crucial factor in EELS. Large collection angles will give high intensity in the spectrum. If you collect your spectrum in image mode without an objective aperture, then you don't compromise your energy resolution. If you're in diffraction mode and you control β with the entrance aperture, then a large aperture (high intensity, large β) will degrade the energy resolution.

37.4.B. Spatial Selection

Depending on whether you're operating in image or diffraction mode, you obtain your spectrum from different regions of the specimen. In TEM-image mode, you position the area to be analyzed on the optic axis, above the spectrometer entrance aperture. The area selected is a function of the aperture size demagnified back to the plane of the specimen. For example, if the image magnification is 100,000 \times at the recording plane and the *effective* entrance aperture size at the recording plane is 1 mm, then the area contributing to the spectrum is 10 nm. So, you might think that you can do high-spatial-resolution microanalysis without a probe-forming STEM. However, if you're analyzing electrons that have suffered a significant energy loss, they may have come from areas of the specimen well away from

the area you selected, because of chromatic aberration. This displacement d is given by

$$d = \theta \Delta f \quad [37.7]$$

where θ is the angle of scatter, typically < 10 mrad, and Δf is the defocus error due to chromatic aberration given by

$$\Delta f = C_c \frac{E}{E_0} \quad [37.8]$$

where C_c is the chromatic aberration coefficient. So if we take a typical energy loss E of 284 eV (the energy required to eject a carbon K shell electron) and we have a beam energy of 100 keV, then the defocus due to chromatic aberration (with $C_c = 3$ mm) will be close to 10 μm , which gives an actual displacement, d , of 10^{-4} mm, or 100 nm. This figure is large compared to the value of 10 nm which we calculated without considering chromatic aberration effects.

While TEM-image mode is good for gathering spectra with a large β and high-energy resolution, the price you pay is poorer spatial resolution.

In TEM diffraction mode, you select the area of the specimen contributing to the DP in the usual way. You can either use the SAD aperture, which has a lower limit of about 5 μm , or you can form a fine beam as in STEM, so that a CBED pattern appears on the screen. In the latter case, the area you select is a function of the beam size and the beam spreading, but is generally < 50 nm wide. Therefore, this method is best for high-spatial-resolution microanalysis; just as for XEDS microanalysis, STEM operating mode is recommended for EELS microanalysis.

- Form an image in STEM mode.
- Stop the probe from scanning.
- Position it on the area to be analyzed.
- Switch on the EELS; in a TEM/STEM you have to lift up the TEM viewing screen also!

37.5. WHAT YOU NEED TO KNOW ABOUT YOUR PEELS

As with XEDS, where there are several standard tests you need to perform to determine that all is well with the detector and the electronics, there are similar tests for the PEELS diode array and electronics. Some of these are described in the Gatan handbook and others have been proposed by Egerton *et al.* (1993). We'll discuss specific artifacts visible in the spectrum in the next chapter.

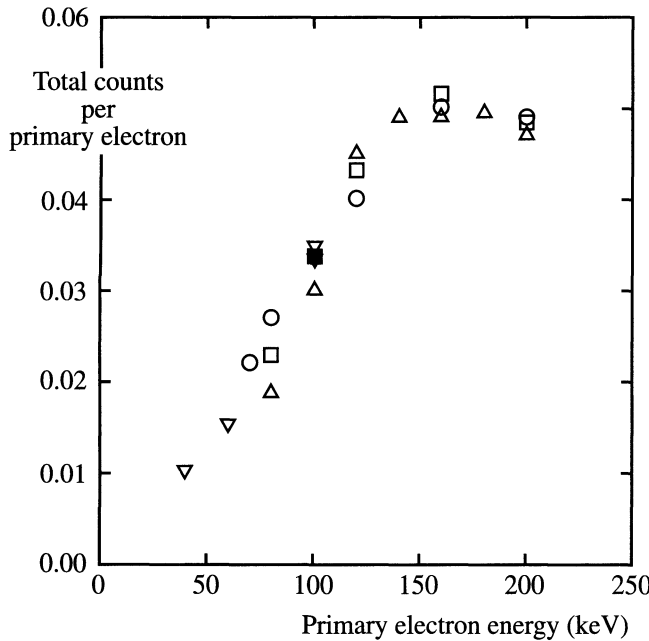


Figure 37.10. Nonlinear response of the diode array as a function of the beam energy. The response saturates at ~ 150 keV. Different symbols represent different dispersion settings.

Since increasing the keV means more electrons are generated in the scintillator, the sensitivity of the diode array should be linearly related to the electron energy. Egerton *et al.* (1993) have shown (see Figure 37.10) that, in fact, the Gatan diode-array response saturates at ~ 150 keV because of electron penetration. This nonlinearity doesn't affect quantification, since we typically make measurements over a very small energy range (< 1 keV), but it means that there is no gain in count rate by operating $> \sim 150$ keV. More important is the need for the YAG to respond linearly to different intensities incident on it; you should check that this is so by comparing the zero-loss intensity measured in a single 1-s readout with that recorded, say, in 40 readouts each of 0.025 s. In each case, you have to subtract the dark current (see Section 38.5). Obviously, the ratio of these two intensities should be unity for all levels of signal falling on the YAG. If it is not so, then you should consult the manufacturer.

37.6. IMAGING SPECTROMETERS

Two types of electron spectrometers are designed for energy-filtered imaging:

- In-column spectrometers on Zeiss 902 and LEO 912 series TEMs for “electron-spectroscopic imaging” (ESI).

- The Gatan Imaging Filter (GIF), which is a variation of the magnetic prism spectrometer.

Zeiss first used a mirror-prism system originally devised by Castaing and Henry (1962) and described by Zanchi *et al.* (1982). The drawback to the mirror-prism is the need to split the high-tension supply and raise the mirror to the same voltage as the gun. So LEO now use a magnetic omega (Ω) filter (Lanio *et al.* 1986). The Ω filter disperses the electrons in the column, as shown in Figure 37.11A. The spectrometer is placed in the TEM column between the intermediate and the projector lenses. Usually, you project an image into the prism, which is focused on a DP in the back focal plane of the intermediate lens. Therefore, the entrance aperture to the spectrometer selects an area of the specimen and the angle of collection is governed by the objective aperture (i.e., the same as image mode for the magnetic prism spectrometer). Electrons following a particular path through the spectrometer can be selected by the post-spectrometer slit. Thus only electrons of a given energy range, determined by the slit width, are used to form the image projected onto the TEM screen. ESI has several advantages over conventional TEM images, as we'll see in Section 40.3. We will also see then that the magnetic prism, which is primarily used for spectrometry, can also be used in a STEM to form energy-filtered images.

You can also change the microscope optics and project a DP into the prism, thus producing an energy-filtered DP on the TEM screen. Then, if you use the slit to select a portion of the DP, you get an energy-loss spectrum showing not only the intensity distribution as a function of energy but also the angular distribution of the electrons.

The GIF (Krivanek *et al.* 1992) shown in Figure 37.11B is basically a PEELS with an energy-selecting slit after the magnet and a two-dimensional slow scan CCD array detector rather than a single line of diodes. There are also more quadrupoles and sextupoles in the optics of the GIF. The first two quadrupoles before the slit increase the dispersion of the spectrometer onto the slit and the quadrupoles after the slit have two functions. Either they project an image of the spectrum at the slit onto the CCD, or they compensate for the energy dispersion of the magnet and project a magnified image of the specimen onto the CCD (which has advantages over the diode array in a conventional PEELS). In the first mode, the system is operating like a standard PEELS; in the second, it produces images (or DPs) containing electrons of a specific energy selected by the slit. Obviously, such a large number of variable sextupoles and quadrupoles could be a nightmare to operate without appropriate computer control, and this is built into the system. We'll describe energy filtering with the GIF in Section 40.3.

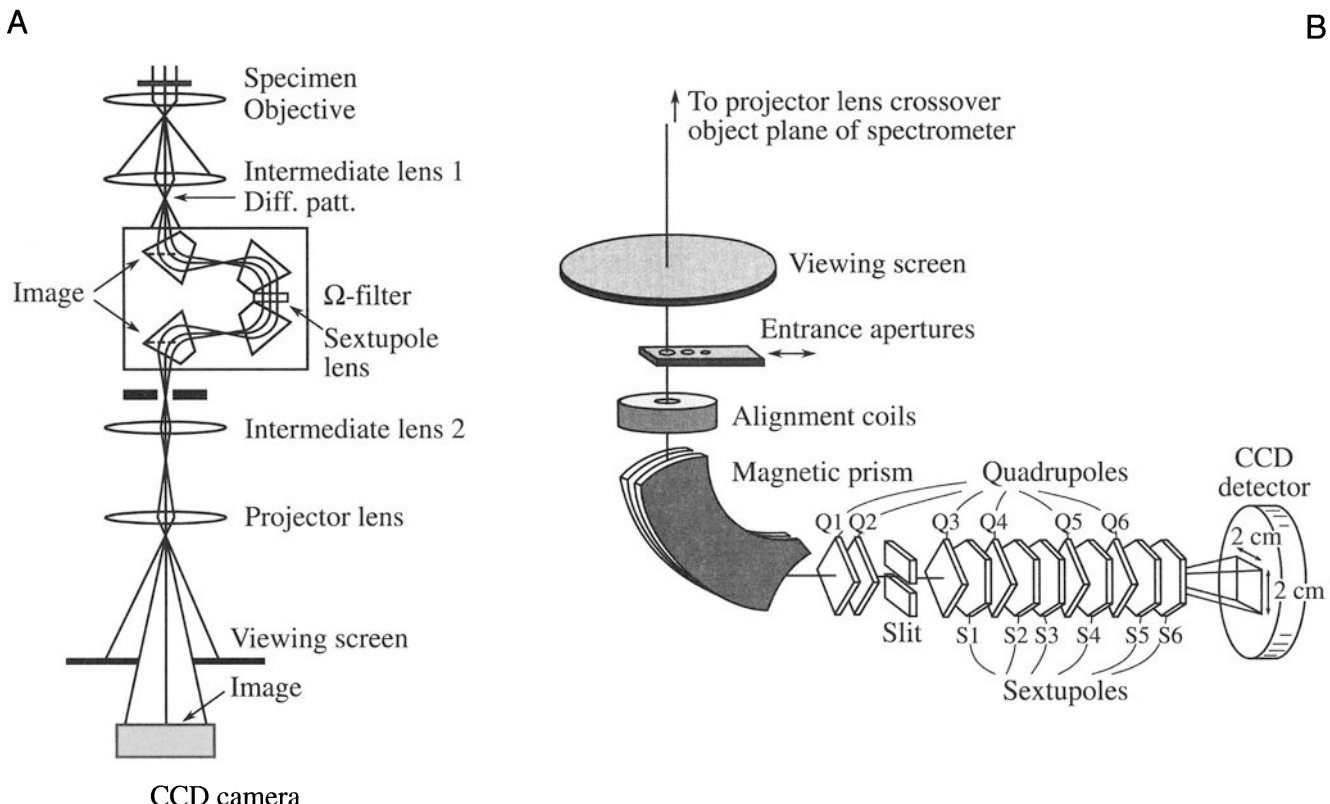


Figure 37.11. (A) Ray paths through the Ω filter system inserted in the imaging lens system of the LEO TEM. (B) The Gatan Imaging Filter attached to the TEM column after the imaging lenses, in the same position as a PEELS.

CHAPTER SUMMARY

We generally use a magnetic prism spectrometer for EELS. It is a simple device and very sensitive, but requires careful operation and an understanding of how it functions in combination with different TEM modes. PEELS is the preferred type of spectrometer, and it is best operated with the TEM in diffraction or STEM mode, or with a DSTEM. You have to know how to focus and calibrate it and how to determine the collection semi-angle, β . Once you can do this you're in a position to analyze energy-loss spectra, so in the next chapter we'll tell you what these spectra look like and what information they contain. If you have an Ω filter, or GIF, you can routinely form images or DPs with electrons of specific E .

REFERENCES

General References

- Disko, M.M., Ahn, C.C., and Fultz, B., Eds. (1992) *Transmission Electron Energy Loss Spectrometry in Materials Science*, TMS, Warrendale, Pennsylvania.
- Egerton, R.F. (1996) *Electron Energy-Loss Spectroscopy in the Electron Microscope*, 2nd edition, Plenum Press, New York.
- Krivanek, O.L., Ed. (1991) *Microsc. Microanal. Microstruct.* **2** (2,3).
- Krivanek, O.L., Ed. (1995a) *Microsc. Microanal. Microstruct.* **6** (1).
- Krivanek, O.L., Ed. (1995b) *Ultramicroscopy* **59** (1–4).

Specific References

- Castaing, R. and Henry, L. (1962) *C. R. Acad. Sci. Paris* **B255**, 76.
- Egerton, R.F., Yang, Y.Y., and Cheng, S.Y. (1993) *Ultramicroscopy* **48**, 239.
- Hillier, J. and Baker, R.F. (1944) *J. Appl. Phys.* **15**, 663.
- Krivanek, O.L., Gubbens, A.J., Dellby, N., and Meyer, C.E. (1992) *Microsc. Microanal. Microstruct.* **3**, 187.
- Lanio, S., Rose, H., and Krah, D. (1986) *Optic* **73**, 56.
- Metherell, A.J.F. (1971) in *Advances in Optical and Electron Microscopy*, 4 (Eds. R. Barer and V.E. Cosslett), p. 263, Academic Press, New York.
- Zanchi, G., Kihn, Y., and Sevely, J. (1982) *Optik* **60**, 427.

The Energy-Loss Spectrum

38

38.1. A Few Basic Concepts	655
38.2. The Zero-Loss Peak	656
38.3. The Low-Loss Spectrum	656
38.3.A. Plasmons	656
38.3.B. Inter- and Intra-Band Transitions	658
38.4. The High-Loss Spectrum	658
38.4.A. Inner-Shell Ionization	658
38.4.B. Ionization-Edge Characteristics	662
38.5. Artifacts in the Spectrum	664

CHAPTER PREVIEW

The term “energy-loss” spectrometry implies that we are only interested in inelastic interactions, but the spectrum will also contain electrons which have not lost any energy so we need to consider elastic scattering as well. We’ll deal with three principal regions of the energy-loss spectrum:

- The zero-loss peak, which consists primarily of elastic forward-scattered electrons, but also contains electrons that have suffered minor (unresolvable) energy losses.
- The low-loss region up to an energy loss of ~50 eV contains electrons which have interacted with the weakly bound outer-shell electrons of the atoms in the specimen.
- Electrons in the high-loss region have interacted with the more tightly bound inner-shell or “core” electrons.

These different regimes of energy losses can give us different information about the specimen. The terminology is a bit vague but is generally accepted. The zero-loss peak defines the energy resolution and is essential in calibrating your spectrum. The electrons in the low-loss region have only interacted weakly with the atoms via their outer-shell electrons, so they contain information about the electronic properties of the specimen. The electrons in the high-loss region have “probed” the inner electron shells and therefore contain information characteristic of the atoms in the specimen.

We can also obtain information about how the atoms are bonded to one another, and even how the neighboring atoms are distributed around a specific atom. In principle, the energy-loss spectrum is far more useful than an XEDS spectrum. However, it is also far more complex. To understand its content you need a greater understanding of the physics of beam–specimen interactions. The spectrum also contains artifacts which we need to identify and minimize.

In this chapter we will discuss the different features of electron energy-loss spectra and go on to use these spectra in Chapters 39 and 40.

The Energy-Loss Spectrum

38

38.1. A FEW BASIC CONCEPTS

Back in Chapters 2–4 we talked about the difference between elastic and inelastic beam–specimen interactions and introduced the ideas of scattering cross sections and the associated mean-free path. It would be a good idea to remind yourself of those ideas before starting on this chapter. Briefly, you should recall that elastic scattering is an electron–nucleus interaction; the word “elastic” implies that there is no energy loss although a change in direction, and hence in momentum, usually occurs. Elastic scattering is usually manifest as Bragg diffraction in crystalline specimens. Inelastic scattering is primarily an electron–electron interaction and entails both a loss of energy and a change of momentum. Therefore, we have to be concerned with both the amount of energy lost and the direction of the electrons after they’ve come through the specimen. This latter point is one reason why the collection semiangle of the spectrometer is so important.

Remember, the cross section is a measure of the probability of a specific scattering event occurring and the mean free path is the average distance between particular interactions. Also, you must remember to distinguish between the definitions of scattering that will keep appearing.

Single scattering occurs when each electron undergoes at most one scattering event as it traverses the specimen.

Plural scattering (>1 scattering event) and multiple scattering (>20 scattering events) imply that the electron has undergone a combination of interactions.

We’ll see that the energy-loss spectrum is most understandable when it represents single scattering. This ideal is approached when we have very thin specimens. In prac-

tice, most specimens are thicker than ideal and so we usually acquire plural-scattering spectra, and we may have to remove the plural-scattering effects. If multiple scattering occurs, the specimen is too thick for EELS and for much of TEM in general.

The principal inelastic interactions in order of increasing importance (and energy loss) are phonon excitations, inter- and intra-band transitions, plasmon excitations, and inner-shell ionizations. We’ve already introduced these processes back in Chapter 4 and we will emphasize inner-shell ionizations almost exclusively from here on. The two major characteristics of any inelastic scattering are the energy loss \mathcal{E} and the scattering semiangle θ , and we summarize typical values in Table 38.1.

It’s a little difficult to be specific about the values of the scattering angle because the angle varies with energy. In fact there are different definitions of scattering angle which you may come across, and these can be confusing. You can find derivations of the equations governing scattering in Egerton (1996).

The symbol θ in all cases refers to the scattering semiangle.

We will always assume that the scattering is symmetrical around the direct beam. The most important angle is θ_E , the so-called characteristic or most-probable scattering semi-angle for an energy loss, \mathcal{E} . This angle is given by

$$\theta_E \approx \frac{\mathcal{E}}{2E_0} \quad [38.1]$$

This equation is an approximation and it ignores relativistic effects, so you should only use it for rough calculations at and above 100 keV. We can be more precise and define θ_E as

Table 38.1. Characteristics of the Principal Energy-Loss Processes

Process	Energy loss (eV)	θ_E (mrads)
Phonons	~0.02	5–15
Inter/intra-band transitions	5–25	5–10
Plasmons	~5–25	<~0.1
Inner-shell ionization	~10–1000	1–5

$$\theta_E \approx \frac{E}{(\gamma m_0 v^2)} \quad [38.2]$$

Here we have the usual definitions: m_0 is the rest mass of the electron, v is the electron velocity, and γ is given by

$$\gamma = \left(1 - \frac{v^2}{c^2}\right)^{-\frac{1}{2}} \quad [38.3]$$

The electron velocity is v and c is the velocity of light. One other useful angle, θ_C , is the cut-off angle above which the scattered intensity is zero, and this is given by

$$\theta_C = (2\theta_E)^{\frac{1}{2}} \quad [38.4]$$

In Table 38.1 we have given some typical values of θ_E . This is the scattering angle that we'll usually refer to from now on. Let's now move on to the energy-loss spectrum. We'll start at the low-energy end and proceed to higher-energy losses.

38.2. THE ZERO-LOSS PEAK

If your specimen is thin, the predominant feature in the energy-loss spectrum will be the zero-loss peak. As the name implies, this peak consists mainly of electrons that have completely retained the beam energy E_0 . Such electrons may be forward scattered in a relatively narrow cone within a few mrads of the optic axis and constitute the 000 spot in the DP, i.e., the direct beam. If we were to tilt the incident beam so a diffracted beam entered the spectrometer, then it too would give a zero-loss peak. The scattering angles for diffraction ($2\theta_B$) are relatively large (~20 mrad) compared to the smaller collection angles in EELS, and so the diffracted beams rarely enter the spectrometer. Actually, we can also measure the intensity and energy of electrons as a function of their angular distribution, and we'll discuss this aspect briefly in Chapter 40.

Now the term "zero-loss peak" is really a misnomer for two reasons. First, our spectrometers have a finite energy resolution (at best ~0.3 eV) so the zero-loss peak will also contain electrons that have lost very small amounts of energy, mainly those that excited phonons. So in EELS in

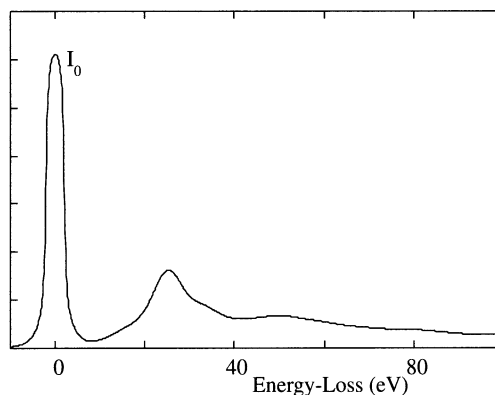


Figure 38.1. The intense zero-loss peak I_0 in a spectrum from stainless steel. The rest of the spectrum comprises energy-loss electrons which constitute a relatively small fraction of the total intensity in the spectrum.

the TEM we never resolve phonon losses. This is not a "great loss" since phonon-loss electrons don't carry any useful information anyway; they only cause the specimen to heat up. However, it does explain why we shouldn't really call this the zero-loss peak. Second, we can't produce a beam of monochromatic electrons; the beam has a finite energy range about the nominal value E_0 . Despite this imprecision, we will continue to use the zero-loss terminology.

The zero-loss peak is usually a problem rather than a useful feature in the spectrum, because it is so intense that it can damage the scintillator or saturate the photodiode array. We don't collect it except under certain circumstances. Figure 38.1 shows the intense zero-loss peak in a spectrum. To the right of the peak is a relatively small peak, which is part of the low-loss spectrum. This small peak is where we start to get useful information, but you can also see immediately that the useful part of the spectrum is very much less intense than the somewhat useless zero-loss peak, and this is one of several fundamental problems in EELS.

38.3. THE LOW-LOSS SPECTRUM

We use the term "low-loss" to describe energy-loss electrons in the range up to about 50 eV. In this part of the spectrum we come across electrons that have set up plasmon oscillations or have generated inter- or intra-band transitions. Plasmons are by far the most important, so we'll look at these first.

38.3.A. Plasmons

Plasmons are longitudinal wave-like oscillations of weakly bound electrons. The oscillations are rapidly damped, typi-

Table 38.2. Plasmon Loss Data for 100-keV Electrons for Several Elements

Material	E_p (calc) (eV)	E_p (expt) (eV)	θ_E (mrad)	θ_C (mrad)	λ_p (calc) (nm)
Li	8.0	7.1	0.039	5.3	233
Be	18.4	18.7	0.102	7.1	102
Al	15.8	15.0	0.082	7.7	119
Si	16.6	16.5	0.090	6.5	115
K	4.3	3.7	0.020	4.7	402

cally having a lifetime of about 10^{-15} s and so are quite localized to <10 nm. The plasmon peak is the second most dominant feature of the energy-loss spectrum after the zero-loss peak. The small peak beside the zero-loss peak in Figure 38.1 is a plasmon peak.

The energy E_p lost by the beam electron when it generates a plasmon of frequency ω_p is given by

$$E_p = \frac{h}{2\pi} \omega_p = \frac{h}{2\pi} \left(\frac{ne^2}{\epsilon_0 m} \right)^{\frac{1}{2}} \quad [38.5]$$

where h is Planck's constant, e and m are the electron charge and mass, ϵ_0 is the permittivity of free space, and n is the free-electron density. Typical values of E_p are in the range 5–25 eV and a summary is given in Table 38.2.

Plasmon losses dominate in materials with free-electron structures, such as Li, Na, Mg, and Al, but occur to a greater or lesser extent in all materials.

We even see a plasmon-like peak in spectra from materials with no free electrons (such as polymers) for reasons that are not well understood. From equation 38.5 you can see that E_p is affected by n , the free-electron density. Interestingly, n may change with the chemistry of the specimen. So in principle, measurement of the plasmon energy loss can give indirect microanalytical information, as we'll see later in Section 40.2. Plasmon-loss electrons also carry contrast information and therefore are important because they limit image resolution through chromatic aberration. We can remove them from the image by energy filtering, as we'll also describe in Section 40.3.

Because of the low values of λ_p , the characteristic scattering angles θ_E are very small, being typically <0.1 mrad (as listed in Table 38.2). So, plasmon-loss electrons are strongly forward-scattered. Their cut-off angle $\theta_C \sim 100 \theta_E$. Hence if you use a β of only 10 mrad, you will gather virtually all the plasmon-loss electrons. Also, their line width ΔE_p is at most a few eV.

A typical value of the plasmon mean-free path λ_p at AEM voltages is about 100 nm, and so it is reasonable to expect at least one strong plasmon peak in all but the thinnest specimens. Likewise, the number of individual losses should increase with the thickness of the specimen. Figure 38.2 shows the plasmon-loss spectra from thin and thick foils of pure Al. Since Al is a good approximation to a free-electron metal, the plasmon-loss process is the dominant energy-loss event. Plural plasmon scattering in thicker foils is a most important phenomenon because it eventually limits the interpretation of part of the spectrum containing chemical information from ionization losses in which we are really interested (see Section 38.4). The well-known properties of plasmon

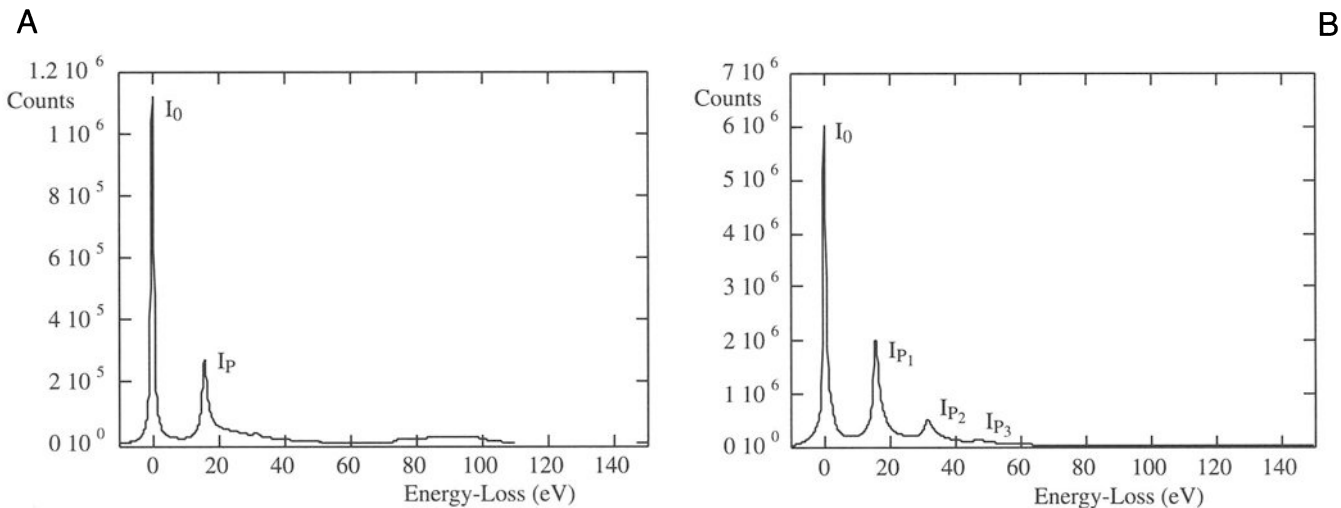


Figure 38.2. (A) The low-loss spectrum from a very thin sample of pure Al showing the intense zero-loss peak (I_0) and a small plasmon peak (I_p) at about 15 eV. (B) The low-loss spectrum from a thicker specimen of pure Al showing several plasmon peaks.

loss electrons from several elements are summarized in Table 38.2.

The plasmon losses which we've just described all arise from interactions with the electrons in the interior of the specimen, but the incident electrons can also set up plasmon oscillations on the surface of the specimen. We can envisage these surface plasmons as transverse charge waves. Surface plasmons have about half the energy of bulk plasmons. Generally, however, the surface plasmon peak is much less intense than the volume plasmon peaks, even in the thinnest specimens.

38.3.B. Inter- and Intra-Band Transitions

An electron in the beam may transfer sufficient energy to a core electron to cause it to change its orbital state, for example, to a Bohr orbit of higher quantum number. We call these events “single electron interactions” and they result in energy losses of up to ~ 25 eV. Interactions with molecular orbitals such as the π orbitals produce characteristic peaks in this low-energy region of the spectrum, and it is possible sometimes to use the intensity variation in this part of the spectrum to identify a particular specimen. However, the details of the spectrum intensity variations due to single electron interactions are not well understood and cannot yet be predicted *a priori*.

Use of the low-loss spectrum for phase identification is only possible through a “fingerprinting” process by which the low-loss spectra of known specimens are stored in a library in the computer.

Spectra from unknown specimens may then be compared with the stored library standards. Figure 38.3 shows the low-loss spectra of Al and Al-containing compounds exhibiting differences in the detailed intensity variation. A collection of low-loss spectra from all the elements has been compiled in the EELS Atlas (Ahn and Krivanek 1983) and this can help with “fingerprinting” unknown specimens.

If the beam electron gives a weakly bound valence-band electron sufficient energy to escape the attractive field of the nucleus, then we've created a secondary electron (SE), of the sort used to give topographic images in the SEM and STEM. Typically, we give < 20 eV to a SE and therefore the electrons causing SE emission appear in the same low-energy region of the spectrum as the inter- and intra-band transitions.

The weakly bound outer-shell electrons control the reaction of an atom to an external field and thus control the dielectric response of the material. We'll see in Chapter 40 that it is possible to get a measure of the dielectric constant by careful processing of the very low loss portion ($<\sim 10$ eV) of the spectrum.

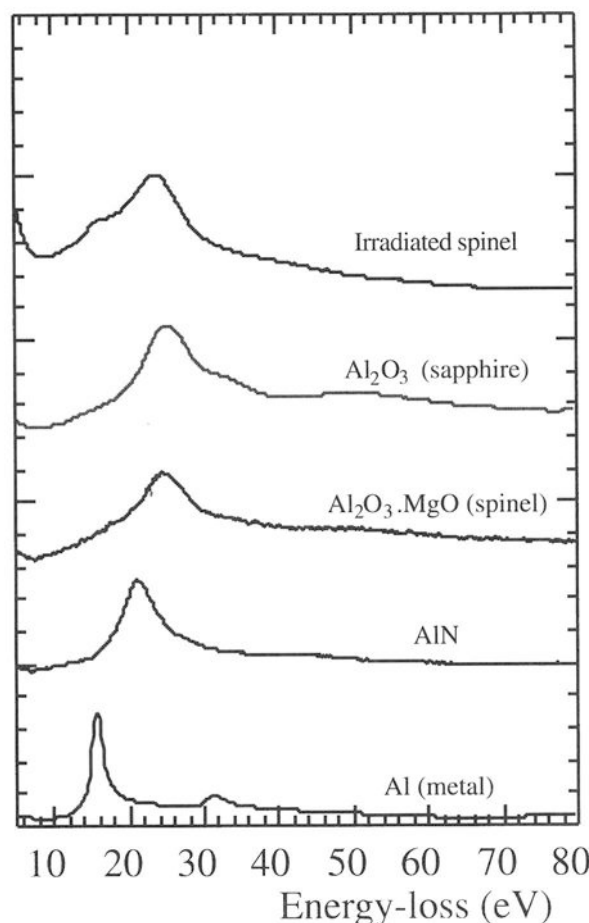


Figure 38.3. The low-loss spectrum from specimens of Al and Al-containing compounds, showing differences in intensity that arise from differences between the bonding in the different materials. The spectra are displaced vertically for ease of comparison.

38.4. THE HIGH-LOSS SPECTRUM

The high-loss portion of the spectrum above about 50 eV contains information from inelastic interactions with the inner or core shells.

38.4.A. Inner-Shell Ionization

When a beam electron transfers sufficient energy to a K, L, M, N, or O shell electron to move it outside the attractive field of the nucleus, as shown back in Figure 4.2, the atom is said to be ionized. As you know from the earlier chapters on X-ray analysis, the decay of the ionized atom back to its ground state may produce a characteristic X-ray, or an Auger electron. So the processes of inner-shell ionization-

loss EELS and XEDS are different aspects of the same phenomenon. We are interested in ionization losses precisely because the process is characteristic of the atom involved and so the signal is a direct source of elemental information, just like the characteristic X-ray. We call the ionization-loss signal an “edge” for reasons we’ll describe shortly.

You should appreciate that detection of the beam electron that ionized the atom is independent of whether the atom emits an X-ray or an Auger electron. EELS is not affected by the fluorescence-yield limitation that restricts light-element X-ray analysis. This difference explains, in part, the complementary nature of XEDS and EELS.

Inner-shell ionization is generally a high-energy process. For example, the lightest solid element, Li, requires an input of ≥ 55 eV to eject a K-shell electron, and so the loss electrons are usually found in the “high-loss” region of the spectrum, above ~ 50 eV. K-shell electrons require much more energy for ejection as Z increases, because they are more strongly bound to the nucleus. The binding energy for electrons in the Uranium K shell is about 99 keV. So, as in XEDS, we tend to look for other lower-energy ionizations, such as the L and M edges, when dealing with high- Z atoms. Typically, we start to use the L edges when the K-shell energy exceeds ~ 1 keV (Na) and M edges when the L shell exceeds ~ 1 keV (Zn).

It’s worth a short mention here about the nomenclature used for EELS edges. Just like in X-rays, where we have K, L, M, etc. peaks in the spectrum, we get ionization edges from K, L, M, etc. shell electrons. However, the greater energy resolution of the EELS spectrometer means that it is much easier to detect differences in spectra that arise from the presence of different energy states in the shell. For example:

- The K-shell electron is in the 1s state and gives rise to a single K edge.
- In the L shell, the electrons are in either 2s or 2p orbitals, and if a 2s electron is ejected, then we get an L_1 edge, and a 2p electron causes either an L_2 or L_3 edge.

The L_2 and L_3 edges may not be resolvable at lower ionization energies (e.g., they aren’t in Al but they are in Ti), and sometimes we call this edge the $L_{2,3}$. The full range of possible edges is shown schematically in Figure 38.4, and you can see that other “dual” edges exist, such as the $M_{4,5}$. There will be more about this in Chapter 40.

Compared with plasmon excitation, which requires much less energy, the ionization cross sections are relatively small and the mean-free paths relatively large. As a result the ionization edge intensity in the spectrum is very much smaller than the plasmon peak, and becomes even smaller as the energy loss increases (look back to Figure 37.4A). This is another reason for staying with the lower-energy-loss (L and M) core edges. While the possibility of plural ionization events being triggered by the same electron is small in a typical thin foil, we’ll see that the combination of an ionization loss with a plasmon loss is by no means uncommon, and this phenomenon distorts the resultant spectrum.

If you go back and look at Figure 4.2, you can see that a specific minimum-energy transfer from the beam electron to the inner-shell electron is required to overcome the binding energy of the electron to the nucleus and ionize the atom.

This minimum energy constitutes the ionization threshold, or the critical ionization energy, E_C .

We define E_C as E_K for a particular K-shell electron, E_L for an L shell, etc. Of course, it is also possible to ionize an atom by the transfer of $E > E_C$. However, the chances of ionization occurring become less with increasing energy above E_C , because the value of the cross section decreases with increasing energy. As a result, the ionization-loss electrons have an energy distribution that ideally shows a sharp rise to a maximum at E_C , followed by a slowly decreasing intensity above E_C back toward the background. This triangular shape is called an “edge.”

This idealized triangular or saw-tooth shape is only found in spectra from isolated hydrogen atoms, and is therefore called a hydrogenic ionization edge. Real ionization edges have shapes that approximate, more or less, to the hydrogenic edge.

You’ll notice that this edge, shown in Figure 38.5A, has almost the same intensity profile as the “absorption edges” in X-ray spectroscopy. In reality, because we aren’t dealing with isolated atoms but atoms integrated into a crystal lattice or amorphous structure, the spectra become more complex. The ionization edges are superimposed on a rapidly decreasing background intensity from electrons that have undergone random, plural inelastic scattering events (Figure 38.5B). The edge shape may also contain fine structure around E_C (Figure 38.5C) which is due to bonding effects, and is termed energy-loss near-edge structure (ELNES). More than ~ 50 eV after the edge, small intensity oscillations may be detectable (Figure 38.5D) due to diffraction effects from the atoms surrounding the ion-

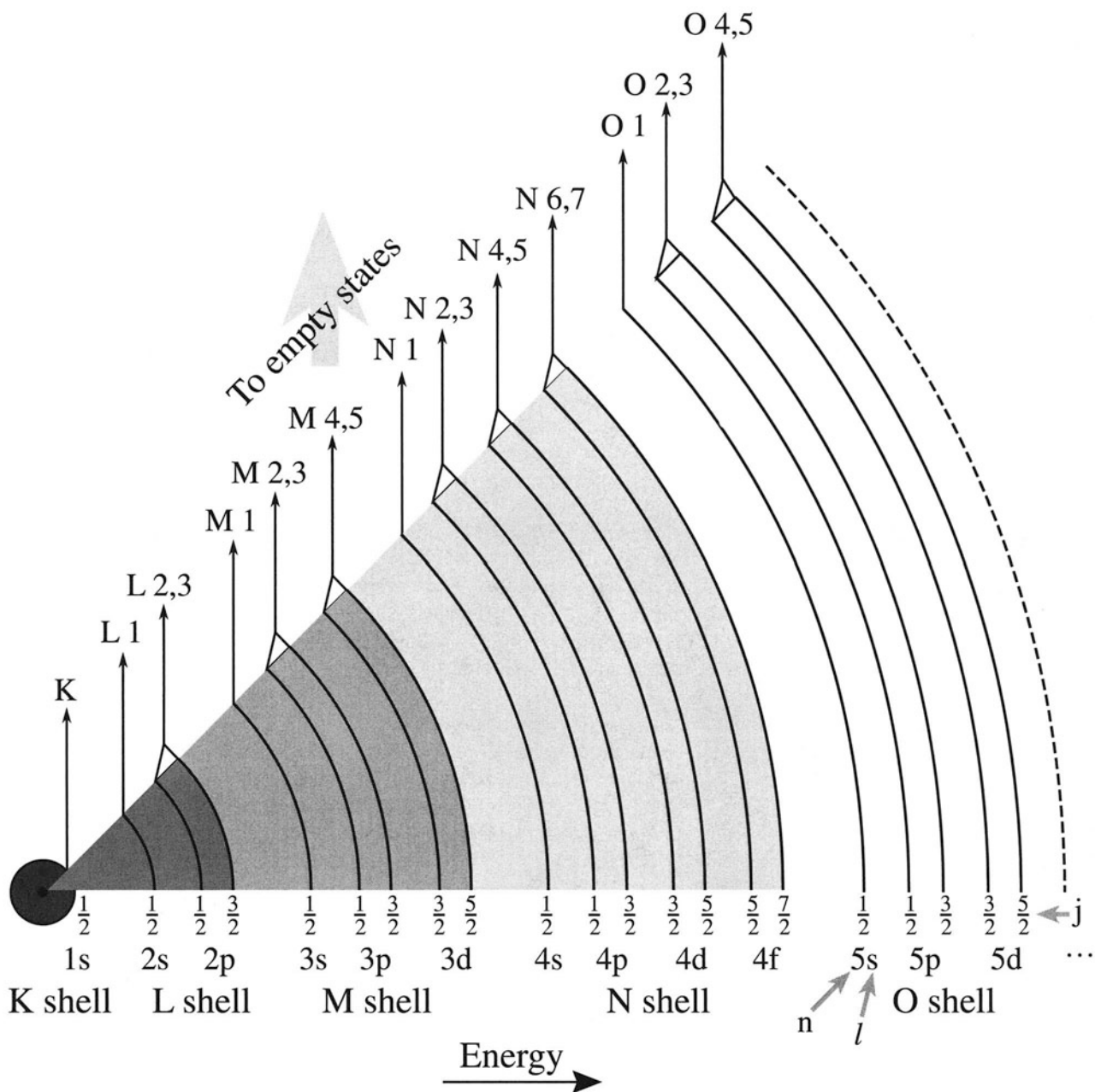


Figure 38.4. The full range of possible edges due to inner-shell ionization, and their associated nomenclature.

ized atom, and these oscillations are called extended energy-loss fine structure (EXELFS), which is analogous to extended X-ray absorption fine structure (EXAFS) in X-ray spectra, particularly those generated from intense synchrotron sources.

- Fine structure before or around the peak is known as ELNES.
- Small intensity oscillations ~ 50 eV after the edge due to diffraction effects are called EXELFS.

Finally, as we noted earlier, the ionization-loss electrons may also undergo further low-loss interactions. They may create plasmons, in which case the ionization edge contains plural scattering intensity $\sim 15\text{--}25$ eV above E_C , as shown in Figure 38.5E. So the resultant ionization edge is far more complicated than the simple Gaussian peak seen in an XEDS spectrum. Clearly, the edge details contain far more information about the specimen than a characteristic X-ray peak. From an X-ray spectrum you only get *elemental* identification rather than *chemical* in-

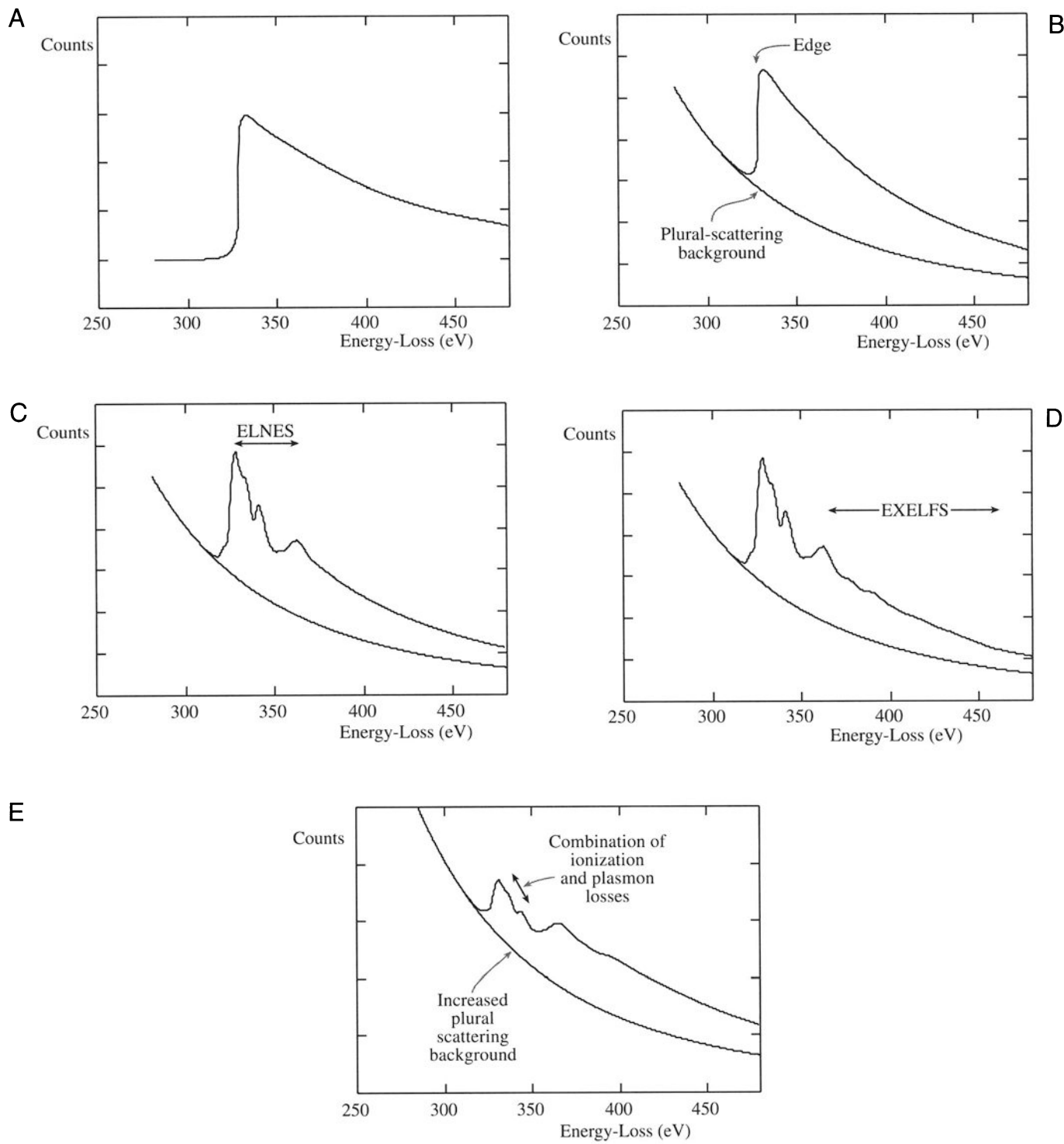


Figure 38.5. The characteristic features of an inner-shell ionization edge: (A) the idealized saw-tooth (hydrogenic) edge, (B) the edge superimposed on the background arising from plural inelastic scattering, (C) the presence of ELNES, (D) the EXELFS. (E) Plural scattering in a thick specimen, such as the combination of ionization and plasmon losses, distorts the post-edge structure and give an increase in the background level.

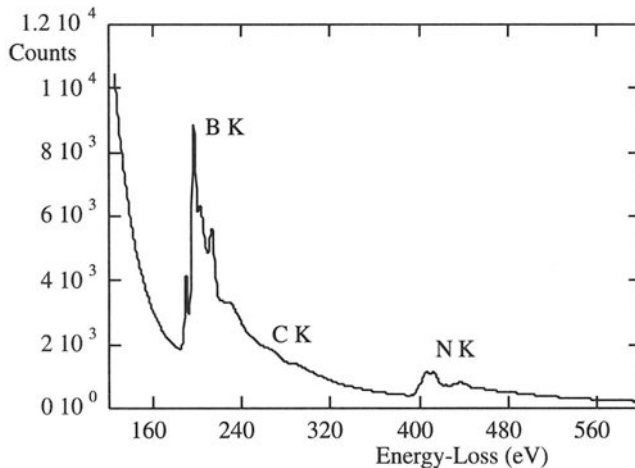


Figure 38.6. High-energy-loss spectrum from a particle of BN over a hole in a C film showing the B and N K-shell ionization edges superimposed on a rapidly decreasing background. A faint C K edge is also visible at ~ 280 eV.

formation, such as bonding, which is contained in the ELNES. Figure 38.6 shows a spectrum from BN on a C film. The various ionization edges show some of the features drawn schematically in Figure 38.5; we'll discuss these “fine structure” effects more in Section 40.1.

38.4.B. Ionization-Edge Characteristics

The angular distribution of ionization-loss electrons varies as $(\theta^2 + \theta_E^{-2})^{-1}$ and will be a maximum when $\theta = 0^\circ$, in the forward-scattered direction. The distribution decreases to a half width at the characteristic scattering angle θ_E given by equation 38.1. This behavior is essentially the same as for plasmon scattering, but we have relatively large values of E_C compared to E_p :

- $\theta_E \sim 5$ mrad for ionization-loss electrons at $E_C = 1000$ eV, for a beam energy of 100 keV.
- The average plasmon-loss scattering was broadened to ~ 10 –15 mrad.

The characteristic scattering angles for both plasmon and inner-shell ionization are still much lower than the characteristic scattering angles for phonon and elastic scattering. The angular distribution varies depending on the energy loss, and because of the extended energy range of ionization-loss electrons above E_C , this can be quite complicated. For $E \sim E_C$ the intensity drops rapidly to zero over about 10 mrad at θ_E , but as E increases above E_C the angular intensity distribution drops around $\theta = 0^\circ$, but increases at larger scattering angles, giving rise to the so-called Bethe Ridge. Since this effect is irrelevant for EELS studies, we'll ig-

nore it, but you can find more information in Egerton (1996).

So, in the region immediately following the ionization edge the angular distribution of the electrons is generally confined to a semiangle of <10 –15 mrad and drops to zero beyond this. In other words, like the plasmon-loss electrons, the ionization-loss electrons are very strongly forward-scattered. Consequently, efficient collection of the major inelastically scattered electrons is a straightforward matter, since a spectrometer entrance aperture semiangle (β) of <20 mrad will collect the great majority of these electrons. As a result, collection efficiencies in the range 50–100% are not unreasonable, which contrasts with the situation in XEDS, where the isotropic generation of characteristic X-rays results in very inefficient collection. Figure 38.7 compares the collection of X-rays and energy-loss electrons in the AEM. Figure 38.8 shows the variation in collection efficiency for ionization-loss electrons as a function of both β and energy.

While the K edges in Figure 38.6 show reasonably sharp onsets, like an ideal hydrogenic edge, not all edges are similar in shape. Some edges have much broader onsets, spread over several eV or even tens of eV. The edge shape in general depends on the electronic structure of the atom but, unfortunately, we can't give a simple relationship between specific edge types and specific shapes. The situation is further complicated by the fact that the edge shapes change significantly depending on whether or not

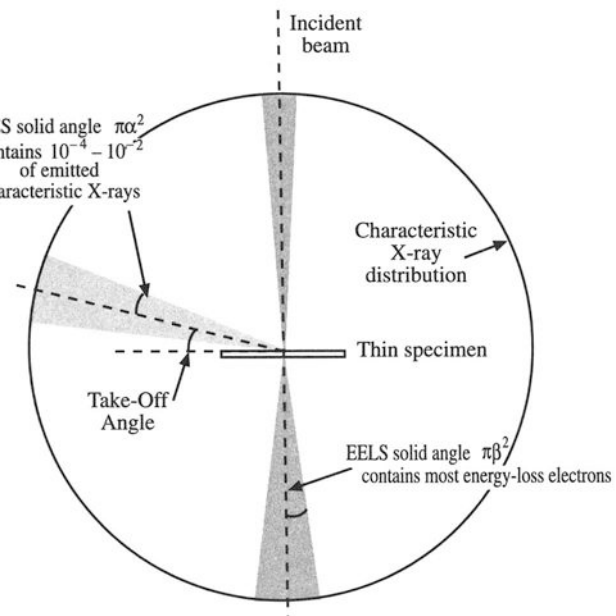


Figure 38.7. Comparison of the relative efficiencies of collection of EELS and XEDS. The forward-scattered energy-loss electrons are more efficiently collected than the uniformly emitted characteristic X-rays.

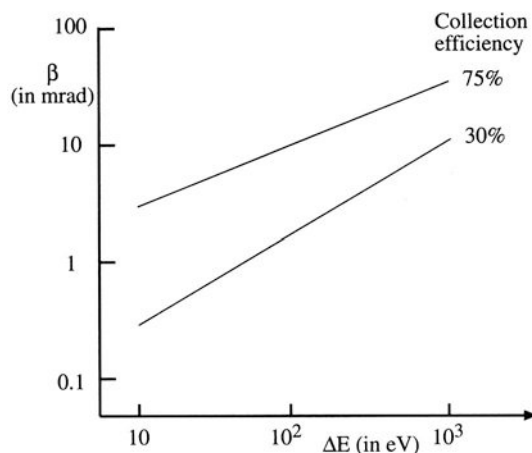


Figure 38.8. Variation in the collection efficiency of ionization-loss electrons as a function of their energy and the spectrometer collection semiangle, β .

certain energy states are filled or unfilled. For example, if you look below at Figure 38.9, the Ni L edge shows two sharp peaks, which are the L_3 and L_2 edges. (We'll discuss these details much more in Section 40.1.) These sharp lines arise because the ejected L shell electrons don't entirely escape from the atom and have a very high probability of ending up in unfilled d band states, which are present in Ni. In contrast, in Cu, in which the d band is full, the $L_{2,3}$ edge does not show these intense lines. Similar sharp lines appear in the $M_{4,5}$ edges in the rare earths. As if this were not enough, the details of the fine structure and edge shapes are also affected by bonding. For example, the Ni edge in NiO in Figure 38.9 is different from the Ni edge in pure Ni. To sort all this out it's best if you consult the EELS Atlas (Ahn and Krivanek 1983), which contains representative edges from all the elements and many oxides.

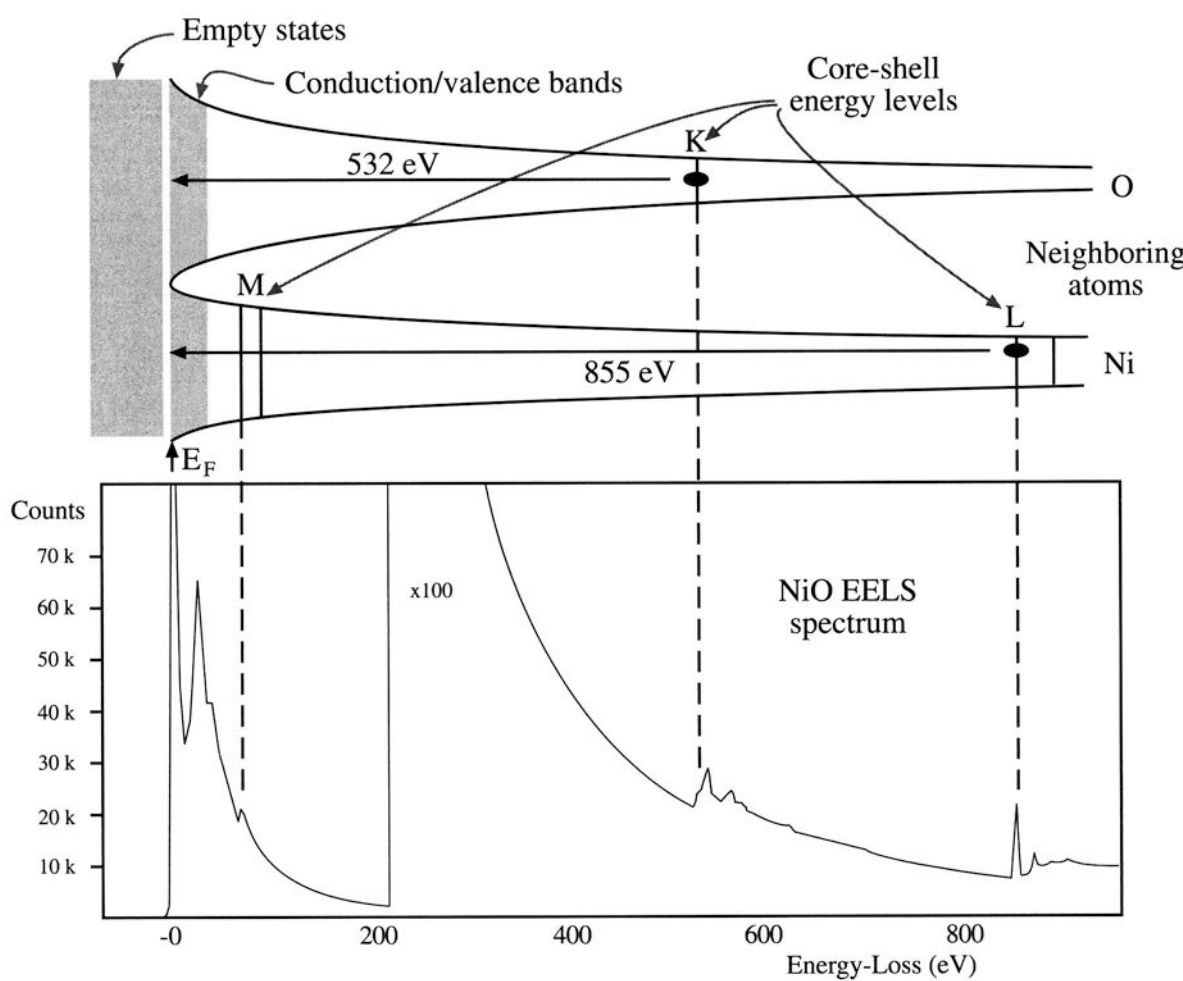


Figure 38.9. The correspondence between the energy levels of electrons surrounding adjacent Ni and O atoms and the energy-loss spectrum: the zero-loss peak is above the Fermi energy E_F , the plasmon peak is at the energy level of the conduction/valence bands, and the critical ionization energy required to eject specific K-, L-, and M-shell electrons is shown.

We can summarize the characteristics of the energy-loss spectrum by showing a complete spectrum from NiO containing both low- and high-loss electrons, as shown in Figure 38.9. In this figure we also compare the spectrum to the energy-level diagram for NiO. You can see that:

- The plasmon peak corresponds to the energy of the valence electron band just below the Fermi level (E_F).
- The relative energy levels of the ionized atom (K, L, or M) control the position of the ionization edge in the spectrum.
- The different density of states in the valence (3d) band of the Ni atom is indicated by shading at the top of the potential wells and is reflected in the characteristic, intense, near-edge, fine structure at the Ni L edge.

The electrons could also be given sufficient energy to travel into the conduction band well above E_F ; as we just mentioned, in this case we see extended fine structure after the ionization edge. We'll discuss more details of such fine structure in the spectrum in Chapter 40.

Despite the very high collection efficiency of the spectrometer, the ionization edges, which are the major signal for elemental analysis, show relatively low intensity, have an extended energy range above the ionization energy, and ride on a rapidly varying, relatively high background. All these factors, as we shall see, combine to make quantitative microanalysis using EELS a difficult and less accurate technique when compared with XEDS. However, for the light elements the X-ray fluorescence yield drops to such low values, and absorption becomes so strong, even in thin specimens, that EELS is the preferred technique. Experimentally, the choice between the two is not simple, but below oxygen in the periodic table, EELS has shown better performance than XEDS and, for elements below boron, there is no sensible alternative to EELS for microanalysis at high spatial resolution.

38.5. ARTIFACTS IN THE SPECTRUM

The SEELS spectrum contains no artifacts of any consequence, unless it is grossly misaligned, in which case the beam may scatter through the slits or off the drift tube, giving distorted background intensities. These effects are easy to spot and correct.

Unfortunately, the highly efficient PEELS system generates more artifacts which you have to recognize and remove before analyzing the spectrum. Details are available in the Gatan manual, but here we'll summarize

the major problems (which are in addition to the point-spread function that we talked about in the previous chapter).

All the individual diodes will differ slightly in their response to the incident electron beam, and therefore there will be a channel-to-channel gain variation in intensity. This will be characteristic of each individual diode array.

One way to determine the gain variation is to spread the beam uniformly over the array using at least the 3-mm entrance aperture and looking at the diode readouts, as shown in Figure 38.10. This is difficult with an FEG system because the probe is too small, and then it is necessary to scan the beam across the array, although this is not very satisfactory. Then you have to divide your experimental spectrum by this response spectrum to remove the gain variation. Alternatively, and this is recommended, you can gather two or more spectra with slight energy shifts (~1–2 eV) or spatial shifts between them and superimpose them electronically. The gain variation then disappears, as you can see if you look at Figure 38.12. Using a two-dimensional array, as in the GIF, removes this problem also.

Gathering many spectra and superimposing them can bring another problem, namely, that of readout noise. There are two kinds of readout noise, random and fixed. The random readout noise, or shot noise, arises from the electronics chain from the diode to the display, and is minimized by taking as few readouts as possible, and also by

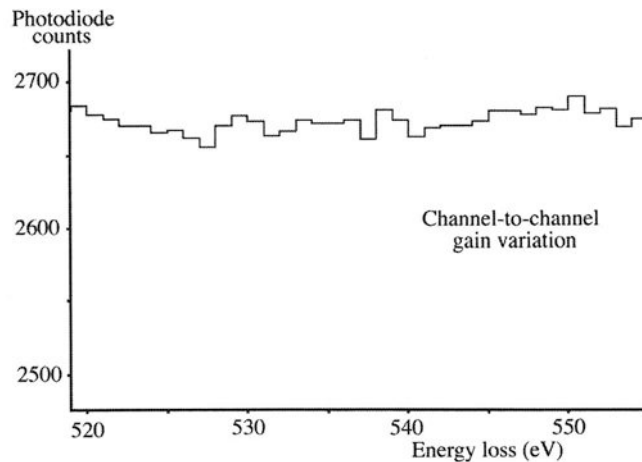


Figure 38.10. The variation in the response of individual diodes in the PEELS detection system to a constant incident electron intensity. A channel-to-channel gain variation is clear and each detector array has its own characteristic response function.

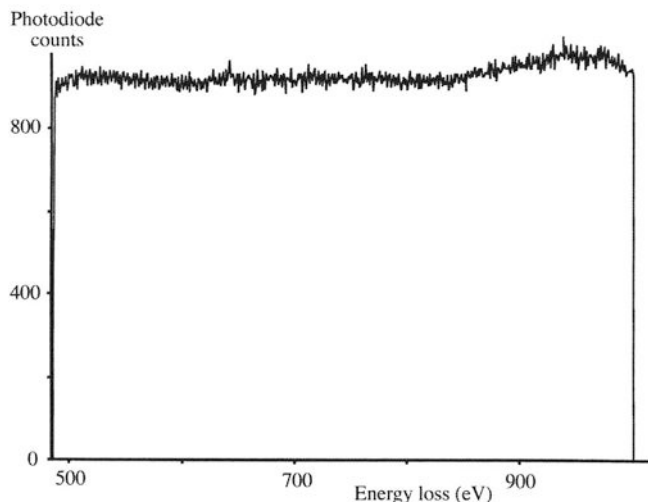


Figure 38.11. The intensity of the dark current which flows from the diode array when no electron beam is present.

cooling the diode array. Individual diodes may have high leakage currents which give a spike on the display. The fixed pattern readout noise is a function of the three-phase readout circuitry. All these effects will appear when there is no current falling on the diodes and together they constitute the dark current (see Figure 38.11). The dark current is small unless you have a bad diode array, and it is only a problem when there are very few counts in your spectrum or you have added together 10 or more spectra. Figure 38.12 shows some of these effects and how to remove them.

Finally, there is the problem of incomplete readout of the display. When the diodes are cooled, only ~95% of the signal is read out in the first integration, ~4.5% in the second, ~0.25% in the third, and so on. This is only a problem if you have saturated the diodes with an intense signal like the zero-loss peak. This peak then shows up as a ghost peak in the next readout and decays slowly over several readouts. So if a ghost peak appears, just run several readouts and it will disappear; this way you should never confuse a ghost peak with a genuine edge.

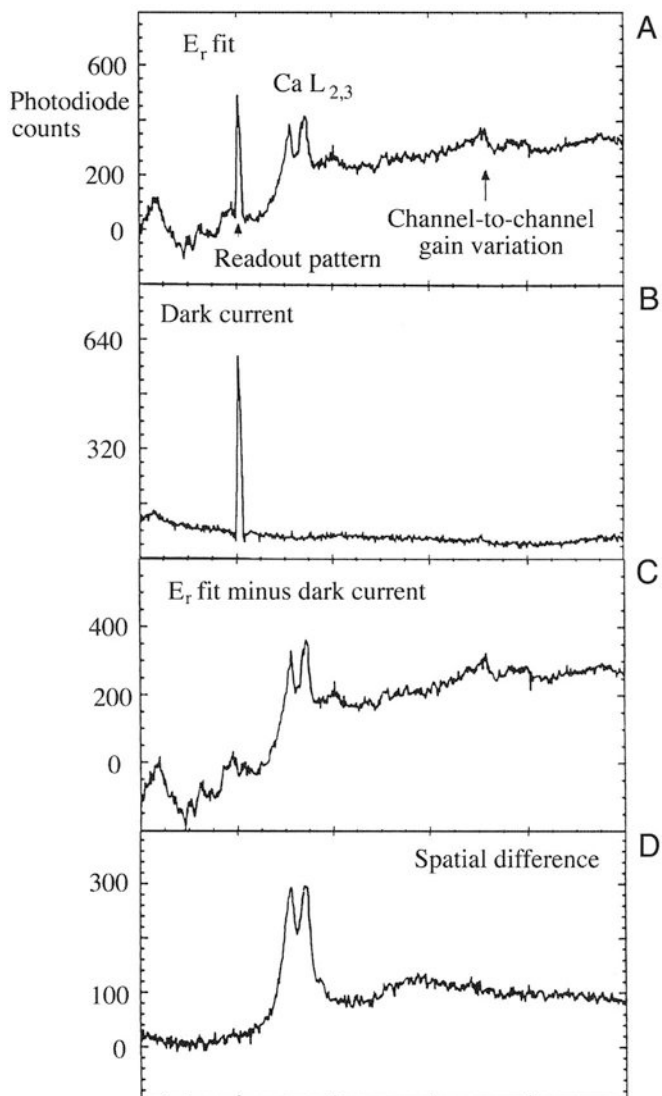


Figure 38.12. How to remove artifacts from a specimen: (A) A $\text{Ca L}_{2,3}$ edge spectrum showing both channel-to-channel gain variation and a faulty diode with a high leakage current which appears as a spike in the spectrum. The spike is referred to as the readout pattern and is present in every recorded spectrum. Subtracting the dark current (B) removes the spike (C) and a difference spectrum (D) removes the gain variation, leaving the desired edge spectrum.

CHAPTER SUMMARY

The EELS spectrum varies in intensity over several orders of magnitude.

- The least useful signal (the zero-loss peak) is the most intense, and the most useful signals (the ionization edges) are among the least intense signals.
- The low-loss spectrum reflects beam interactions with loosely bound conduction and valence-band electrons.

Table 38.3. PEELS Artifacts and How to Eliminate Them

Noise name	Source	Elimination
Leakage current	Different diodes	Subtract dark current
Internal scanning noise	Electronics readout	Adjust the electronics and subtract the dark count
Nonuniform sensitivity	Diode sensitivities differ	Determine the response characteristic by sweeping the beam along the array and divide the real spectrum by this result, i.e., normalize the diodes

- The high-loss spectrum contains small ionization edges riding on a strong plural-scattered background.
- Differences in the energy onset of the ionization edges distinguish different elements in the specimen.
- Differences in the fine structure of the edges reflect chemical (bonding) effects and structural (atomic arrangement) effects.
- Artifacts can complicate spectrum interpretation, but they are well understood and easily removed.

We summarize the different sources of noise and how we eliminate this noise in Table 38.3.

REFERENCES

Specific References

- Egerton, R.F. (1996) *Electron Energy Loss Spectroscopy in the Electron Microscope*, 2nd edition, Plenum Press, New York.
 Ahn, C.C. and Krivanek, O.L. (1983) *EELS Atlas*, Gatan Inc., 780 Commonwealth Drive, Warrendale, Pennsylvania.

Microanalysis with Ionization-Loss Electrons

39

39.1. Choice of Operating Parameters	669
39.2. What Should Your Spectrum Look Like?	670
39.3. Qualitative Microanalysis	671
39.4. Quantitative Microanalysis	672
39.4.A. Derivation of the Equations for Quantification	673
39.4.B. Background Subtraction	674
39.4.C. Edge Integration	676
39.4.D. The Zero-Loss Integral	676
39.4.E. The Partial Ionization Cross Section	676
39.5. Measuring Thickness from the Energy-Loss Spectrum	678
39.6. Deconvolution	680
39.7. Correction for Convergence of the Incident Beam	682
39.8. The Effect of the Specimen Orientation	682
39.9. Spatial Resolution	682
39.10. Detectability Limits	683

CHAPTER PREVIEW

In the previous two chapters we've described how to acquire an energy-loss spectrum and have also given you some idea of the information in such spectra. Most importantly, there are elemental composition data which can be extracted primarily from the high-loss ionization edges. In this chapter we'll examine how to get this information and quantify it. As we've already indicated, the prime use for these kind of data is light-element microanalysis, where EELS complements XEDS. First we'll remind you of the experimental variables over which you have control, because these are rather critical. Then we'll discuss how to obtain a spectrum and what it should look like for microanalysis. Next, we'll discuss the various quantification routines which, in principle, are just as straightforward as those for XEDS but in practice require a rather more sophisticated level of knowledge to carry them out successfully. Finally, we'll say a bit about spatial resolution and minimum detectability, although these topics aren't as important in EELS as they are in XEDS.

Microanalysis with Ionization-Loss Electrons

39

39.1. CHOICE OF OPERATING PARAMETERS

Perhaps a major reason why EELS is not as widespread as XEDS is the relative complexity of the experimental procedure and the number of variables which you have to define before you can get started. EELS is not yet a “turn-key” operation so you cannot simply place your specimen under the beam, switch on the spectrometer and the computer, and acquire a spectrum. This is in marked contrast to the situation in XEDS, where the high degree of software control means that the XEDS system is almost invariably ready to go when you push the “acquire” button. Furthermore, as you’ll see, little useful information is present in the acquired EELS spectrum unless your specimen is very thin. Disko (1986) succinctly summarized the important experimental variables. We’ve already told you back in Chapter 37 how to control most of these factors. In this chapter, we’ll go through all the parameters and indicate reasonable values for each.

- *Beam energy E_0 :* It’s probably best to use the highest E_0 , unless doing so causes displacement damage or surface sputtering. A higher E_0 does reduce the scattering cross section and so you get reduced edge intensity. However, as E_0 increases, the plural-scattering background intensity falls faster than the edge intensity and so the ionization-edge signal-to-background increases and this is useful. The increase in signal-to-background varies with the particular edge but it is never a strong variation; so while we make a lukewarm recommendation to use the highest kV, it’s not a good reason to justify purchasing an IVEM.
- *Convergence semiangle α :* You know how to control α with the C2 aperture and/or the C2 lens, but α is only important in the quantification process if it is larger than β . So if you op-

erate in TEM image or diffraction mode with a broad parallel beam, rather than STEM mode, you can ignore any effects of α ; otherwise, use the correction factor we give in Section 39.7.

- *Beam size and current:* You control these factors by your choice of electron source, C1 lens, and C2 aperture. As usual, the beam size is important in limiting the spatial resolution in STEM mode, and the beam current controls the signal intensity. You have to make the same compromise between improved spatial resolution and loss of signal intensity, or vice versa, as we discussed at some length in Chapter 36 for XEDS.
- *Specimen thickness:* The specimen must be thin because then the plural-scattering contributions to the spectrum are minimized and quantification is most straightforward.

Making your specimen as thin as possible is the most important part of EELS.

If your specimen is too thick, then you’ll have to use deconvolution procedures to remove the effects of plural scattering. So we’ll tell you how to determine the thickness from your spectrum and how to decide if you need to deconvolute the spectrum.

- *Collection semiangle β :* You know from Section 37.4 how to measure β in all operating modes. If you need lots of intensity and are happy with limited spatial resolution, use TEM-image mode with no objective aperture ($\beta \sim 100$ mrad). A small spectrometer entrance aperture would provide better energy resolution at the same time. If you want a small β to prevent contributions to the spectrum from high-angle scattering, use diffraction mode (TEM or STEM) and a small spectrometer entrance aper-

ture for good energy resolution. In the STEM case you also get good spatial resolution.

Remember that a 5-mm entrance aperture gives $\beta \sim 5$ mrad at a camera length of ~ 800 mm.

Generally, for microanalysis $\beta \sim 1$ –10 mrad is fine, so long as it's less than the Bragg angle for your particular specimen and orientation; but for EELS imaging, which we discuss in Section 40.3, 100 mrad may be necessary.

- *Energy resolution:* ΔE is limited by your electron source, assuming you've focused the spectrum. In a SEELS, the slit width can control ΔE . Microanalysis and imaging do not require the best ΔE and ~ 5 eV will generally suffice. You really only need the best ΔE for ELNES, and plasmon-shift studies, both of which are somewhat esoteric pursuits. Use an FEG source and a PEELS if you want to do this kind of thing.
- *Energy-loss range and spectrum dispersion:* The full spectrum extends out to the beam energy E_0 , but the useful portion only extends to about 1 keV. Above this energy loss, the intensity is very low, and microanalysis by XEDS is both easier and more accurate, although arguably a little less sensitive. So you rarely need to collect a spectrum above about 1 keV and therefore, with a minimum of 1024 channels in the MCA display, 1 eV/channel is always a good starting point. You can easily select a higher display resolution if you want to look at a more limited region of the spectrum or if you want to see detail with $\Delta E < 1$ eV.
- *Signal processing:* In SEELS, remember that your two choices (in which the spectral intensity is determined by the total current on the scintillator) are analog processing or single electron counting. You should collect the high-intensity, low-loss portion of the spectrum in analog mode and the lower-intensity, high-loss region in single-electron mode. The change in counting mode is most conveniently made at the same point in the collection process as the gain change. Set this point around 50–100 eV, well above the plasmon range but at lower E than most ionization edges. There is no equivalent of this variable in PEELS.
- *Dwell time:* In SEELS, typical dwell times are in the range from 10 ms to 1 s per channel, depending on the number of channels in the spectrum and the intensity necessary to extract the analytical result. Because the magnetic prism is not very stable, it is unwise to collect spectra

for periods longer than a few minutes. If more counts are required you should sum several spectra (see below), each recorded over a limited time range, with intermediate checks on the calibration. In PEELS, you set the dwell time (or integration time) such that the maximum intensity in the spectrum doesn't saturate the photodiode array, i.e., stay below 16,000 counts per acquisition in the most intense channel and sum as many spectra as you need to give sufficient counts for analysis.

- *Number of sweeps:* It is better in both SEELS and PEELS to sum many spectra rather than gather one SEELS spectrum for several minutes, or saturate the PEELS detector. Remember also that each sweep in SEELS should be a reverse scan from high to low energy. Furthermore, if the intense zero loss has to be recorded, several minutes should elapse between each scan to ensure that the scintillator after-glow has subsided to below the normal dark-current output of the detector. In PEELS, multiple acquisitions can give rise to artifacts, as we discussed in Section 38.5.

So now you can see why EELS is not a straightforward turn-key operation. You must have a very good understanding of your TEM and spectrometer optics; be aware that the system is not very stable, needs recalibrating regularly and, PEELS, particularly, is prone to artifacts.

39.2. WHAT SHOULD YOUR SPECTRUM LOOK LIKE?

Before you analyze a particular spectrum, you should check three things:

- Display the zero-loss peak to ensure that the spectrometer is giving you the necessary ΔE , if this is important.
- Look at the low-loss portion of the spectrum; this gives you an idea of your specimen thickness.
- Look for the expected ionization edges. If you can't see any edges, your specimen is probably too thick.

The first of these tasks is not critical, as we noted earlier. Regarding the second task, you'll see in Section 39.5 that, to a first approximation, if the plasmon peak intensity is less than about one-tenth the zero-loss peak, then the specimen is thin enough for microanalysis. Otherwise, you'll

probably have to deconvolute plural-scattering effects from your experimental spectrum. For the third task, you should ideally see a discrete edge on a smoothly varying background, but you need to see at least a change in slope in the background intensity at any expected edge energies. The Gatan ELP program can identify and quantify such hidden peaks (see Section 1.5). If the background intensity is noisy, it will make quantification more difficult.

An important parameter in determining the quality of your spectrum is the signal-to-background ratio which, in EELS, we call the jump ratio.

This is the ratio of the maximum edge intensity (I_{\max}) to the minimum intensity (I_{\min}) in the channel preceding the edge onset, as shown in Figure 39.1.

If the jump ratio is above ~5, for the carbon K edge at 284 eV from a standard (< 50 nm thick) carbon film at 100 kV, then your TEM-EELS system is operating satisfactorily. Figure 39.1 is a well-defined edge from a film of amorphous carbon. If you can't get such a jump ratio, then perhaps you need to realign the spectrometer, or find a thinner specimen. The jump ratio should increase with increasing kV.

39.3. QUALITATIVE MICROANALYSIS

As with XEDS, you should always carry out qualitative microanalysis to ensure that you have identified all the features in your spectrum. Then you can decide which edges to use for microanalysis.

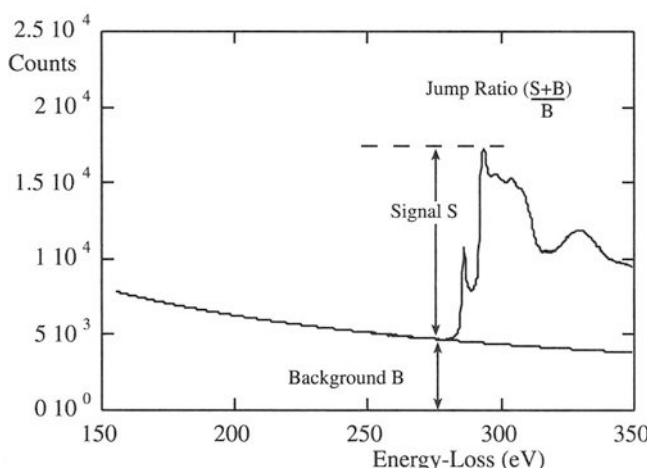


Figure 39.1. Definition of the jump ratio of an ionization edge which should be about 5–10 for the carbon K edge if the EELS is well aligned.

Qualitative microanalysis using ionization edges is very straightforward. Unlike XEDS, there are actually very few artifacts that can be mistaken for an edge. The most prominent artifact that may lead to misidentification is the so-called ghost edge from diode saturation in PEELS spectra (see Section 38.5). So long as you calibrate the spectrum to within 1–2 eV you can unambiguously identify the edge energy.

We identify the ionization edge as the energy loss at which there is a discrete increase in the slope of the spectrum; this value is the edge onset, i.e., E_C , the critical ionization energy.

You have to be careful here: sometimes you'll see the edge energy defined somewhat arbitrarily half-way up the edge, e.g., at the π^* peak on the front of a C K edge. There is no strict convention, and very often L and M edges do not have sharp onsets anyhow.

Examination of a portion of a spectrum, such as that shown back in Figure 38.6, is usually sufficient to let you draw a definite conclusion about the identity of the specimen, which is BN on a C support film. In addition, it is wise to compare your spectrum with reference spectra from one of several EELS libraries that are available (Zaluzec 1981, Ahn and Krivanek 1983, Colliex 1984).

Remember that there are families of edges (K, L, M, etc.) just as there are families of peaks in X-ray spectra. As a rule of thumb, quantification is equally easy with K and L edges, but the accuracy of K-edge quantification is slightly better. Up to Z = 13 (Al) we usually use K edges, because any L edges occur at very low energy and are masked by the plasmon peak. Above Z = 13 you can use either K or L edges. Sometimes, there is the question of which edge is most visible. The K-edge onset is generally a bit sharper than the L edge, which consists of both the L_2 and L_3 edges and so may be somewhat broader. This is not always the case.

L edges for Z = 19–28 and 37–45 are characterized by intense near-edge structure, called white lines. M edges for Z = 55–69 have similar intense lines.

These white lines, which we first saw back in Figure 38.9, are so named because of their appearance in early, photographically recorded energy-loss spectra; more details are given in Section 40.1. If you have to use the M, N, or O edges without any white lines, you should know that they are very broad, with an ill-defined threshold, and quantification is only possible with standards, as we'll see shortly.

The energy-loss spectrum clearly does not lend itself to a quick “semiquantitative” analysis, as we can do with XEDS. For example, the spectrum in Figure 38.6 comes from equal numbers of B and N atoms, but the intensities in the B and N edges are markedly different. This difference arises because of the variation in ionization cross section with E , the strongly varying nature of the plural-scattering background, and the edge shape, which causes the C and N K edges to ride on the tails of the preceding edge(s).

Example

Sometimes, qualitative analysis is all that you need to do. Figure 39.2A and Figure 39.2B show images and spectra from two small precipitates in an alloy steel. The spectra show a Ti L₂₃ edge in both cases, and C and N K edges in Figure 39.2A and Figure 39.2B, respectively. It does not take much effort to deduce that the

first particle is TiC because it is the only known carbide of Ti, but the nitride could be either TiN or Ti₃N. To determine which of the two it is, you have to carry out full quantification, which we’ll discuss shortly. You should note that such clear discrimination between TiC and TiN in Figure 39.2 would be difficult using windowless XEDS, because the energy resolution is close to the separation of the Ti L (452 eV) and the N K (392 eV) X-ray peaks. In addition, the DPs from both phases are almost identical, so this problem is a perfect one for EELS.

39.4. QUANTITATIVE MICROANALYSIS

To quantify the spectrum, you have to extract intensity in the ionization edge(s) by removing the plural-scattering background and integrating the intensity (I) in the edge.

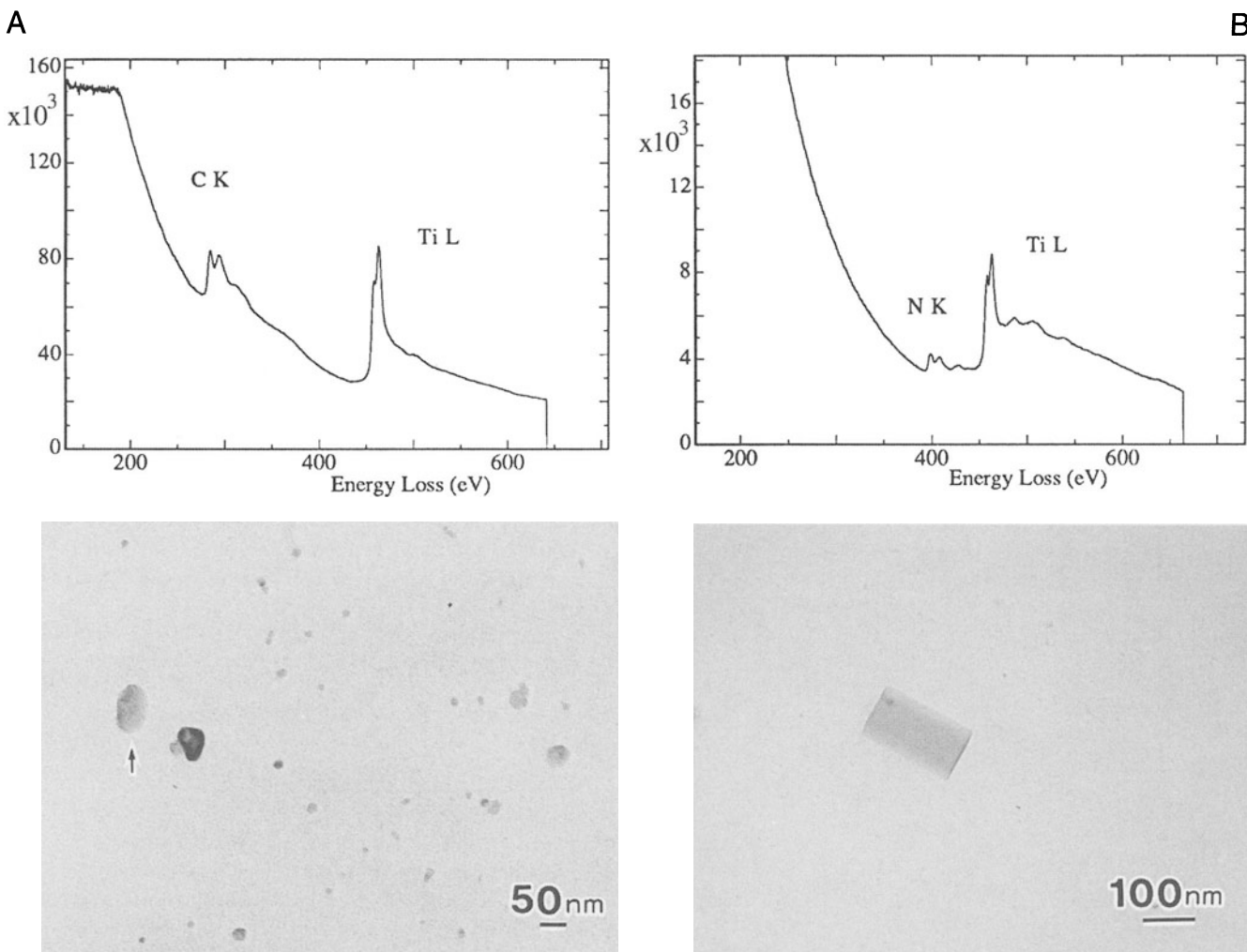


Figure 39.2. Images of small precipitates in a stainless steel specimen, and the corresponding ionization edges showing qualitatively the presence of Ti, C, and N. Thus the precipitates can be identified as (A) TiC and (B) TiN, respectively.

Then you have to determine the sensitivity factor, that is, you need to determine the number of atoms N responsible for I . This sensitivity factor is called the “partial ionization cross section.” We’ll see that it plays a similar role to the k_{AB} factor in X-ray microanalysis. If you go back and look at Figure 38.5, you’ll see how an ionization edge is built up from several contributions. The process of quantification in essence involves stripping away (or ignoring) the various contributions until you’re left with Figure 38.5A, which contains the single-scattering “hydrogenic” edge intensity.

39.4.A. Derivation of the Equations for Quantification

The equations we use for quantitative analysis have been derived, refined, and applied by Egerton and co-workers. The following derivation is a summary of the full treatment by Egerton (1996), which itself draws on work carried out over the preceding two decades.

We’ll assume that we are quantifying a K edge, although the basic approach can be used for all edges. The K-shell intensity above background, I_K , is related to the probability of ionization, P_K , and the total transmitted intensity, I_T

$$I_K = P_K I_T \quad [39.1]$$

This equation assumes that the intensities are measured over the complete angular range (0 – 4π sr), which of course is not the case, but we’ll correct for this later. In a good thin specimen we can approximate I_T to the incident intensity, neglecting backscatter and absorption effects. Now, this is the important point:

If we assume also that the electrons contributing to the edge have only undergone a single ionization event, then we can easily obtain an expression for P_K

$$P_K = N \sigma_K \exp\left(\frac{t}{\lambda_K}\right) \quad [39.2]$$

where N is the number of atoms *per unit area* of the specimen (thickness t) that contribute to the K edge. The assumption of a single K-shell ionization event with cross-section σ_K is reasonable, given the large mean free path (λ_K) for ionization losses; but it explains why you have to make thin specimens. It also means that the exponential term is very close to unity, and so

$$I_K \approx N \sigma_K I_T \quad [39.3]$$

and therefore

$$N = \frac{I_K}{\sigma_K I_T} \quad [39.4]$$

Thus we can measure the absolute number of atoms per unit area of the specimen simply by measuring the intensity above background in the K edge and dividing it by the total intensity in the spectrum and the ionization cross section. We can easily extend this expression to a spectrum containing two edges from elements A and B, in which case the total intensity drops out and we can write

$$\frac{N_A}{N_B} = \frac{I_K^A \sigma_K^B}{I_K^B \sigma_K^A} \quad [39.5]$$

Similar expressions apply to L, M edges, etc., and combinations of edges can be used. So you see that if you are quantifying more than one element then you don’t need to gather the zero-loss peak, and this makes life much easier for the spectrometer scintillator or diode array.

In both equations 39.4 and 39.5 we assumed that we could accurately subtract the background under the ionization edge and that we know σ . Unfortunately, as you’ll see, both background subtraction and determination of σ are nontrivial and limit the accuracy of quantification. We will discuss these points later, but initially we must take account of the practical realities of spectrum acquisition and modify the equations accordingly.

First, you can’t gather the whole of the energy-loss spectrum out to the beam energy, E_0 , because above 1–2 keV the intensity decreases to a level close to the system noise. Furthermore, while ionization-loss electrons can theoretically have any energy between E_C and E_0 , in practice the intensity in the edge falls to the background level within about 100 eV of the ionization threshold, E_C . In addition, the background extrapolation process becomes increasingly inaccurate beyond about 100 eV, and so it is imperative to restrict the integration of spectral intensities to some window, Δ , usually in the range of 20–100 eV. So we modify equation 39.4 to give

$$I_K(\Delta) = N \sigma_K(\Delta) I_T(\Delta) \quad [39.6]$$

The term $I_T(\Delta)$ is more correctly written as $I_\ell(\Delta)$, where I_ℓ is the intensity of the zero-loss (direct beam) electrons combined with the low-loss electrons over an energy loss window Δ . Only if we have true single scattering can we use I_T , and we’ll discuss the conditions for this later.

As we discussed, EELS has the tremendous advantage that the energy-loss electrons are predominantly forward-scattered and so you can easily gather most of the signal. As a result, the technique is inherently far more efficient than XEDS. However, because we cannot physically collect the spectrum over 4π sr, but are limited by our

choice of collection semiangle β , we must further modify the equation and write

$$I_K(\beta\Delta) = N\sigma_K(\beta\Delta)I_\ell(\beta\Delta) \quad [39.7]$$

The factor $\sigma_K(\beta\Delta)$ is termed the “partial ionization cross section,” from this equation, therefore, the absolute quantification for N is given by

$$N = \frac{I_K(\beta\Delta)}{I_\ell(\beta\Delta)\sigma_K(\beta\Delta)} \quad [39.8]$$

For a ratio of two elements A and B , the low-loss intensity drops out

$$\frac{N_A}{N_B} = \frac{I_K^A(\beta\Delta)\sigma_K^B(\beta\Delta)}{I_K^B(\beta\Delta)\sigma_K^A(\beta\Delta)} \quad [39.9]$$

We can draw a direct analogy between this equation and the Cliff–Lorimer expression (equation 35.2) used in thin-foil XEDS. In both cases, the composition ratio C_A/C_B or N_A/N_B is related to the intensity ratio I_A/I_B through a sensitivity factor, which we call the k_{AB} factor in XEDS and which in electron spectrometry is the ratio of two partial cross sections, σ^B/σ^A .

Remember that the major assumption in this whole approach is that the electrons undergo *a single scattering event*. In practice, it's difficult to avoid plural scattering, although in very thin specimens the approximation remains valid, if errors of $\pm 10\text{--}20\%$ are acceptable. If plural scattering is significant then the spectrum must be deconvoluted, and we will discuss ways to do this in Section 39.6 when we describe the limitations of specimen thickness. You should also note when using the ratio equation that your analysis is a lot better if the two edges are similar in shape, i.e., both K edges or both L edges, otherwise the approximations inherent in equation 39.9 will be less accurate.

In summary then, these equations give us an absolute value of the atomic content of the specimen or a ratio of the amounts of two elements. You have to carry out two essential practical steps:

- The background subtraction to obtain I_K .
- The determination of the partial ionization cross section $\sigma_K(\beta\Delta)$.

So now you can see why it is important to know β .

39.4.B. Background Subtraction

The background intensity comes from plural-scattering events which are usually associated with outer-shell interactions. In the spectrum the background appears as a

rapidly changing continuum decreasing from a maximum just after the plasmon peak at about 15–25 eV, down to a minimum at which it is indistinguishable from the instrumental noise, typically when $E \sim 1\text{--}2$ keV. In addition to the true plural scattering, there is also the possibility of single-scattering contributions to the background from the tails of preceding ionization edges. Because of the complexity of the many combinations of plural-scattering processes, it has not proven possible to model the background from first principles to the same degree that is possible in XEDS using variations on Kramers' Law. There are two ways commonly used to remove the background:

- Curve fitting.
- Using difference spectra.

We'll now describe these in some detail.

Curve Fitting: You select a window δ in the background before the edge onset and fit a curve to the channels. Then you extrapolate the curve over the desired energy window Δ under the edge. This process is shown schematically in Figure 39.3, and experimentally in Figure 39.4.

We assume that the energy dependence of the background has the form

$$I = A E^{-r} \quad [39.10]$$

where I is the intensity in the channel of energy loss E , and A and r are constants for a particular curve fit. The fitting parameters are only valid over a limited energy range because they depend on E . The exponent r is typically in the

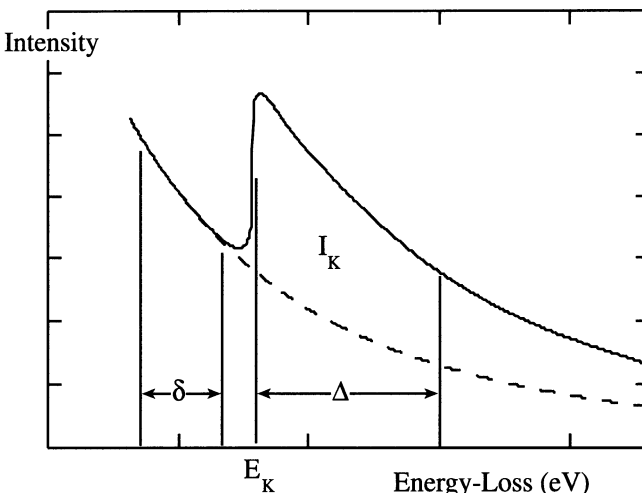


Figure 39.3. The parameters required for background extrapolation and subtraction under an ionization edge. The pre-edge fitting window δ is extrapolated over a post-edge window Δ then subtracted to give the edge intensity I_K .

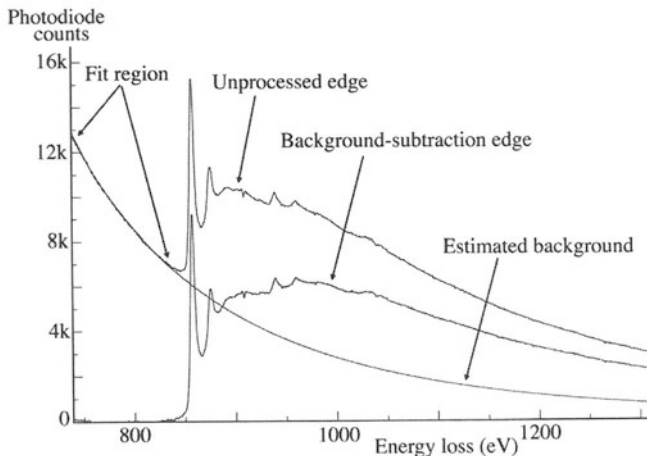


Figure 39.4. A Ni L_{2,3} edge before and after background subtraction. The fit region before the unprocessed edge is extrapolated to give the estimated background, which is then removed, leaving the background-subtracted edge.

range 2–5, but A can vary tremendously. We can see some trends in how r varies. The value of r decreases as:

- The specimen thickness, t , increases.
- The collection semiangle, β , increases.
- The electron energy loss, E , increases.

The fit to the tail of a preceding edge also shows a similar power-law dependence on the plural-scattering background, and may be fitted in a similar manner, i.e., $I = BE^{-r}$. The energy range δ over which you fit the background should not be $<\sim 10$ channels, and at most not $>\sim 30\%$ of E_K . In practice, however, you might not be able to fit the background over such a wide window if another edge is present within that range.

You should choose the extrapolation window, Δ , such that the ratio of the finish to the start energies, $E(\text{finish})/E(\text{start})$, is <1.5 . In Figure 39.4, the extrapolation window (~ 450 eV) is a little larger than ideal. So, Δ is smaller for lower edge energies. Using larger windows, although improving the statistics of the total edge integration, eventually reduces the accuracy of the final quantification because the fitting parameters A and r are only valid over ~ 100 eV. If there's a lot of near-edge structure, either use a larger Δ to minimize its effect or avoid it in the extrapolation window, unless the quantification routine can handle it.

Instead of the simple power-law fit, you can use any expression such as an exponential, polynomial, or log-polynomial, so long as it provides a good fit to the background and gives acceptable answers for known specimens. Polynomial expressions can behave erratically if you extrapolate them over a large Δ , so use them cautiously. Generally, the power law seems adequate for most

purposes except close to the plasmon peaks ($E <\sim 100$ eV). Clearly, the background channels closest to the edge onset will influence the extrapolation most strongly, and various weighting schemes have been proposed. A noisy spectrum will be particularly susceptible to poor fitting, unless some type of weighting is used.

We can judge the “goodness of fit” of a particular power-law expression qualitatively by looking at the extrapolation to ensure that it is heading toward the post-edge background and not substantially under- or over-cutting the spectrum. More quantitatively, we can assign a χ^2 , chi-squared, value based on a linear least-squares fit to the experimental spectrum. The least-squares fit can be conveniently tied in with a weighting scheme using the expression

$$\chi^2 = \sum_i \frac{(y - y_i)^2}{y^2} \quad [39.11]$$

where y_i is the number of counts in the i th channel and $y = \ln_e I$. The squared term in the denominator ensures suitable weighting of the channels close to the edge.

Difference Spectra: You can also remove the background using a first-difference approach (which is equivalent to differentiating the spectra). This method is particularly suited to PEELS since it simply involves taking two spectra, offset in energy by a few eV, and subtracting one from the other. As shown in Figure 39.5, the difference process results in the slowly varying intensity (i.e., background) being reduced to zero and the rapidly varying intensity features (i.e., ionization edges) showing up as classical difference-peaks, similar to what you may have seen in an Auger spectrum. This is the *only* way to remove the background if your specimen thickness changes over the area of analysis, and it also has the advantage that it sup-

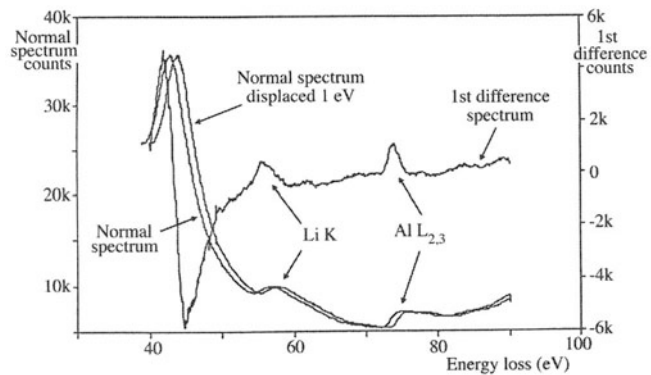


Figure 39.5. First-difference method of background subtraction, showing two PEELS spectra from a specimen of Al-Li displaced by 1 eV and subtracted to give a spectrum in which the background intensity falls to zero and the small Li K and Al L_{2,3} edges are clearly revealed.

presses spectral artifacts common to PEELS, particularly the channel-to-channel gain variation.

Another kind of difference method involves convoluting the experimental spectrum with a filter function. A top-hat filter function, similar to the one we described in Section 35.2 for background subtraction in XEDS, gives a second-difference spectrum which also removes the background but exacerbates some artifacts.

39.4.C. Edge Integration

The edge integration procedure you use depends on how you removed the background. If you used a power-law approach, then remember that there is a limit over which the edge integration window Δ is valid. The value of Δ should be large enough to maximize the integrated intensity, but not so large that the errors in your background extrapolation dominate. Often, the presence of another edge limits the upper end of the integration window. The lower end is usually defined from the edge onset, E_K , but if there is strong near-edge structure, such as in the B K edge or the Ca L₂₃ edge, then your integration window should start at an energy above these, unless the quantification schemes can handle fine structure effects (see below). If you subtracted the background using a first-difference approach, then you determine the peak intensity by fitting the experimental spectrum to a reference spectrum from a known standard using multiple least-squares fitting. We'll talk more about this when we discuss deconvolution of spectra.

39.4.D. The Zero-Loss Integral

Remember from equation 39.8 that if you want *absolute* quantification of N , then you have to integrate the low-loss spectrum I_ℓ out to about 50 eV. In a SEELS you should always do this using a reverse scan to avoid any problems with after-glow of the scintillator, and in PEELS you must be careful to integrate for a short enough time so you don't saturate the diode array. If you are doing a ratio, then I_ℓ is not needed (equation 39.9).

39.4.E. The Partial Ionization Cross Section

There are several ways we can determine the partial ionization cross section, $\sigma(\beta\Delta)$, which is the sensitivity factor relating intensity (I) to the number of atoms (N). We either use a theoretical approach or compare the experimental spectra with known standard spectra.

Theoretical Calculation: The most common approach is that due to Egerton (1979, 1981), who produced two short computer programs to model the K- and L-shell partial cross sections. The programs are called SIGMAK

and SIGMAL, respectively. They are public domain software and are available in Gatan's ELP software, but the code is also given in Egerton's book.

The cross sections are modeled by approximating the atom in question to an isolated hydrogen atom with a charge on the nucleus equal to the atomic number Z of the atom, but with no outer-shell electrons.

While at first sight this is an absurd approximation, the approach is tractable because the hydrogen-atom wave function can be expressed analytically by Schrödinger's wave equation, which can be modified to account for the increased charge. Because this treatment neglects the outer-shell electrons, it is best suited to K-shell electrons, and Figure 39.6 shows a comparison between the measured N K-shell intensity and that computed using SIGMAK. As you can see, the SIGMAK hydrogenic model essentially ignores the near-edge and post-edge fine structure (which would be absent in the spectrum from a hydrogen atom), but still gives a very good fit, on average, to the experimental edge. Figure 39.7 compares the Cr L edge with the SIGMAL model. The L-shell fit is almost as good as the K fit, but the white lines are imperfectly modeled. These programs are very widely used since they are simple to understand and easy and quick to apply.

There is another theoretical approach which uses empirical parameterized equations to calculate the terms that modify σ for the effects of β and Δ . Both Joy (1986b) and Egerton (1989) have given relatively simple expressions, amenable to evaluation on a hand-held calculator, which you can look up if you wish. Joy's parameterization approach and the SIGMAK/SIGMAL models give good agreement, as shown in Figure 39.8. There are more com-

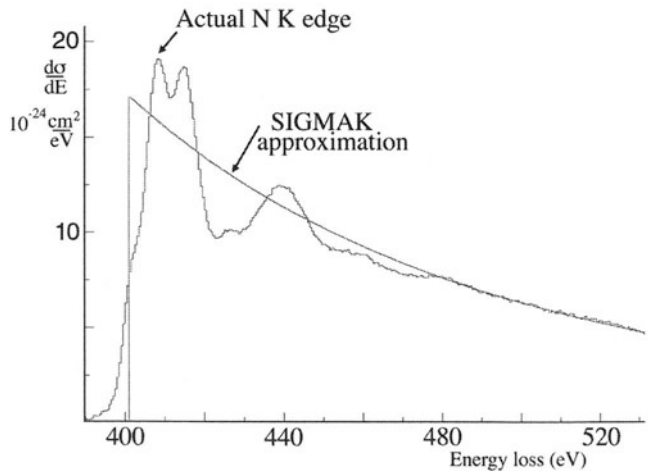


Figure 39.6. Comparison of an experimental N K edge and the hydrogenic fit to the edge using the SIGMAK program.

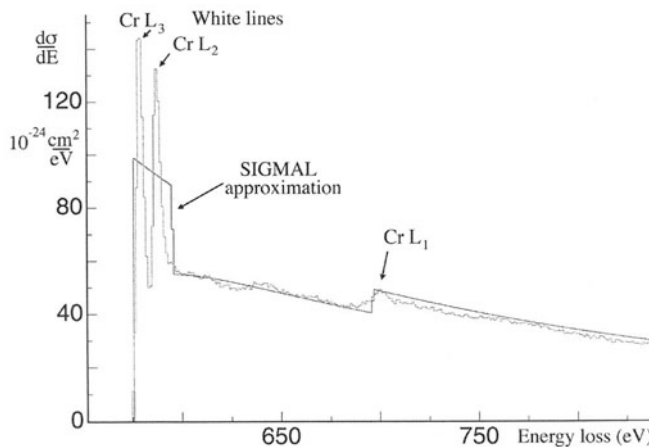


Figure 39.7. Comparison between an experimental Cr $L_{2,3}$ edge and a modified hydrogenic approximation to the edge obtained using the SIGMAL program. The fit makes no attempt to model the intense white lines, but only makes a rough estimate of their average intensity.

plex methods available which calculate the cross section in a more realistic way than the hydrogenic model, e.g., using Hartree–Slater models or atomic-physics approaches, which are better for the more complex L and M edges (Rez 1989). Egerton (1993) has compared experimental and theoretical cross sections, and the M-shell data (which are the worst case) are shown in Figure 39.9. The data are actually plotted in terms of the oscillator strength f (which is a measure of the response of the atom to the incident electron). This term is the integral of the generalized oscillator strength, which is proportional to the differential cross section, so just think of f as proportional to σ . There is still relatively poor agreement between experiment and theory for the M shell, as well as between the atomic and hydrogenic theoretical models. Similar data in Egerton’s paper show

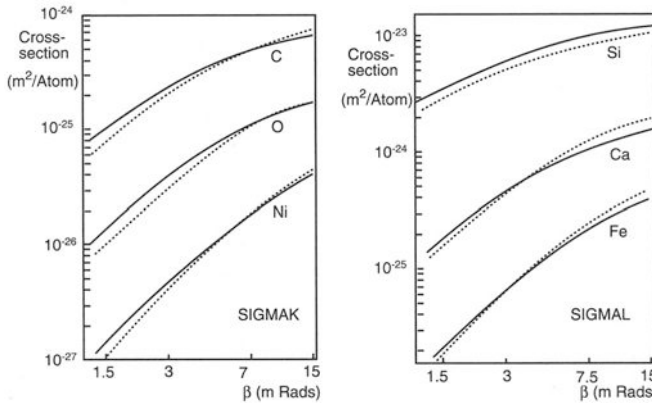


Figure 39.8. Comparison of the SIGMAK and SIGMAL hydrogenic models (full lines) for the ionization cross section with the parametric model (dotted lines).

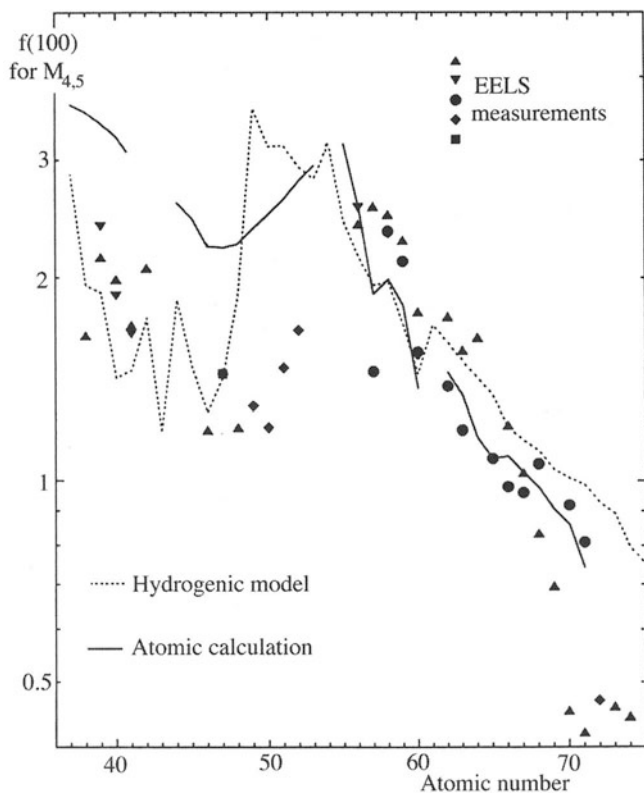


Figure 39.9. Comparison of the experimental and theoretical approaches to determination of the M-shell ionization cross section shown in terms of the variation in the dipole oscillator strength (f) as a function of atomic number. The data points are different experimental measurements, the solid line is a fundamental atomic calculation, and the dotted line is a hydrogenic calculation.

better agreement for K and L shells. These models, while more precise, require substantially longer computing time, but this is fast becoming less of a problem. Given the other sources of error in EELS microanalysis, you rarely need to go to such lengths to obtain a better value of $\sigma(\beta\Delta)$, and you should generally stick with the SIGMAK/L approach for routine quantification.

Experimental Determination: Rather than calculating σ theoretically, you can generate a value experimentally using known standards. This approach is, of course, exactly analogous to the experimental k -factor approach for XEDS quantification in which the cross section is automatically included (along with the fluorescence yield and other factors). It is surprising at first sight that the classical XEDS approach of using standards has not been widely used in EELS, but the reason is obvious when you remember the large number of variables that affect the EELS data. The standard and unknown must have the same thickness and the same bonding characteristic, and the spectra must be gathered under identical conditions; in particular β , Δ , E_0 , and t must be the same.

Again, it is the problem of thickness measurement that appears to be the main limitation to improving the accuracy of microanalysis.

Despite these limitations, data are available comparing cross sections of various elements, relative to oxygen (Hofer *et al.* 1988), just as k factors are determined relative to Si or Fe. Malis and co-workers (Malis *et al.* 1987, Malis and Titchmarsh 1988) have also produced a large number of experimental cross sections for light-element compounds. It is intriguing to note that the experimental approach appears increasingly popular in EELS, while in XEDS the reverse trend, toward more theoretical modeling of k factors, seems to be the case!

The SIGMAK/L programs may introduce large errors when quantifying the lightest metallic elements, Li and Be, so for the most accurate quantification of these elements the standards approach is still the best.

Example

In a study of Al-Li alloys (Liu and Williams 1989), a homogeneous sample of Al-12.7 at.% Li was used as a standard; t was determined from the relative intensities of the first plasmon peak and the zero-loss peak. The integrated intensity ratio for the Li K/Al L_{2,3} edges was determined after background subtraction to be 0.106 ± 0.006 . This number was the average of six separate spectra, and the errors were based on a student t analysis at the 95% confidence limit. From equation 39.9, the Li/Al partial-cross-section ratio was calculated to be 1.37 ± 0.07 . An Al-Li specimen containing an intermetallic of unknown Li content was then examined and 13 spectra obtained which gave an average Li K/Al L_{2,3} intensity ratio of 0.188 ± 0.009 . Combining this ratio with the partial ionization cross section and substituting back into equation 39.9 gives the composition of the intermetallic as Al-20.5±1 at.%Li. This result and others are given in Figure 39.10, which shows the low-Li portion of the Al-Li phase diagram, determined through direct Li composition measurements. For comparison, the partial ionization cross section was also determined from the SIGMAK/L programs, and the ratio was 0.969, ~30% less than that obtained using the standard. While this is a large difference compared to most SIGMAK/L calculations, it still sounds a note of caution against unquestioning use of the calculated cross sections.

In summary, there are two approaches to the determination of $\sigma(\beta\Delta)$: theoretical calculation and experimental measurement. In contrast to XEDS, the theoretical approaches dominate. There is good evidence that, particularly for the lighter elements for which EELS is best suited, the simple and quick hydrogenic model is usually ade-

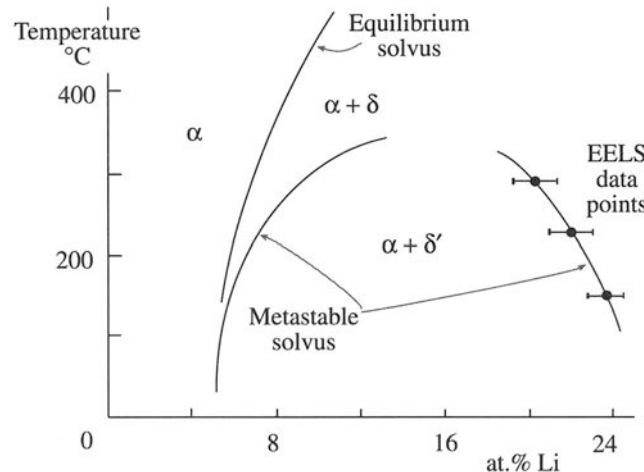


Figure 39.10. The Al-Li phase diagram determined by EELS, showing a variation in the Li content of the metastable Al_3Li (δ') phase as the temperature is raised. The equilibrium phases are α (Al-Li) solid solution and δ (Al-Li) intermetallic.

quate. However, for the heavier elements, where the M shell is used for analysis, tedious experimental data are still the best option. Of course, for such elements it is probably better to revert to XEDS analysis anyhow.

So now we're in a position where we have all the data needed to solve the quantification equations. However, our assumption all along has been that the spectra were the result of single scattering and we neglected plural scattering. Now in practice there will *always* be some plural-scattering contribution to the ionization edges.

The combination of a plasmon interaction and an ionization will show up as a bump about 15–25 eV past the onset of the edge.

This effect is shown schematically back in Figure 38.5F and, if you look ahead, in Figure 39.15. So how do we go about correcting for this? We can either make our specimens so thin that plural scattering is negligible, or we can deconvolute the spectra. The former approach is possible, but you have to be lucky or exceptionally skilled at specimen thinning. The latter approach is mathematically simple, but can be misleading if not done properly, so we will need to examine deconvolution in more detail; but let's look at how we determine t because EELS offers us a simple method for this.

39.5. MEASURING THICKNESS FROM THE ENERGY-LOSS SPECTRUM

There is thickness information in the energy-loss spectrum since the amount of all inelastic scatter increases with

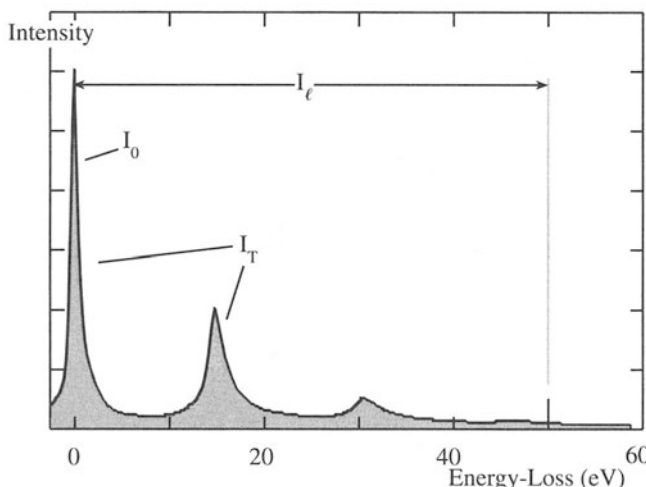


Figure 39.11. Definition of the zero-loss intensity I_0 , the total intensity I_T , and the low-loss (I_ℓ) intensity required for thickness determination.

specimen thickness. In principle we have to measure the intensity under the zero-loss peak (I_0) and ratio this to the total intensity in the spectrum (I_T), as defined in Figure 39.11. But in practice the intensity in the EELS spectrum falls so rapidly with increasing energy loss that we can reasonably approximate I_T to the intensity in the low-loss portion of the spectrum I_ℓ , out to about 50 eV. The relative intensity of the zero loss and the total intensity is governed by the average mean free path (λ) for energy losses up to 50 eV, and thus

$$t = \lambda \ln \left(\frac{I_\ell}{I_0} \right) \quad [39.12]$$

All we need is to determine λ for the specimen, and we get this from a parameterization based on many experimental measurements (see Malis *et al.* 1988). The expression is

$$\lambda = \frac{106 F E_0}{\left\{ E_m \ln \left(\frac{2\beta E_0}{E_m} \right) \right\}} \quad [39.13]$$

where λ is in nm, E_0 in keV, β in mrad, F is a relativistic correction factor, and E_m is the average energy loss in eV which, for a material of average atomic number Z , is given by

$$E_m = 7.6 Z^{0.36} \quad [39.14]$$

The relativistic factor (F) is given by

$$F = \frac{\left\{ 1 + \frac{E_0}{1022} \right\}}{\left\{ 1 + \left(\frac{E_0}{511} \right)^2 \right\}} \quad [39.15]$$

You can easily store these equations in the TEM computer or in your calculator and they give an accuracy for t of better than $\pm 20\%$.

If indeed your specimen is so thin that only single scattering occurs, then you can use a similar expression but assume that the only significant scatter was a single plasmon event. Thus

$$t = \lambda_p \frac{I_p}{I_0} \quad [39.16]$$

where λ_p is the plasmon mean-free path (see Table 38.2), I_p is the intensity in the first (and only) plasmon peak, and I_0 is the intensity in the zero-loss peak.

The method has advantages over other thickness measurement techniques in that you can apply it to any specimen, amorphous or crystalline, over a wide range of thicknesses.

If plural scattering is significant, then your quantification results become unreliable.

A typical ball-park figure is that, if the intensity in the first plasmon peak is greater than one-tenth the zero-loss intensity, then your specimen is too thick.

Another way of saying this is that, if $t > 0.1\lambda_p$, then errors $>\sim 10\%$ are expected, as shown in Figure 39.12. Of course,

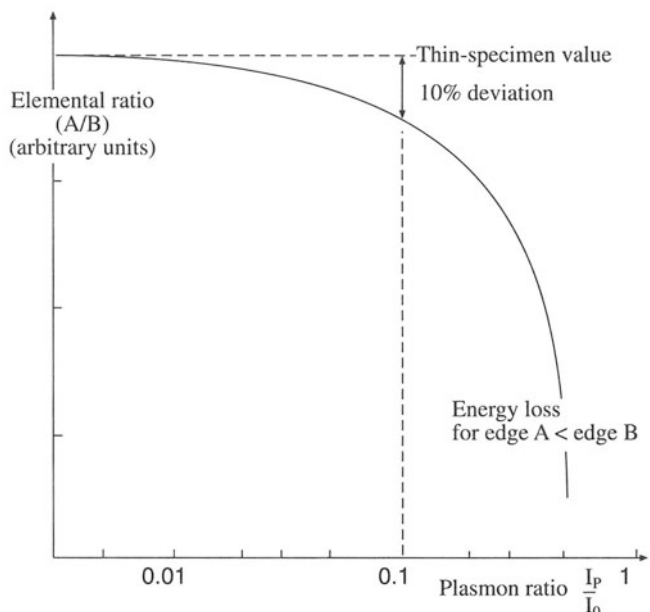


Figure 39.12. The intensity ratio of two ionization edges (A/B) as a function of specimen thickness. The thickness is plotted in terms of the ratio of the plasmon to the zero-loss intensity (I_p/I_0). The intensity ratio is affected significantly when I_p is above about $0.1 I_0$.

one way round this problem is to use very thin foils, but often you can't produce thin enough specimens. Murphy's law says that the area you're interested in will usually be too thick. Then you have to deconvolute the spectra to make the single-scattering assumption valid.

39.6. DECONVOLUTION

We saw back in Figure 38.5 that the effect of plural scattering is to add intensity to the ionization edge, mainly as a result of combined inner- and outer-shell losses.

We can represent the experimental ionization edge as a true single-scattering (hydrogenic) edge convoluted with the plasmon, or low-loss, spectrum.

The aim of the deconvolution process therefore, as shown schematically in Figure 39.13, is to extract the single-scattering intensity distribution. We'll describe two methods, the Fourier-Log and the Fourier-Ratio, which are both based on the work of Egerton *et al.* (1985), and both methods are incorporated in the Gatan ELP proprietary software. Strictly speaking, the deconvolution should be carried out in both the energy dimension and the angular dimension, but in practice all the routines ignore the angular dimension; this simplification introduces a small systematic error into any deconvolution. The error is usually <10% up to typical energy losses below about 1 keV, so we can usually ignore it. A smaller β increases the deconvolution error, since the plural-scattered electrons have a wider angular distribution and so more of them are excluded as β decreases.

The *Fourier-Log* method removes the effects of plural scattering from the whole spectrum. The technique

describes the spectrum in terms of the sum of individual scattering components, i.e., the zero-loss (elastic contribution) plus the single-scattering spectrum plus the double-scattering spectrum, etc. Each term is convoluted with the "instrument response function," which is a measure of how much the spectrometer degrades the generated spectrum; in the case of a PEELS, this is the point-spread junction we described in Section 37.3. The Fourier transform of the whole spectrum (F) is then given by

$$F = F(0) \exp\left(\frac{F(1)}{I_0}\right) \quad [39.17]$$

where $F(0)$ is the transform of the elastic contribution, $F(1)$ is the single-scattering transform, and I_0 is the zero-loss intensity. So to get the single-scattering transform you take logarithms of both sides, hence the name of the technique.

Extracting the single-scattering spectrum would ideally involve an inverse transformation of $F(1)$, but this results in too much noise in the spectrum. There are various ways around this problem, the simplest of which is to approximate the zero-loss peak to a delta function. After deconvolution, you can subtract the background in the usual way, prior to quantification.

The danger of this approach is that you may introduce artifacts into the single-scattering spectrum. In particular, any gain change in a SEELS spectrum must be removed or not incorporated in the original spectrum at all. Despite the assumptions and approximations, the net result of deconvolution is often an increase in the ionization edge jump ratio. This improvement is important when you are attempting to detect small ionization edges from trace elements, or the presence of edges in spectra from thick specimens. An example of Fourier-Log deconvolution is shown in Figure 39.14.

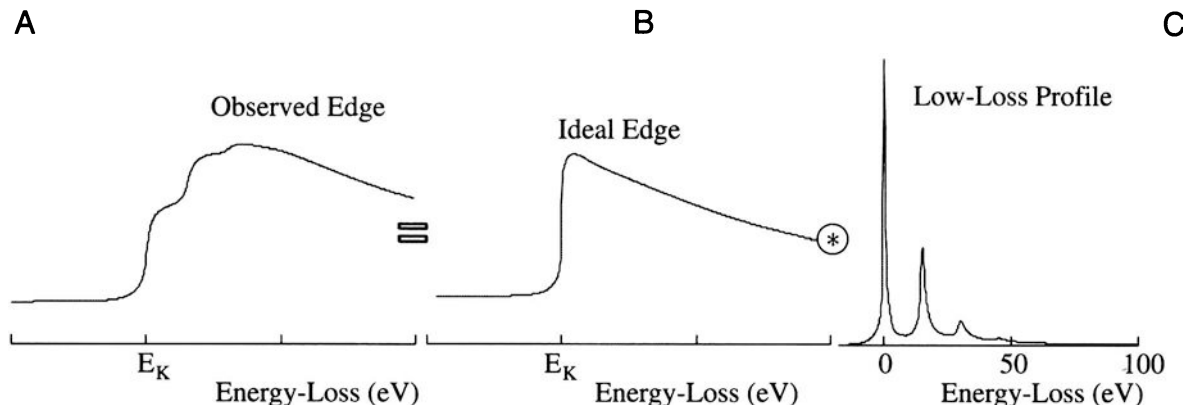


Figure 39.13. The contribution of plural scattering to the experimentally observed ionization edge intensity profile (A) is determined by the convolution of the ideal single-scattering ionization edge (B) with the low-loss plasmon region (C).

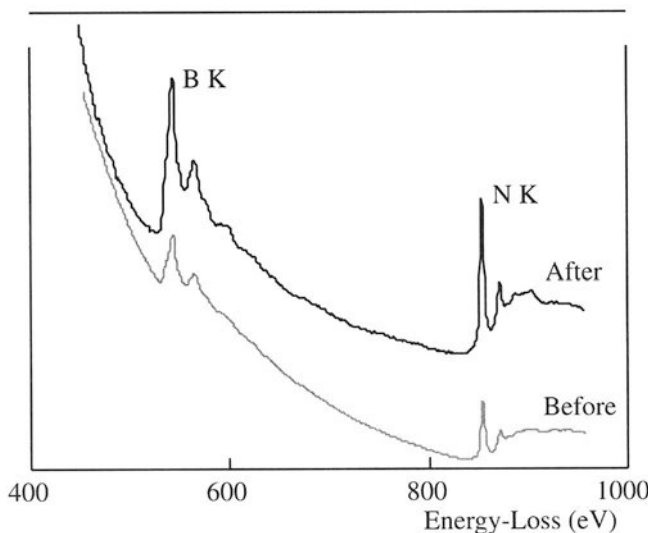


Figure 39.14. A spectrum from a thick crystal of BN before and after Fourier-Log deconvolution. The jump ratio is increased in the deconvoluted spectrum, which is displaced vertically for clarity.

The *Fourier-Ratio* technique approximates the experimental spectrum to the ideal single-scattering spectrum, convoluted with the low-loss spectrum. We define the low-loss portion of the spectrum as the region up to ~ 50 eV, including the zero-loss peak, but before the appearance of any ionization edges. So we can now write

$$F' = F(1) \cdot F(P) \quad [39.18]$$

where F' is the Fourier transform of the experimental intensity distribution around the ionization edge and $F(P)$ is the Fourier transform of the low-loss (mainly plasmon) spectrum. In this equation, therefore, the instrument response is approximated by the low-loss spectrum rather than the zero-loss peak. If we rearrange equation 39.18 to give a ratio (hence the name of the technique)

$$F(1) = \frac{F'}{F(P)} \quad [39.19]$$

we now obtain the single-scattering distribution by carrying out an inverse transformation. In contrast to the Fourier-Log technique, you must subtract the background intensity before you deconvolute. Again, to avoid the problem of increased noise, it is necessary to multiply equation 39.19 by the transform of the zero-loss peak. Figure 39.15 shows a carbon K edge before and after Fourier-Ratio deconvolution.

Multiple Least-Squares Fitting: If your specimen is not uniformly thin, Fourier techniques won't work. Then you should use multiple least-squares (MLS) fitting of convoluted reference spectra (Leapman 1992). A single-

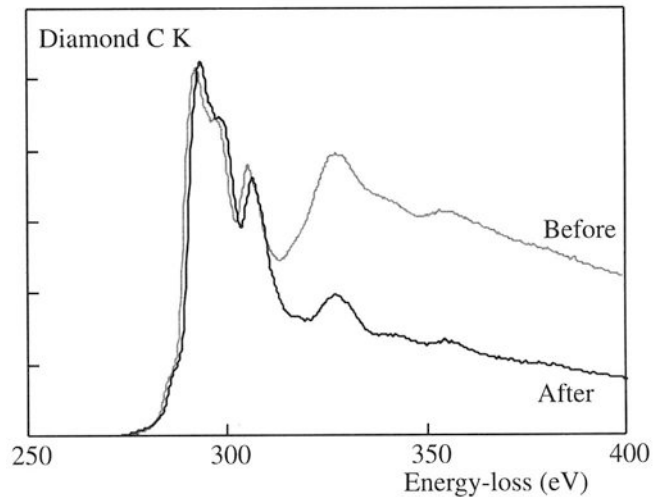


Figure 39.15. A carbon K edge from a thick specimen before and after Fourier ratio deconvolution. The plural scattering plasmon contribution to the post-edge structure is removed.

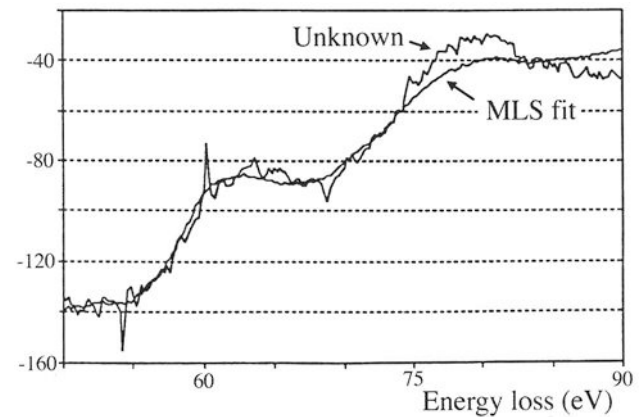
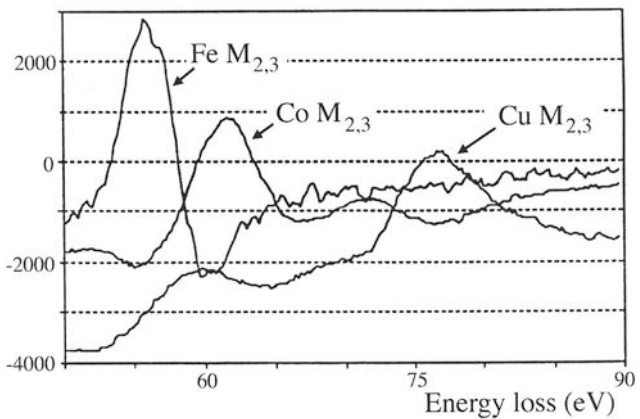


Figure 39.16. (A) Three first-difference M edge reference spectra from Fe, Co, and Cu. (B) MLS fit of the reference spectra superimposed on a low-energy portion of an experimental spectrum from an intermetallic particle in a Cu alloy showing the good fit that can be obtained.

scattering reference spectrum $R_0(E)$ in the region of the edge to be quantified is convoluted with the first plasmon-loss portion of the unknown spectrum (P) and the resultant spectrum $R_1(E) = P * R_0(E)$ is used to generate several reference spectra ($R_2(E) = P * R_1(E)$, etc.). These reference spectra are then fitted to the experimental spectrum using MLS routines and specific fitting parameters are obtained. An experimental set of Fe, Co, and Cu reference spectra is shown in Figure 39.16A and the actual fit to part of the experimental spectrum from an intermetallic in a Cu-Be-Co alloy is shown in Figure 39.16B.

In summary, to quantify ionization-loss spectra you need a single-scattering spectrum, which can be approximated if you have very thin specimens or generated by deconvolution of your experimental spectrum. It is arguable that all spectra should be deconvoluted prior to quantification, but the uncertain effects of the possible errors introduced by deconvolution mean that you should do this cautiously. Often you'll find it useful to deconvolute the point-spread junction from all PEELS spectra, since this sharpens the edge onset and any ELNES intensity variations.

Always check the validity of the deconvolution routine by applying it to spectra from a known specimen obtained over a range of thickness.

39.7. CORRECTION FOR CONVERGENCE OF THE INCIDENT BEAM

If you're working in STEM mode to get high spatial resolution, then it is possible that the beam-convergence angle, 2α , may introduce an error into your quantification. When 2α is equal to or greater than 2β , convergence effects can limit the accuracy because the experimental angular distribution of scattered electrons will be wider than expected. Therefore, you have to convolute the angular distribution of the ionization-loss electrons with the beam-convergence angle. Joy (1986b) proposed handling this through a simple equation which calculates the effective reduction (R) in $\sigma(\beta\Delta)$ when α is greater than β

$$R = \frac{\left[\ln \left(1 + \frac{\alpha^2}{\theta_E^2} \right) \beta^2 \right]}{\left[\ln \left(1 + \frac{\beta^2}{\theta_E^2} \right) \alpha^2 \right]} \quad [39.20]$$

where θ_E is the characteristic scattering angle. So you can see that if α is small (particularly if it is smaller than β), then R is $\ll 1$ and the effect of beam convergence is negligible.

39.8. THE EFFECT OF THE SPECIMEN ORIENTATION

In crystalline specimens, diffraction may influence the intensity of the ionization edge. This effect may be particularly large if your specimen is oriented close to strong two-beam conditions. Both X-ray emission and ionization-loss intensity can change because of electron channeling effects close to the Bragg condition. At the Bragg condition the degree of beam-specimen interaction increases, compared with zone-axis illumination where no strong scatter occurs; the energy-loss processes behave similarly. This phenomenon, known as the Börmann effect in XEDS (see Section 35.8) is not important for low-energy edges, but intensity changes of a factor of two have been reported for Al and Mg K edges (Taftø and Krivanek 1982). The use of large α minimizes the problem in XEDS, but beam-convergence effects are themselves a problem in EELS. The easiest way to avoid orientation effects is simply to operate under kinematical conditions and stay well away from any bend centers or bend contours, just as in XEDS.

39.9. SPATIAL RESOLUTION

In contrast to the situation in XEDS, beam spreading is not a major factor in determining the source of the EELS signal and so the many factors that influence beam spreading are mainly irrelevant. The spectrometer only collects those

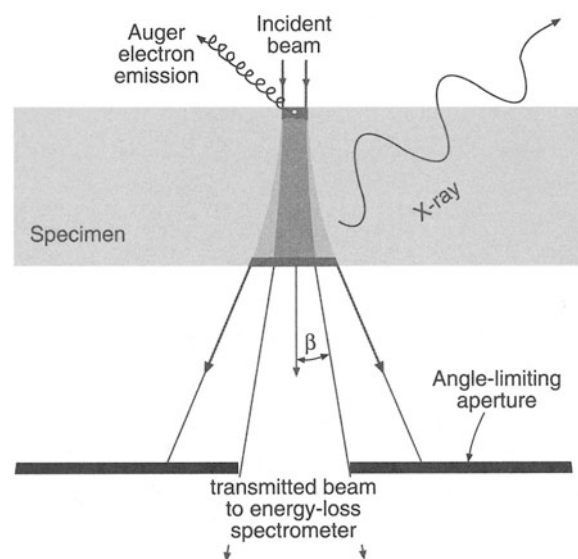


Figure 39.17. The effect of the spectrometer collection angle is to limit the contribution to the spectrum from high-angle scattered electrons, thus ensuring a high spatial resolution signal.

electrons emanating from the specimen in a narrow cone, as shown in Figure 39.17. Therefore, energy-loss electrons that are elastically scattered through large angles are excluded from contributing to your spectrum. Remember that for XEDS these same high-angle electrons would still generate X-rays some distance from the incident probe position, and these X-rays would be detected by XEDS.

In the absence of a contribution from beam spreading, the spatial resolution of ionization-loss spectrometry depends on the mode of analysis:

- The factor controlling the resolution in STEM mode, or in a probe-forming mode on a TEM, is mainly the size of the probe; we can easily get data with probe sizes <10 nm, and <1 nm with more difficulty.
- When we operate in TEM mode, the spatial resolution is a function of the selecting aperture, i.e., the spectrometer entrance aperture and its effective size at the plane of the specimen.

In TEM mode, chromatic aberration usually limits the spatial resolution, as we showed back in Section 37.4.B. We know that the EELS signal isn't affected much by beam spreading and we can easily limit the source of the signal to a few nanometers with an FEG. So, there have been correspondingly fewer studies of the limits of spatial resolution. Most work on defining the spatial resolution has been pursued in France by Colliex and co-workers, e.g., Colliex (1985). Because the primary factor when operating in STEM mode (especially with an FEG) is the incident-probe diameter, we have to be concerned about the problems of spherical aberration broadening the probe (Colliex and Mory 1984). So you must be careful in your selection of the beam-defining aperture. We discussed this topic in detail in the section on the spatial resolution of XEDS.

One factor that we often consider in EELS, but ignore in XEDS (although it occurs in X-ray generation also), is the phenomenon of delocalization.

Delocalization is the ejection of an inner-shell electron by the passage of a high-energy electron some distance from the atom.

If you are physics oriented and want to read more about this, see Muller and Silcox (1995). The scale of this wave-mechanical effect is small, in the range 2–5 nm, and it is inversely proportional to the energy loss. So it appears that, except in rare cases, delocalization will not limit the spatial resolution; the practical factors such as probe aberrations, signal-to-background in the EELS signal, and damage are much more important. So we can conclude that spatial res-

olution for EELS will be somewhat better than for XEDS and experiments seem to indicate that this indeed is the case (Colliex 1985). In fact, in certain zone-axis misorientations, it appears that the (FEG) electron beam, if it is <1 nm, can be localized to individual rows of atoms, producing atomic-level spatial resolution (see Figure 40.5C and Browning *et al.* 1993).

39.10. DETECTABILITY LIMITS

The detectability limits for ionization-loss spectrometry are governed by the same factors as we discussed for XEDS. Therefore, the inverse relationship with spatial resolution also applies. Clearly we have to optimize several factors:

- The edge intensity.
- The signal-to-background ratio (jump ratio).
- The efficiency of signal detection.
- The time of microanalysis.

EELS has an inherently higher efficiency than XEDS, but a correspondingly poorer signal-to-background because of the higher background in the spectrum. Joy (1986a) has attempted to compare the two techniques in some detail and calculations based on a thermionic source. He concluded that the MMF for EELS would be of the order of 1–10% in a Si foil 50 nm thick; this value is somewhat worse than the experimental data for XEDS in similar specimens. Leapman and Hunt (1991) have argued that in most situations, PEELS is more sensitive to the presence of small amounts of material than XEDS.

The time of collection, which strongly influences the detectability limit, is particularly dependent on whether serial or parallel collection is used. Colliex (1985) reckons

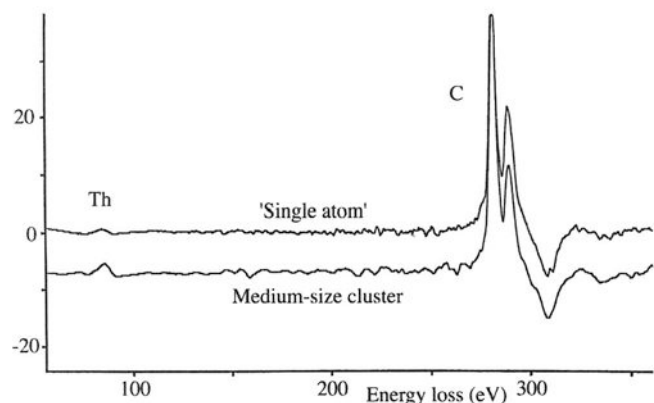


Figure 39.18. First-difference spectra showing the detection of a small cluster and a single atom of Th on a carbon support film.

that a tenfold improvement in all EELS performance criteria is to be expected if parallel collection is used. The best results, combining sensitivity and spatial resolution, will be obtained with an FEG. Krivanek *et al.* (1991) used an FEG DSTEM, parallel detection, and sophisticated data processing to detect the presence of single atoms of Th on thin carbon films, as shown in Figure 39.18. While this is a most favorable analysis situation because of high Z of the atoms and the low average Z of the support film, the result

still shows clearly the superiority of the best possible EELS microanalysis over XEDS, which cannot yet detect single atoms.

In conclusion, microanalysis using ionization edges, while considerably more difficult to perform than XEDS, appears to offer both improved spatial resolution and analytical sensitivity. Parallel collection is significantly better than serial collection in both aspects. As was the case for XEDS, an FEG source is required for the best performance.

CHAPTER SUMMARY

The ionization edges can be used to give quantitative elemental analyses from all the elements in the periodic table using a ratio equation. Beware, however, of the many experimental variables you have to define for your TEM, the PEELS, and the specimen. Compared to XEDS there have been very few quantitative analyses or composition profiles measured using EELS.

To use Egerton's ratio equation:

- You have to subtract the background using a power law or MLS approach. The former is easier.
- Integrate the edge intensity. That's straightforward.
- Then you have to determine the partial ionization cross section $\sigma_K(\beta\Delta)$. This is more difficult.
- Calculate $\sigma_K(\beta\Delta)$ with SIGMAK and SIGMAL for most K and L edges.
- For M edges and for the lightest elements (e.g., Li), use known standards.

The difficulty with using standards is that the specimen thickness has to be the same as the unknown and the standard also has to have the same bonding type as the "unknown." This is often impossible, although specimen thicknesses can be deduced directly from the low-loss spectrum intensity. The biggest limitation to quantification is that, ideally, your specimens have to be less than one mean-free path in thickness (typically < 50 nm) otherwise deconvolution routines are needed, which can introduce artifacts on their own.

Spatial resolution and minimum detectability are better than XEDS. Single-atom detection has been demonstrated.

REFERENCES

General References

- Egerton, R.F. (1996) *Electron Energy-Loss Spectroscopy in the Electron Microscope*, 2nd edition, Plenum Press, New York.
- Joy, D.C. (1986a) in *Principles of Analytical Electron Microscopy* (Eds. D.C. Joy, A.D. Romig Jr., and J.I. Goldstein), p. 249, Plenum Press, New York.
- Joy, D.C. (1986b) in *Principles of Analytical Electron Microscopy* (Eds. D.C. Joy, A.D. Romig Jr., and J.I. Goldstein), p. 277, Plenum Press, New York.
- Maher, D.M. (1979) in *Introduction to Analytical Electron Microscopy* (Eds. J.J. Hren, J.I. Goldstein, and D.C. Joy), p. 259, Plenum Press, New York.
- Williams, D.B. (1987) *Practical Analytical Electron Microscopy in Materials Science*, 2nd edition, Philips Electron Optics Publishing Group, Mahwah, New Jersey.

Specific References

- Ahn, C.C. and Krivanek, O.L. (1983) *EELS Atlas*, Gatan, Inc., 780 Commonwealth Drive, Warrendale, Pennsylvania 15086.
- Browning, N.D., Chisholm, M.F., and Pennycook, S.J. (1993) *Nature* **366**, 143.
- Colliex, C. (1984) *Advances In Optical and Electron Microscopy* **9** (Eds. R. Barer and V.E. Cosslett), p. 65, Academic Press, New York.
- Colliex, C. (1985) *Ultramicroscopy* **18**, 131.
- Colliex, C. and Mory, C. (1984) *Quantitative Electron Microscopy* (Eds. J.N. Chapman and A.J. Craven), p. 149, SUSSP Publications, Edinburgh, Scotland.
- Disko, M.M. (1986) in *Microbeam Analysis-1986* (Eds. A.D. Romig Jr. and W.F. Chambers), p. 429, San Francisco Press, San Francisco, California.
- Egerton, R.F. (1979) *Ultramicroscopy* **4**, 169.

- Egerton, R.F. (1981) in *Proc. 39th EMSA Meeting* (Ed. G.W. Bailey), p. 198, Claitors, Baton Rouge, Louisiana.
- Egerton, R.F. (1989) *Ultramicroscopy* **28**, 215.
- Egerton, R.F. (1993) *Ultramicroscopy* **50**, 13.
- Egerton, R.F., Williams, B. G., and Sparrow, T.G. (1985) *Proc. Roy. Soc. A* **398**, 395.
- Hofer, F., Golob, P., and Brunegger, A. (1988) *Ultramicroscopy* **25**, 181.
- Krivanek, O.L., Mory, C., Tence, M., and Colliex, C. (1991) *Microsc. Microanal. Microstruct.* **2**, 257.
- Leapman, R.D. (1992) in *Transmission Electron Energy Loss Spectrometry in Materials Science* (Eds. M.M. Disko, C.C. Ahn, and B. Fultz), p. 47, TMS, Warrendale, Pennsylvania.
- Leapman, R.D. and Hunt, J.A. (1991) *Microsc. Microanal. Microstruct.* **2**, 231.
- Liu, D.R. and Williams, D.B. (1989) *Proc. Roy. Soc. London A* **425**, 91.
- Malis, T., Rajan, K., and Titchmarsh, J.M. (1987) in *Intermediate Voltage Electron Microscopy* (Ed. K. Rajan), p. 78, Philips Electron Optics Publishing Group, Mahwah, New Jersey
- Malis, T. and Titchmarsh, J.M. (1988) in *Electron Microscopy and Analysis-1985* (Ed. G.J. Tatlock), p. 181, Adam Hilger Ltd., Bristol and Boston, Massachusetts.
- Malis, T., Cheng, S., and Egerton, R.F. (1988) *J. Electron Microsc. Tech.* **8**, 193.
- Muller, D.A. and Silcox, J. (1995) *Ultramicroscopy* **59**, 195.
- Rez, P. (1989) *Ultramicroscopy* **28**, 16.
- Taftø, J. and Krivanek, O.L. (1982) *Phys. Rev. Lett.* **48**, 560.
- Zaluzec, N.J. (1981) in *Analytical Electron Microscopy-1981* (Ed. R.H. Geiss), p. 193, San Francisco Press, San Francisco, California.

Everything Else in the Spectrum

40

40.1. Fine Structure in the Ionization Edges	689
40.1.A. ELNES	689
40.1.B. EXELFS	694
40.2. The Low-Loss Spectrum	696
40.2.A. Plasmon Losses	696
40.2.B. Dielectric-Constant Determination	697
40.2.C. Band-Gap and Interband Transitions	698
40.2.D. Angle-Resolved EELS	698
40.3. Energy-Filtered and Spectrum Imaging	699
40.3.A. STEM Digital Imaging	700
40.3.B. TEM Analog Imaging	700

CHAPTER PREVIEW

The energy resolution of the magnetic prism spectrometer is very good, which means that the energy-loss spectrum contains a wealth of information about the specimen in addition to its basic elemental chemistry. In the previous chapter, we mentioned how we can learn about chemistry using ionization edges. Much of this chemical information is contained in fine-detail intensity variations at the ionization edges in the core-loss spectra termed *energy-loss near-edge structure* (ELNES) and *extended energy-loss fine structure* (EXELFS). From this fine structure, we can obtain information on how the ionized atom is bonded, the coordination of the atom, and its density of states. Furthermore, we can probe the distribution of other atoms around the ionized atom, i.e., the radial distribution function (RDF). Understanding these phenomena requires that we use certain concepts from atomic and quantum physics. The nonphysicist can skip some sections at this time and just concentrate on the results. The rewards of working through this topic will be an appreciation of some of the more powerful aspects of EELS.

If high spatial resolution is important, you can't obtain this additional information by any other spectroscopic technique.

In addition to the extra information around the ionization edges, we can extract useful data from the low-loss region (<50 eV) of the spectrum. The predominant features in this part of the spectrum are the plasmon

peaks, which represent the response of the weakly bound valence and conduction electrons to the high-energy incident electron. The plasmon response contains direct information about the free-electron density. In some binary free-electron alloys, plasmon-peak shifts reflect the composition of the specimen. Within the low-loss region, but separate from the intense plasmon peak, we can find intensity that is related to the dielectric constant of the specimen. Furthermore, we can discern certain inter/intraband transitions, especially in polymers, and we can measure directly the band gap of semiconductors and insulators. We also introduce briefly the effect of the angle of scatter of the energy-loss electrons, which can be studied using the DP.

We note how the intense nature of the EELS spectrum, due mainly to the very high collection efficiency of the spectrometer, permits EELS imaging. Energy-loss (or energy-filtered) images and DPs can be formed in two ways: slowly, quantitatively, and digitally, or rapidly and qualitatively in an analog fashion. The primary advantage of EELS imaging is that *all* the information available in the spectrum can be imaged and related to all the other diffraction and imaging techniques that come from the TEM.

Everything Else in the Spectrum

40

40.1. FINE STRUCTURE IN THE IONIZATION EDGES

We saw in Section 38.4 that the ionization edges have intensity variations both within about 30 eV of the onset of the edge (ELNES) and extending for several hundred eV as the edge intensity diminishes (EXELFS). This fine structure contains a wealth of useful information, but to understand its origins you have to use some ideas from quantum physics.

Both ELNES and EXELFS arise because the ionization process can impart more than the critical ionization energy (E_c) needed by the core electron to escape the attraction of the nucleus.

Any excess energy ($>E_c$) that the core electron possesses can be imagined as a wave emanating from the ionized atom. So again, we have to switch from a particle to a wave model of the electron, as we've done before, e.g., when we talked about diffraction in Part II. If this wave has only a few eV of excess energy, it undergoes plural elastic scattering from the surrounding atoms, as shown schematically in Figure 40.1A; this scattering is responsible for the ELNES, as we'll show. If the wave has even more excess energy, then it is less likely to be scattered several times and we can approximate the cause of the EXELFS to a single-scattering event, as shown in Figure 40.1B. Thus, EXELFS and ELNES can be viewed as a continuum of electron-scattering phenomena, with the arbitrary distinction that ELNES is confined to a few tens of eV past the edge onset. While ELNES arises from a more complex process than EXELFS, it is more widely used, because the ELNES is more intense, and so we'll discuss it first.

40.1.A. ELNES

The Physics: A core electron may receive enough energy from the beam electron to be ejected, but not enough to es-

cape to the vacuum level. So it is still not free of all specific nuclear attraction. In such circumstances, the final state of the core electron will be in one of a range of possible energy levels above the Fermi energy (E_F). You may recall that the Fermi level, or the Fermi surface in three dimensions, is the boundary between the filled states and the unfilled states in the weakly bound conduction/valence bands (although, strictly speaking, this statement is only true when $T = 0$ K). In a metal, there is no separate valence band and E_F sits somewhere in the conduction band, as shown schematically in the classical energy level diagram of an atom in Figure 40.2. In an insulator or a semiconductor, E_F is between the valence band (which has all filled states) and the conduction band (which has no filled states).

The EELS: The excited electron can reside in any of the unfilled states, but not with equal probability. Some empty states are more likely to be filled than others because there are more states within certain energy ranges than in others. This uneven distribution of electron energy levels is termed the density of states (DOS) and this is also shown in the right diagram in Figure 40.2. Because of the greater probability of electrons filling certain unoccupied states above E_F , the intensity in the ionization edge is greater at the corresponding energy losses above the critical ionization energy E_c (which is equivalent to E_F), as shown in Figure 40.3.

This variation in intensity, extending several tens of eV above E_c , is the ELNES and is effectively a probe of the DOS above E_F .

The Application: The importance of ELNES is that the DOS is extremely sensitive to changes in the bonding, or the valence state, of the atom. For example, if you look ahead to Figure 40.5 the carbon K ELNES is different for graphite and diamond and the Cu L ELNES changes when Cu is oxidized to CuO. On an even more detailed level, we can deduce the coordination of the ionized atom from the shape of the ELNES.

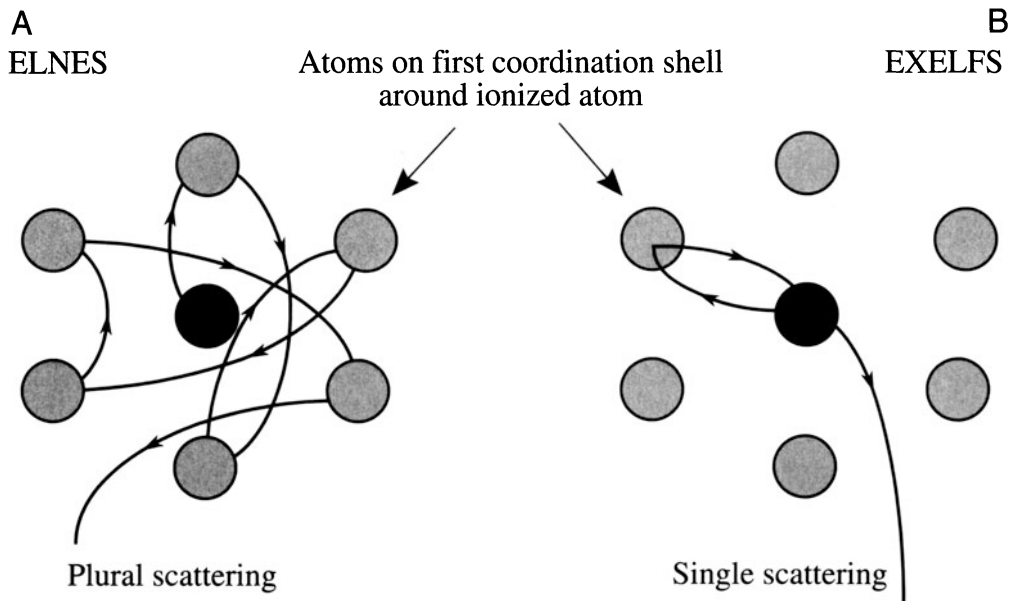


Figure 40.1. Schematic diagram showing the source of (A) ELNES and (B) EXELFS. The excess energy above the ionization threshold creates a wave radiating from the ionized atom which is scattered by surrounding atoms. The low-energy ELNES arises from multiple scatter and is affected by the bonding between the atoms. The higher-energy EXELFS approximates to single scatter and is affected by the local atomic arrangement.

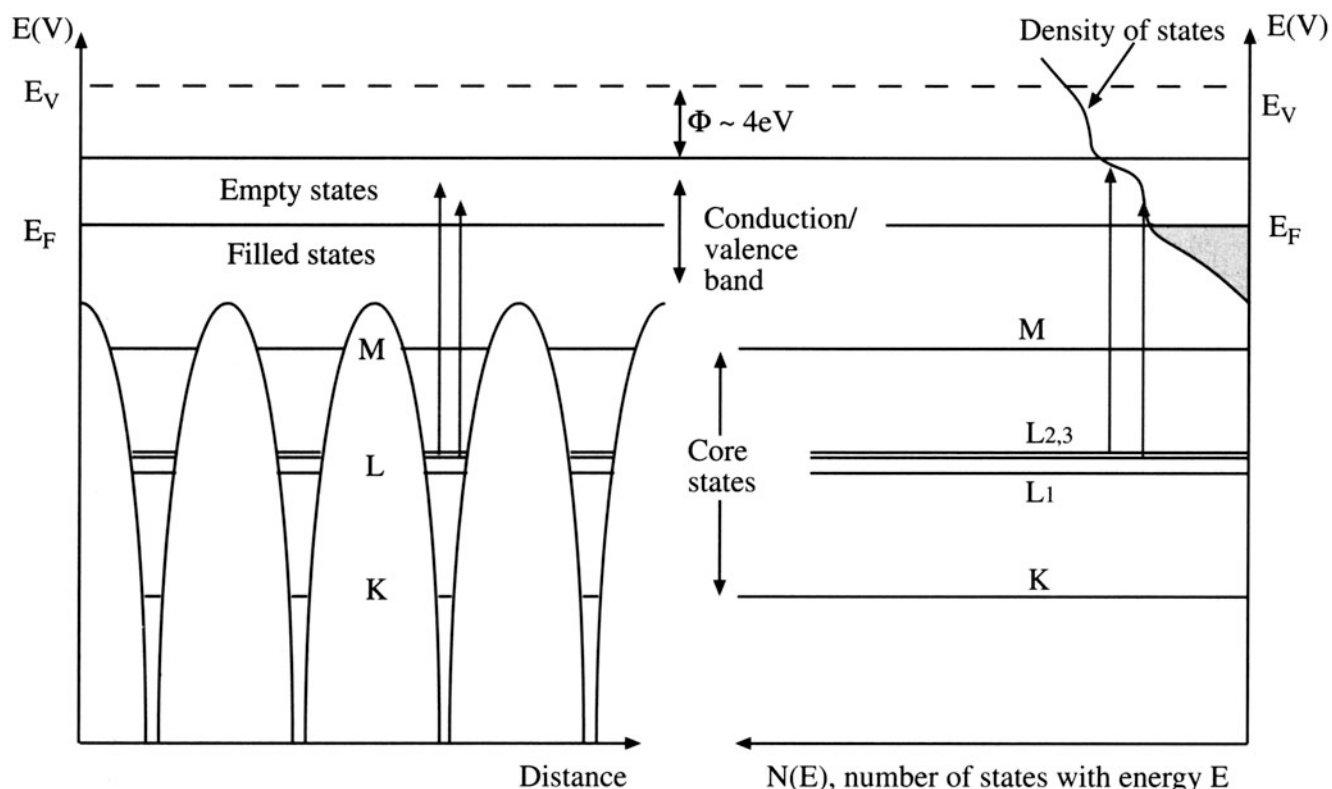


Figure 40.2. Relationship between the classical energy diagram of a metal atom (left) and the density of filled (shaded) and empty (unshaded) states (DOS) in the conduction band (right). The DOS is approximately a quadratic function on which small variations are superimposed. Ionization results in electrons ejected from the core states into empty states above the Fermi level (E_F).

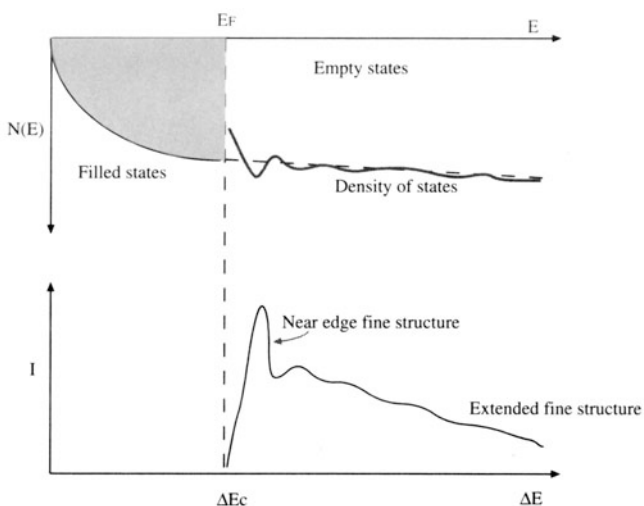


Figure 40.3. Relationship between the empty DOS and the ELNES intensity. Note the equivalence between the Fermi energy E_F and the ionization edge onset E_C . Electrons ejected from the inner shells reside preferentially in regions of the DOS with the greatest density of empty states. The filled states below E_F are shown as a quadratic function, but this is an approximation.

Even if you don't understand the intricacies of the DOS and Fermi surfaces, you can still deduce bonding information simply by comparing your experimental ELNES with that from standard specimens of known valence state or coordination.

The EELS Atlas, which we've already referred to several times, contains many oxide spectra as well as elemental ones.

Perhaps the most startling example of ELNES is the presence of the “white lines,” which we introduced in Section 38.4. They are intense sharp peaks on certain ionization edges; the L edges of the transition metals show such lines. Reminder: white lines were first seen on photographic plates in early X-ray absorption spectroscopy experiments. The white lines in the transition metal L edges are the L_3 and L_2 edges, respectively, as shown in Figure 40.4A. We'll explain what happened to L_1 later. To explain these lines we need a little more quantum physics, which you can skip if you wish and go to the last paragraph of this section. You should also be aware that there is disagreement as to whether white lines are truly “fine structure” or strictly ionization edge (atomic) intensity; but we'll not discuss this somewhat arcane argument.

More Physics: First, go back and look at Figure 38.4 to remind yourself that the various electron energy levels, K, L, M, etc., correspond to principal quantum numbers (n) equal to 1, 2, 3, etc. Within those energy levels, the electrons may have s, p, d, or f states, for which the angular momentum

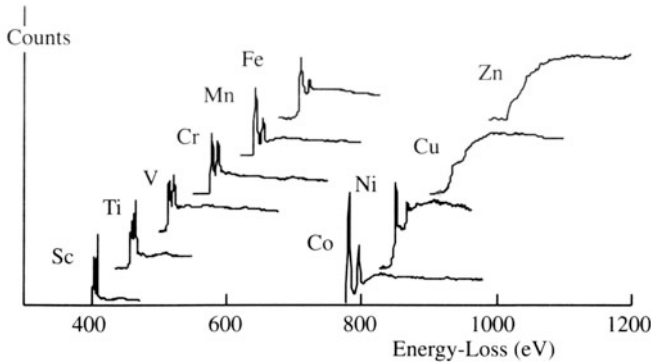


Figure 40.4. The L_3 and L_2 white lines in spectra from the transition metals show a slow variation in intensities until Cu, which has no white lines because the d shell is full.

quantum number (ℓ) equals 0, 1, 2, 3, respectively. The notation s, p, d, f comes from the original description of the atomic spectral lines arising from these electron states, namely, sharp, principal, diffuse, and fine, although these have no counterpart in the EELS spectra we obtain.

As we noted in Section 38.4, the nomenclature $L_{2,3}$ arises from the fact that the L shell, from which the electron was ejected, has different energy levels. Such separation of the energies of the core states is called spin-orbit splitting.

Because the L electrons in levels 2 and 3 are in the p state, quantum theory demands that the sum (j) of their spin quantum number (s) and angular momentum quantum numbers (ℓ) is governed by the Pauli exclusion principle such that j ($= s+\ell$) can only equal $1/2$, $3/2$, $5/2$, etc. The spin quantum number, s (not to be confused with the s state), can only equal $\pm 1/2$. Taking all this into account along with other quantum number restrictions, it turns out that in the higher-energy (more tightly bound) L_2 shell we can have 2 p electrons with $j = \pm 1/2$ while in the L_3 shell we can have 4 p electrons with $j = \pm 1/2$, $\pm 3/2$. Therefore, we might expect twice as many electrons to be excited from the L_3 shell as from the L_2 shell, giving an L_3/L_2 intensity ratio of 2. While this rule is approximately obeyed in the Fe spectrum only, in practice the ratio is seen to increase along the transition metal series from 0.8 for Ti to 3 for Ni, as is also seen in the spectral sequence in Figure 40.4.

Now these p-state electrons in the L shell cannot be excited to just any unoccupied state.

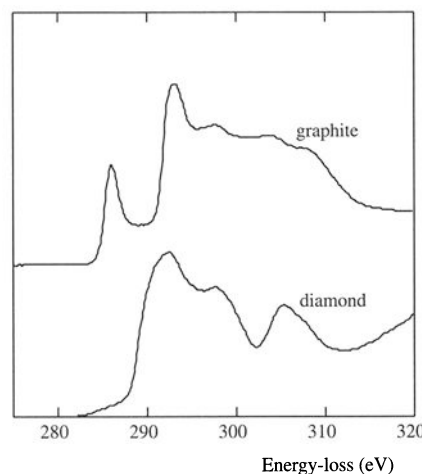
The change $\Delta\ell$ in the angular momentum quantum number between the initial and final states must equal ± 1 . This constraint is called the *dipole selection rule*.

So for the p state ($\ell = 1$) the only permitted final states are either an s state ($\ell = 0$) or a d state ($\ell = 2$). Consequently, the electrons go up primarily into the unoccupied d states, since there are very few unfilled s states in the conduction band.

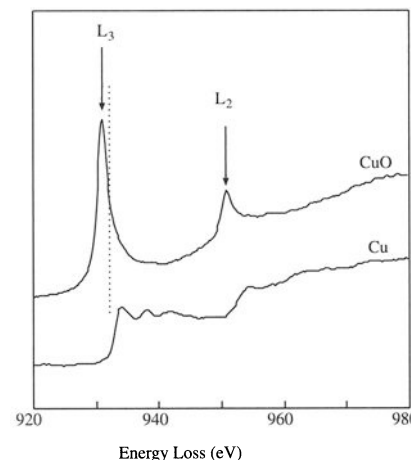
It is because of the dipole selection rules that we don't see a strong L_1 edge in the spectrum. The L_1 edge sits closer to the nucleus than the L_2 and L_3 edges and its electrons are in the s state ($\ell = 0$) so they can only be excited to a p state ($\ell = 1$), but not to a d state ($\ell = 2$), or to another s state. Since there are few unfilled p states in the conduction band of transition metals and they are much more spread out in energy than the d states, the L_1 intensity is very low and the peak is broad and may be invisible in the $L_{2,3}$ post-edge structure.

In fact, the energy width of the white lines is also affected by the time it takes for the ionized state to decay. One form of Heisenberg's uncertainty principle states that $\Delta E \Delta t = h/4\pi$, so a rapid decay gives a wide peak. For example, the Fe L_2 ionization can be rapidly compensated by an electron from the L_3 shell filling the hole and ejecting an Auger electron from the d shell. (This is called a Coster–Kronig transition.) A conduction-band electron could also fill the L_2 core hole, but the L_3 core hole can *only* be filled from the conduction band. Therefore, because there are two possible ways to fill the L_2 core hole, the L_2 line has a shorter Δt and a larger ΔE than the L_3 line, which is much sharper.

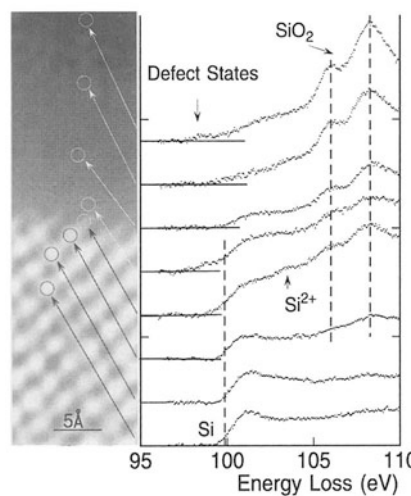
Back to Applications: So let's see how all of this can be useful. If you look at Figure 40.5A you'll see the carbon K edges for graphite and diamond. The carbon atom has hybridized s and p orbitals (termed σ and π in molecular-orbital theory). Graphite contains sp^2 bonds in the basal plane with van der Waals bonding between the planes. The diamond structure, in contrast, has four directional hybridized sp^3 covalent bonds. In diamond, atoms are tetrahedrally coordinated rather than arranged in graphite sheets. The strong peak on the rising portion of the K edge identifies the empty π^* states into which the K-shell electrons are transferred in graphite, while the diamond K edge has no such peak. This kind of information is extremely useful in the study of thin diamond and diamond-like carbon films, which are of tremendous current interest to both semiconductor manufacturers and the coatings industry. Carbon films can be made with a continuous range of graphitic and diamond-like character and it is possible to deduce the relative fraction of sp^3 (diamond) and sp^2 (graphite) bonding from the K-edge ELNES (Bruley *et al.* 1995). Another useful example is given in Figure 40.5B, where the changes in the Cu $L_{2,3}$ edge with oxidation are shown. This is a classical example, since Cu metal has all its 3d states filled so there are no white lines in spectra from the metal. Upon oxidation, some 3d electrons are transferred to the oxygen, leaving unfilled states, and the white lines appear in the oxide spectrum. Note also that the onset of the oxide edge is



A



B



C

Figure 40.5. (A) Differences between the ELNES of the carbon K edge from graphite and diamond, (B) change in the Cu L edge as Cu metal is oxidized, (C) change in ELNES of the Si $L_{2,3}$ edge in a series of spectra gathered from individual atom rows across the interface between crystalline Si and amorphous SiO_2 .

different from that of the metal, because this electron transfer changes the value of E_C .

This phenomenon is called a chemical shift and also helps to fingerprint the specimen.

Finally, in Figure 40.5C the Si L edge ELNES is seen to change across a Si-SiO₂ interface because the Si bonding changes. In this example, you can see the extraordinary power of an FEG STEM to provide simultaneous atomic-level images and spectra localized to individual atomic columns.

The combination of Z-contrast imaging (see Section 22.4) and PEELS is arguably the most powerful analytical technique for atomic characterization (see, e.g., Batson 1995, Browning and Pennycook 1995).

ELNES Calculations: Many attempts have been made to compare the ELNES with calculations of the density of states in simple materials such as metals and oxides. While the experimental and calculated spectra show reasonable agreement in terms of the energy of the various spectral features, there are still some discrepancies in the measured and calculated intensities. Great strides have been made in the last few years, mainly in improvements in models of the atomic potentials and in the computing power needed to pursue the calculations. This aspect is transforming the study of ELNES from an esoteric field to one with broad applications in materials science. There are two approaches to calculating the ELNES:

- Calculate the band structure directly in reciprocal space.
- Calculate the effect of multiple scattering of the electron wave in real space using the model shown in Figure 40.1A.

It can be shown that in fact these two approaches are mathematically equivalent. We'll emphasize the latter method since it is more commonly used.

Various approximations are made in ELNES modeling. The most critical approximation arises from the choice of the atomic potential. A common choice is the so-called "muffin-tin potential" in which a constant potential is assumed in the regions between atoms that don't touch. The potential within the atom must be spherically symmetrical. This model modifies the classical energy diagram, as shown in Figure 40.6. Apparently, this energy profile approximates to a cross section of a tin used by physicists to bake muffins. The potential profile across dissimilar adjacent atoms is asymmetrical, as also shown in Figure 40.6.

Having chosen a potential, the ELNES is determined by calculating all possible inter- and intra-shell scattering events suffered by the electron after it emerges above the Fermi level. A similar calculation is made in X-ray absorption near-edge structure (XANES) studies, and the two phenomena are equivalent. The wavelength is governed by the excess electron energy ($E - E_F$). If the wavelength is long (i.e., low energy), the electron is scattered many times by the first few shells of atoms surrounding the ionized atom. One of the problems that confuses the issue is that the ion-

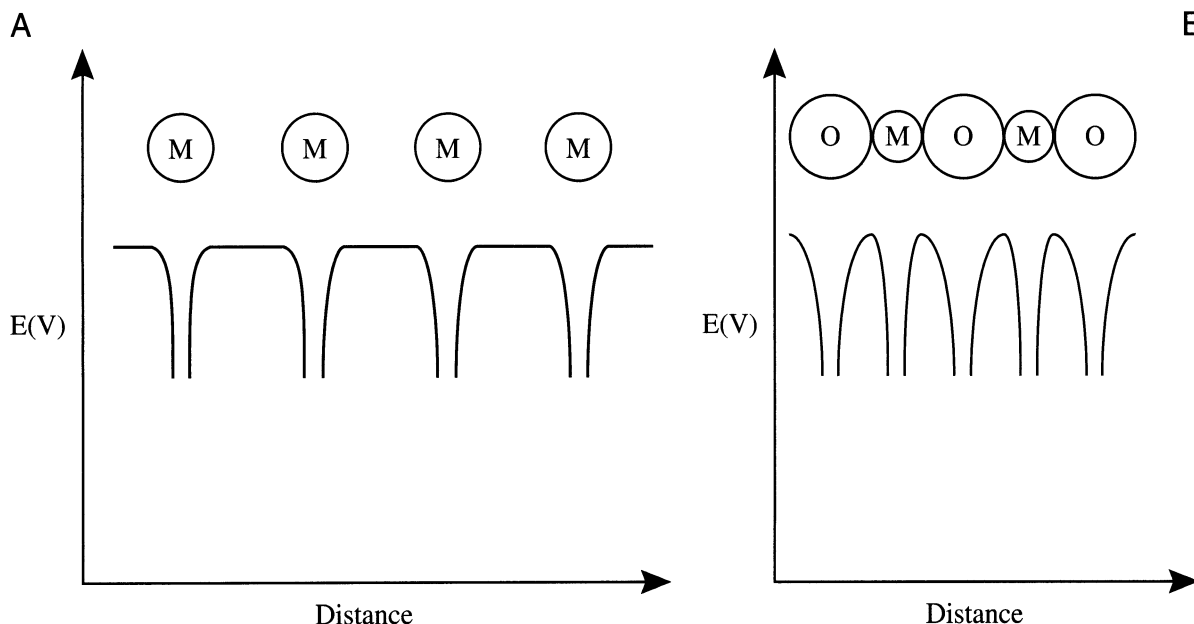


Figure 40.6. The muffin-tin potential energy diagram for (A) a non-closed-packed metal and (B) a metal oxide. Note the symmetry of the potential wells for the metal and the asymmetry for the oxide.

ization event results in a hole in the core shell, thus changing the atomic potential. This is called the *core-hole effect*, and it is accounted for by approximating the ionized atom to one with a nuclear charge of $Z+1$, since the missing electron lowers the shielding effect of the core electrons.

In ceramics and semiconductors the ionized electron remains localized to the ionized atom and may interact with the hole creating an electron–core hole bound state, termed an exciton. Creation of an exciton may influence the ELNES, although this remains a matter of some debate.

It can be shown that the multiple-scattering calculations predict modulations to the intensity of the ionization edge that correspond directly to the DOS of the ionized atom. So you should be aware that these calculations are only an *interpretation* of what actually happens to the electron after it emerges above the Fermi level.

Figure 40.7 shows a comparison of the calculated and theoretical ELNES for the Al L edge in tetrahedral and octahedral coordination in spinels. The difference due to different coordination is obvious. The sharp peak at the Al L-edge onset is thought to be an exciton. This effect is not well modeled by the theory, which otherwise makes a good match with the experimental data. The seminal paper in the field of ELNES experiments on transition metals and oxides is by Leapman *et al.* (1982), and a concise summary was given by Brydson (1991).

40.1.B. EXELFS

If the ejected electron does not fill an empty state, then its excess energy can also be interpreted as an electron wave

which can be diffracted by the surrounding atoms in the structure, giving rise to EXELFS. Because the electron has higher energy than those which gave rise to ELNES, the diffraction is assumed to be single scattering, as shown in Figure 40.1B. As with any diffraction event, there is information about atomic positions in the EXELFS.

So ELNES is multiple scattering and EXELFS is single scattering, although the two phenomena overlap since the L_1 ELNES peak is often far enough past the edge onset to be included in the EXELFS.

The EXELFS modulations are each 20–50 eV wide (just visible in Figure 40.8A), and continue for several hundred eV. EXELFS is exactly analogous to the oscillations seen in the extended X-ray absorption edge fine structure (EXAFS) in synchrotron X-ray spectra. However, EXAFS results from complete photoabsorption of the incident X-ray while EXELFS involves absorption of only a small fraction of the energy of the beam electron.

Experimentally, it's not easy to see the EXELFS modulations because they are only about 5% of the edge intensity, and so you need good counting statistics. With SEELS you may have to gather the spectrum for many minutes or even hours, so PEELS is the only realistic way to pursue EXELFS. A thermionic source is probably best because it can deliver more current than an FEG; for this application, energy resolution is often less important. TEM diffraction mode will also increase your total signal intensity. Either way, you pay a price in terms of a loss of spatial resolution and an increased chance of specimen damage. If you need the best spatial resolution, an FEG and STEM mode is best.

We're interested in EXELFS because of the structural information contained in the intensity oscillations. To extract this information, you can use the Gatan ELP software (see Section 1.5), but you first have to ensure that the spectrum contains single-scattering information only, otherwise the plural-scattering intensity may mask the small EXELFS peaks.

Deconvolution is always the first step if the specimen isn't thin enough, i.e., if the plasmon peak is greater than 10% of the zero-loss peak.

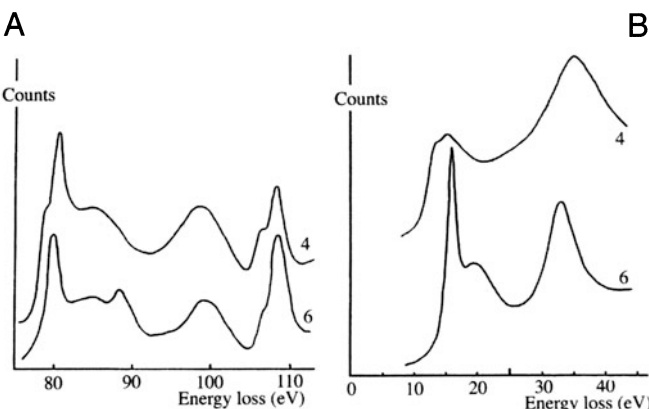


Figure 40.7. Comparison of (A) experimental spectra and (B) theoretical ELNES calculations for the Al L_{2,3} edge in tetrahedrally coordinated (CN-4) and octahedrally coordinated minerals (CN-6). The calculated energy axis in (B) refers to eV above the L edge onset of ~75 eV.

Next, you have to remove the background if it wasn't done prior to deconvolution. Then the EXELFS intensity modulations are fitted to a smooth curve, and the intensity either side of the curve is plotted in \mathbf{k} space (reciprocal space) (Figure 40.8B)

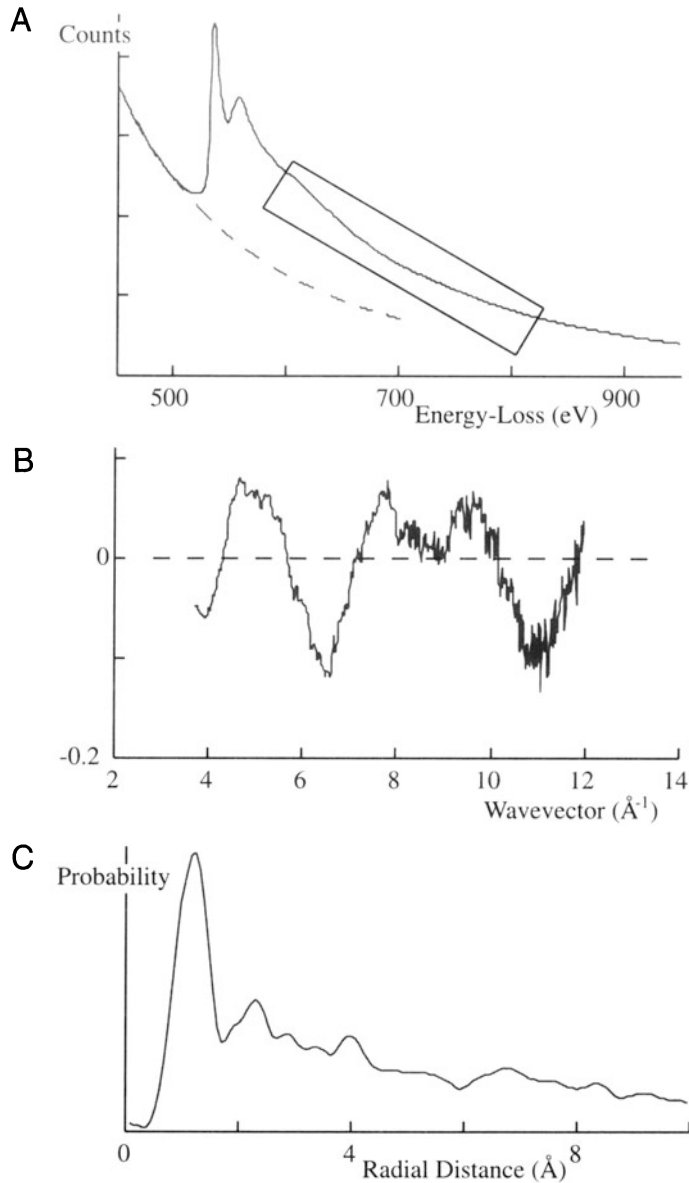


Figure 40.8. (A) EXELFS modulations are barely detectable in the selected post-edge region of an ionization edge. (B) The oscillations either side of a curve fitted to the post-edge spectrum are plotted in \mathbf{k} space before (C) Fourier transforming the data to produce a radial distribution function.

$$k = \frac{2\pi}{\lambda} = \frac{[2m_0(E - E_K)]^{\frac{1}{2}}}{h} \quad [40.1]$$

where E_K is the edge onset energy, E is the energy of the ejected electron, of wavelength λ , and the rest of the terms have their usual meaning. The electron wave interference gives periodic intensity maxima in \mathbf{k} space when

$$\left(\frac{2a}{\lambda}\right)2\pi + \Phi = 2\pi n \quad [40.2]$$

Here a is the distance from the ionized atom to the first scattering atom, and Φ is the phase shift that accompanies the scattering. Therefore, there are periodic maxima occurring for $n = 1, 2, \dots$, and for different interatomic spacings. Consequently, you should be able to determine the local atomic environment, if the various interferences can be discriminated. The atomic spacing is obtained by a Fourier transform of the \mathbf{k} -space modulations to give a radial distribution function, originating at the ionized atom (Figure 40.8C). Peaks in the RDF indicate the probability of an atom occurring a certain distance from the origin.

With EXELFS we can determine the partial RDF around a specific atom, and we are not restricted to the heavier atoms ($Z > 18$) needed for EXAFS. So there is great potential for studying materials such as low- Z glasses, amorphous Si, and quasicrystalline structures. The high spatial resolution is obviously advantageous and all the data can be compared with diffraction patterns and images of the analyzed area. However, like all EELS techniques, we can't get good EXELFS unless the specimen is very thin. Despite these advantages, RDF work continues to be dominated by synchrotron sources because of the intensity of the signal, but EXELFS studies are increasing, e.g., Sklad *et al.* (1992), Qian *et al.* (1995).

RDF data acquired through EXELFS complement another TEM method of acquiring RDF information. This involves energy filtering of SAD patterns by scanning the pattern across the entrance aperture to the PEELS using post-specimen scan coils (Cockayne *et al.* 1991; see also Sections 18.6 and 40.3). Effectively, a full spectrum is available at each scattering angle but, in fact, only the zero-loss (ideally only the elastic) electrons are required. The plot of the zero-loss intensity as a function of scattering angle constitutes a line profile across a filtered diffraction pattern from which the RDF can be extracted; you can see a related example if you look ahead to Figure 40.15. This process does not have the spatial resolution of EXELFS, since typical SAD patterns are integrated over $\sim 0.2\text{--}1 \mu\text{m}^2$, but the signal is much stronger than EXELFS. Accuracies of $\pm 0.001 \text{ nm}$ in nearest-neighbor distances can be obtained, and the process is rapid enough to be performed on-line.

The techniques of ELNES and EXELFS are really quite remarkable demonstrations of quantum theory and the wave-particle duality. Consider that within the spectrum we are only gathering beam electrons that have been scattered by the specimen atoms, yet we are able to deduce information about what happened to those atoms *after* the beam-specimen interaction and where the atoms are in the structure!

An approximate particle-based analogy would be to imagine that we are catching bowling balls that have been thrown at pins, arranged in a certain pattern. (Although instructive, this exercise is best carried out as a thought experiment!) From the velocity of the balls that we catch, we are able not only to identify the weight of the pin that was hit (i.e., identify the characteristic ionization edge), but also to deduce how the pin fell down and where it rolled (the ELNES). Furthermore, we can also work out the spatial arrangement of the surrounding pins that didn't fall down (the EXELFS).

So how does the beam electron know where the core electron went after it left the core shell? The answer lies in the fact that the bowling ball (particle) analogy is totally inadequate. In fact, only certain electron transitions are allowed and the beam electron can therefore only transfer certain quantized energies to the core electron, not a continuum of possible energies. So the beam electron does know the possible final state of the core electron.

40.2. THE LOW-LOSS SPECTRUM

40.2.A. Plasmon Losses

The low-energy plasmon-loss region of the spectrum also contains chemical information, because the composition of the specimen may affect the free-electron density, n , which in turn changes the plasmon-energy peak position, since the two are related, as we described back in equation 38.6. Historically, this technique was the first aspect of EELS to produce quantitative microanalysis data, and it has been used in a limited number of systems, mainly aluminum and magnesium alloys in which the plasmon-loss spectrum is dominant and consists of sharp Gaussian peaks. For a review see Williams and Edington (1976).

The principle of plasmon-loss microanalysis is based on empirical observation of the shift in the plasmon peak position (\mathcal{E}_p) with composition (C), giving an expression of the form

$$\mathcal{E}_p(C) = \mathcal{E}_p(0) \pm C \left(\frac{d\mathcal{E}_p}{dC} \right) \quad [40.3]$$

where $\mathcal{E}_p(0)$ is the plasmon energy loss for the pure component. By creating a series of binary alloys of known composition we can develop a working curve, which we can then use to calibrate measurements of \mathcal{E}_p in unknown alloys. Table 40.1 summarizes the available plasmon-loss data for Al alloys, gathered in this manner.

Table 40.1. Alloys in Which the Variation of Plasmon Energy Loss \mathcal{E}_p Has Been Measured as a Function of Composition

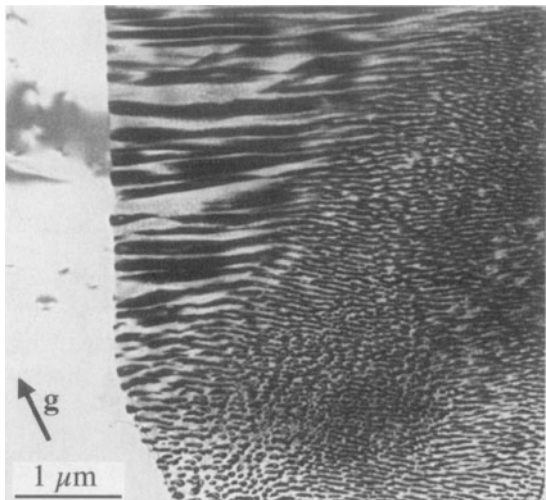
Alloy (at. %)	Range	\mathcal{E}_p (eV) variation with fractional concentration C
Al-Mg	0–100	$\mathcal{E}_p = 15.3 - 5.0 C_{Mg}$
Al-Mg	0–8	$\mathcal{E}_p = 15.3 - 4.4 C_{Mg}$
Mg-Al	0–9	$\mathcal{E}_p = 10.61 + 5.9 C_{Al}$
Al-Cu	0–2	Nonlinear
Al-Cu	0–2	$\mathcal{E}_p = 15.3^a - 10 C_{Cu}$
Al-Cu	0–17.3	$\mathcal{E}_p = 15.3 + 4.0 C_{Cu}$
Al-Zn	0–30	$\mathcal{E}_p = 15.3 - 0.2 C_{Zn}$
Al-Ag	0–6	$\mathcal{E}_p = 15.3^a + 1.6 C_{Ag}$
Al-Li	0–25	$\mathcal{E}_p = 15.3^a - 4.0 C_{Li}$
Al-Ge	0–10	$\mathcal{E}_p = 15.3 + 0.1 C_{Ge}$
Al-Zn-Mg	0–4	$\mathcal{E}_p = 15.3 - 4.7 C_{Mg}$

^aNormalized to 15.3 eV energy loss for pure Al.

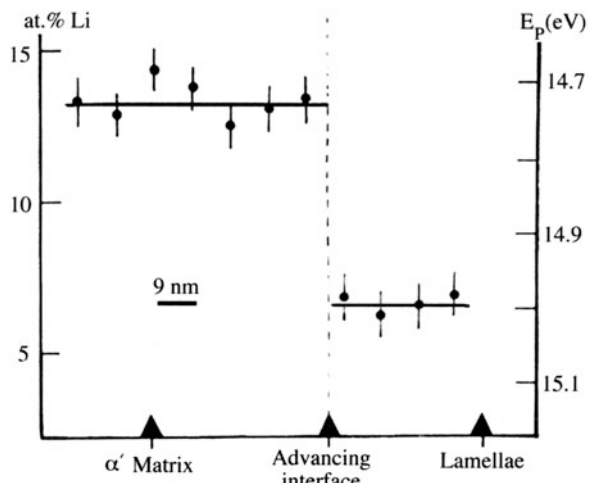
Since plasmon-loss analysis demands the measurement of peak *shifts* rather than peak positions, you need an energy spectrum of the highest resolution and sufficient dispersion to measure the peak centroid accurately. The early plasmon-loss studies did not have access to FEGs and so the resolution of the thermionic source was a limiting factor. The poor resolution was compensated for to some extent by utilizing a high-dispersion Wien Filter or a Möllenstedt electrostatic spectrometer and recording the spectra photographically. More recently, similar results have been achieved using the relatively low-dispersion magnetic-prism spectrometer and electronic recording, but with an FEG. While the shift in the position of the plasmon peak may be as small as ~0.1 eV, the position of the peak centroid can still be measured to an accuracy of ~0.05 eV by computerized peak-fitting (Hunt 1995). Figure 40.9 illustrates some early plasmon-loss concentration data and the visible peak shifts that occur.

Plasmon-loss spectrometry has high spatial resolution and is relatively insensitive to specimen thickness and surface deposits. The spatial resolution is controlled by the localization of the plasmon oscillation, which is only about 10 nm, since the plasmon disturbance is rapidly damped in the free-electron gas. Your specimen thickness only affects the number and intensity of the plasmon peaks, not their position, as we described back in Figure 38.2. In fact, you get the best results from plasmon-loss spectrometry when your specimen is about 1–2 mean free paths (λ_p) thick, so that several intense Gaussian peaks are observable. The plasmon signal is intense and is the dominant loss feature in the spectrum. There are unfortunately strong practical disadvantages, which account for the almost complete absence of plasmon-loss data since the advent of ionization-loss techniques in the mid-1970s.

A



B



C

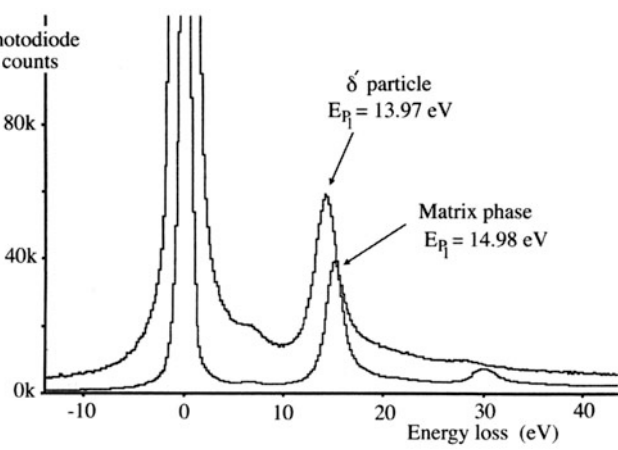


Figure 40.9. (A) Discontinuous transformation interface in Al-11 at.% Li. (B) Plasmon-loss variation and related Li composition change across the interface in (A). (C) Comparison of spectra from the matrix (5 at.% Li) and the precipitate (25 at.% Li) reveals the shift in the plasmon peak.

We are limited to specimens showing well-defined peaks, and only binary specimens can be sensibly analyzed.

In addition, the alloying element must produce a detectable change in \mathcal{E}_p and this is by no means always the case. For example, the addition of 30 at.% Zn to Al scarcely changes \mathcal{E}_p . It is possible that application of modern detection and data-processing techniques may improve the quality and ease of acquiring and analyzing plasmon-loss spectra. However, it is not clear that they will permit the technique to be expanded significantly past the limited range of materials to which it has already been successfully applied.

While quantitative plasmon-loss microanalysis is limited, you can still use the plasmon part of the spectrum to identify unknown phases by the technique of “fingerprinting,” as we showed in Figure 38.3. The low-loss portion of the spectrum is often sufficiently distinctive for different compounds that, since suitable libraries of known spectra exist that we’ve already referenced, you can use these libraries to cross-check the spectra from unknowns. In fact the plasmon-loss spectrum is more robust than the ionization-loss spectrum, since it will not change significantly as you change such experimental variables as α , β , kV, and it is insensitive to the data-processing variables that plague ionization-loss spectra. For example, direct examination of the low-loss spectrum is sufficient to distinguish between free-electron metals and transition metals, as shown in Figures 40.10A,B. Similarly, the low-loss spectra of the different oxides are equally distinctive (Figure 40.10C).

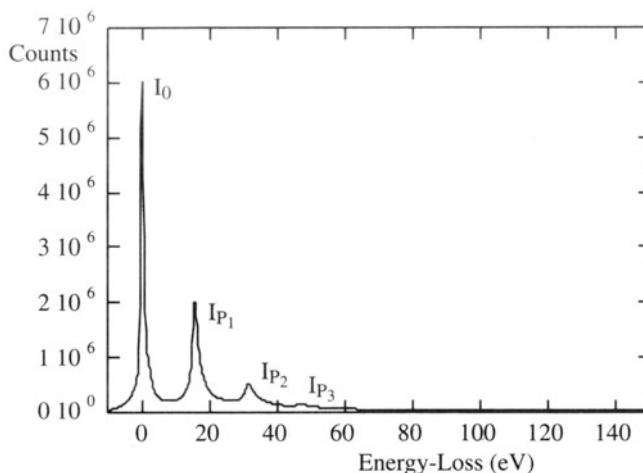
40.2.B. Dielectric-Constant Determination

We can view the energy-loss process as the dielectric response of the specimen to the passage of a fast electron. As a result, your energy-loss spectrum contains information about the dielectric constant or permittivity (ϵ). The single-scattering spectrum intensity $I(\ell)$ is related to ϵ by the expression (Egerton 1996)

$$I(\ell) = I_0 \frac{t}{k} \text{Im} \left(-\frac{1}{\epsilon} \right) \ln \left[1 + \left(\frac{\beta}{\theta_E} \right)^2 \right] \quad [40.4]$$

where I_0 is the intensity in the zero-loss peak, t is the specimen thickness, and k is a constant incorporating the electron momentum and the Bohr radius. You can use a Kramers–Kronig analysis to analyze the energy spectrum in order to extract the real part of the dielectric constant from the imaginary part (Im) in equation 40.4, and details

A



are given in Egerton (1996). Since you need a single-scattering spectrum, deconvolution is again the first step.

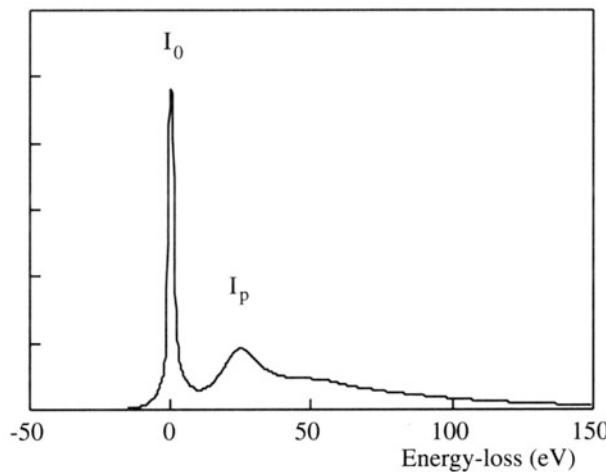
The Kramers–Kronig analysis gives the energy dependence of the dielectric constant and other information which we usually obtain by optical spectroscopy.

The advantage of EELS for this kind of work is the improvement in spatial resolution over electromagnetic radiation techniques. Also, the frequency range which is available is more extended. The low-energy plasmon part of the energy-loss spectrum out to about 20 eV is of most interest to us, and corresponds to optical analysis of the dielectric response from the visible through the ultraviolet frequency range. So in a single EELS experiment you can, in theory, substitute for a whole battery of optical spectroscopy instrumentation. Physicists are most interested in the low-frequency range around 1 eV, since this is less accessible through optical spectroscopy. For this you need an FEG and a high-resolution spectrometer, and you need to deconvolute out the tail of the zero-loss peak so it does not mask the low-energy intensity. An example of the correspondence between EELS and optical dielectric constant spectra is shown in Figure 40.11.

40.2.C. Band-Gap and Interband Transitions

In the region of the spectrum immediately after the zero-loss peak, and before the rise in intensity preceding the plasmon peak, you can see a region of low intensity. If this intensity approaches the dark noise of the detector, then there are no electron–electron energy transfers occurring. This effect implies that there is a forbidden transition region, which is simply the band gap between the valence and conduction bands in semiconductors and insulators. Figure 40.12A illustrates the variable band gap from specimens of Si, SiO_2 , and Si_3N_4 . In this region there are sometimes small peaks that correspond to interband transition which require energy losses of <10 eV, and surface plasmons may occur. An example of an interband transition is given in the spectra from two polymers shown in Figure 40.12B.

B



C

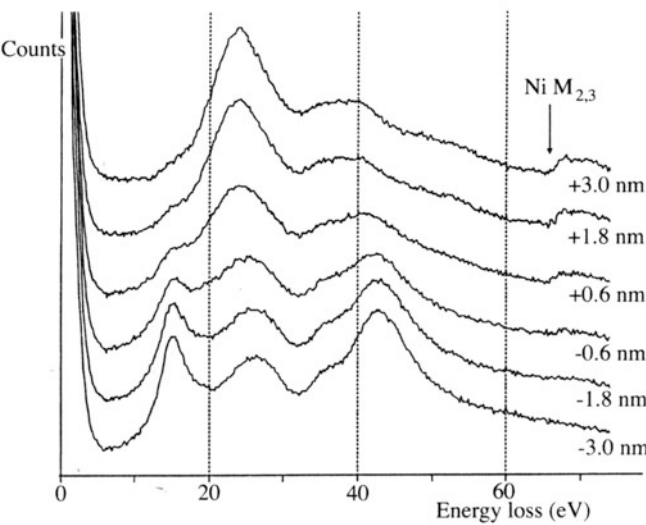


Figure 40.10. (A) Multiple plasmon peaks from Al, which is a free-electron metal, compared with (B) the single weak plasmon from a transition metal, Fe. (C) Six low-loss spectra taken across a NiO (top)– ZrO_2 (bottom) interface showing characteristic differences in the plasmon intensities which occurred within ± 3 nm of the interface.

40.2.D. Angle-Resolved EELS

Most of the time we've been talking about locating the beam at different positions on the specimen and gathering a spectrum by sending the direct beam into the spectrometer. This is often called “spatially resolved” EELS since spectra came from different spatial locations on the speci-

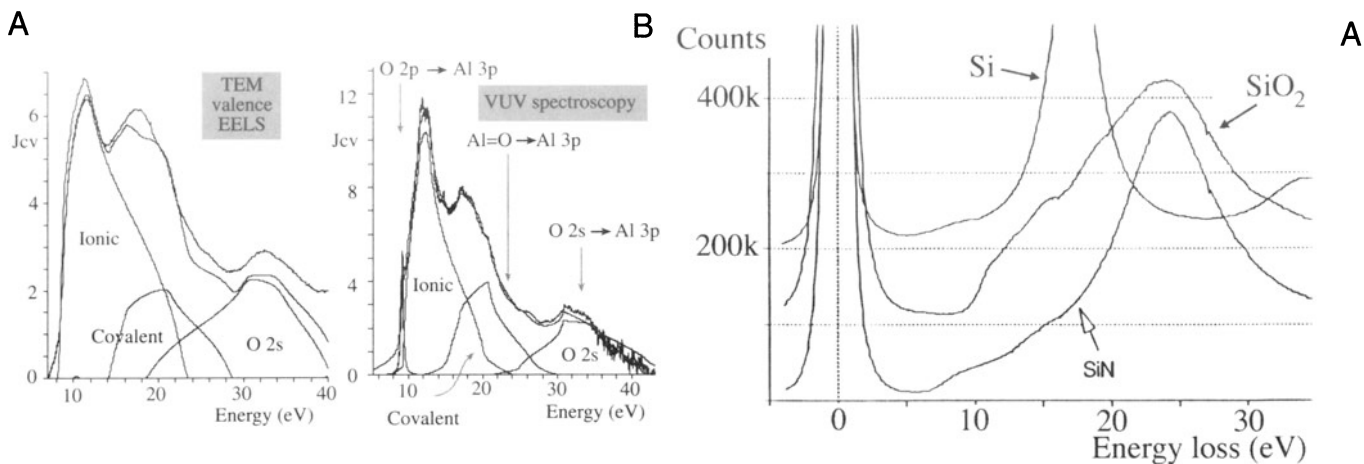


Figure 40.11. Comparison of thin-specimen EELS (A) and bulk-specimen optical dielectric constant data (B) for α -Al₂O₃. J_{cv} is the interband transition strength and the various transitions are labeled: transitions from the filled O 2p level represent ionic bonding, transitions from the hybridized Al=O level represent covalent bonding, interband transitions from O 2s-Al 3p are also detected. Individual contributions to the spectra have been obtained via a critical point model.

men. However, we have occasionally mentioned that the *angle* of scatter of energy-loss electrons is important, and there is a whole field of EELS research that studies angle-resolved spectra. To do this, we just scan the DP across the PEELS entrance aperture (or the SEELS slit) and gather spectra at different angles, as for RDF measurements that we just described. However, rather than studying the energy of electrons primarily, this technique emphasizes the determination of the *momentum* of the energy-loss electrons. Momentum transfer studies were pioneered by Silcox and co-workers (e.g., Leapman and Silcox 1979), and now with FEG STEMs you can get even more information about the symmetry of electronic states which complements spatially resolved ELNES (e.g., Wang *et al.* 1995).

One practical aspect of angle-resolved EELS is the study of Compton scattering, which is the ejection of outer-shell electrons by high-energy photons or electrons. We can detect these Compton-scattered electrons by observing the EELS spectrum at a high scattering angle (about 100 mrad), either by displacing the objective aperture to select an off-axis portion of the diffraction pattern or by tilting the incident beam. This process has been used to analyze the angular and energy distribution of Compton-scattered electrons and determine bonding information, since the Compton-scattering process is influenced by the binding energy (Schattschneider and Exner 1995).

You can appreciate now that there is a wealth of detail in the energy-loss spectrum beyond the basic chemistry of the specimen. To extract this information you need a single-scattering (deconvoluted) spectrum and sophisticated mathematical analysis. Often, our interpretation of the data is limited by lack of knowledge of the physics of

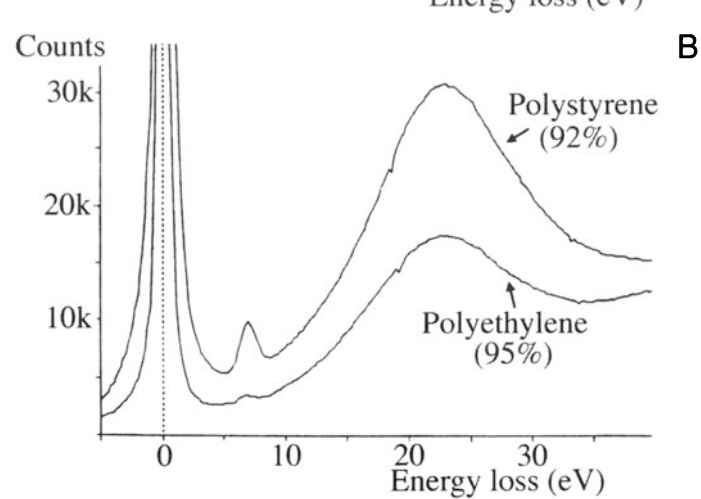


Figure 40.12. (A) Band-gap differences evident in the low-loss spectra of a Si semiconductor and SiO₂ and Si₃N₄ ceramic insulators. (B) The interband transition characteristic of polystyrene, clearly visible on the rise of the plasmon peak, compared with the absence of such a transition in polyethylene.

the electron–specimen interaction. However, considerable research is going on into these aspects of EELS and these fine structure studies are the future of the technique.

40.3. ENERGY-FILTERED AND SPECTRUM IMAGING

We can select the intensity in any part of the EELS spectrum and use it to form an image, either in a digital manner by modulating the signal to the STEM screen or in an analog manner in the energy-selecting TEM. A variety of images can be formed in this way and they have several advantages over conventional TEM and STEM images. We will describe the experimental procedures first and then discuss the different types of images.

40.3.A. STEM Digital Imaging

In SEELS, the ramp voltage to the magnetic prism must be held at a constant setting, so only those electrons in the energy range accepted by the slit pass through the spectrometer. In PEELS you select the output from specific diodes. In either case you've used the spectrometer to select electrons of a fixed energy range. If these electrons are then allowed to hit a detector, the signal can be used to form energy-filtered images. In a TEM/STEM you use the signal from the EELS scintillator to modulate the STEM CRT, while in a dedicated STEM the BF detector sits beyond the EELS and so all your BF images are energy-filtered. To avoid image shifts due to scanning of the beam on the specimen, you must descans the beam using a set of post-specimen coils, which are usually present in the TEM or STEM column as a matter of course. In SEELS, if the spectrometer slit width is too large, your image will suffer from chromatic aberration because electrons of different energy are focused at different planes. In PEELS, the intensity is controlled by the total spectral-acquisition time per pixel. Here, an FEG is best if high-resolution images with reasonable pixel numbers are to be acquired.

With PEELS, it is possible to collect a spectrum in a sufficiently short time (< 50 ms) that you can create images in which a complete spectrum is stored at each pixel and all data processing is carried out after the acquisition.

Then we have what is known as a *spectrum image* (Jeanguillaume and Colliex 1989). Such images contain

immense amounts of data and you need sophisticated hardware and software routines to handle the data. For example, a 512×512 pixel image with a full 1024 channel spectrum at each pixel contains more than 25 Mb of data. Because of the relatively long time to acquire spectrum images, drift correction and other PEELS corrections are necessary (Hunt and Williams 1991). Within such an image you have a *complete* record of the electron–specimen interaction and from such you can create multiple images, as shown in Figure 40.13. This figure is from an Al-Li alloy and shows the distribution of the component elements. There are three strong advantages to this approach:

- You can analyze the “specimen” at a later time, without putting it back in the microscope, and look for elements that were not initially thought to be present or to be important.
- You can process the data in several different ways to compare quantification schemes and the possibility of discerning unexpected correlations between elemental distributions.
- All the information in the EELS spectrum can be mapped discretely, creating, for example, not just elemental images, but dielectric-constant images, valence-state images, thickness images, etc.

40.3.B. TEM Analog Imaging

For analog imaging in a TEM, an Ω filter spectrometer sits between the first and second pairs of projector lenses, as shown back in Figure 37.11 for the LEO EM912. To select

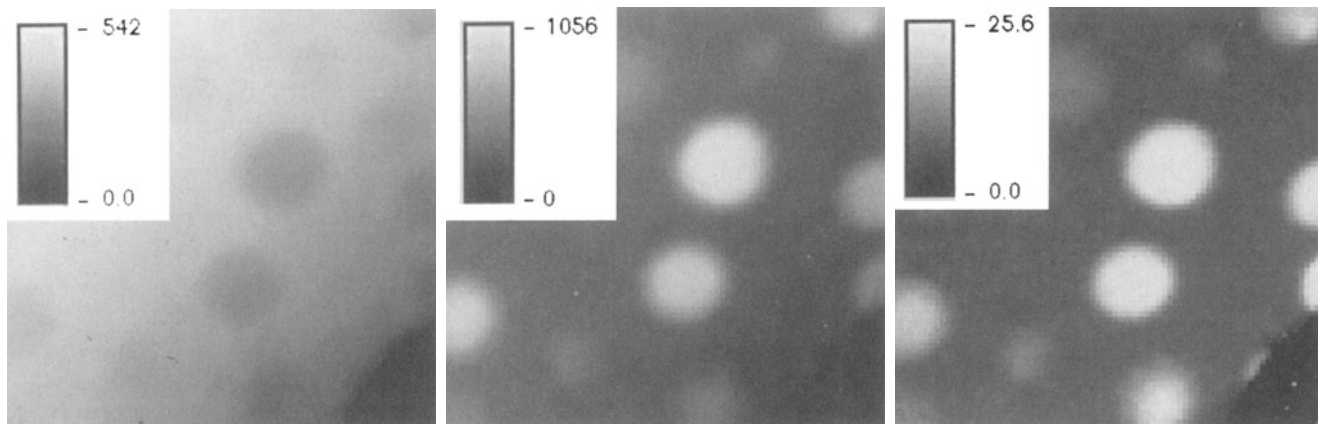


Figure 40.13. Three processed spectrum images of an Al-Li alloy aged to give a dispersion of δ' precipitates. The left image shows the absolute concentration of Al (atoms/nm²) obtained from quantification of the Al L_{2,3} edge, the middle image is the absolute Li content (atoms/nm²) from the Li K edge, and the right image is the Li content (at. %) obtained from the shift of the first plasmon peak. The inserts show the correlation between image intensity and the range of composition imaged.

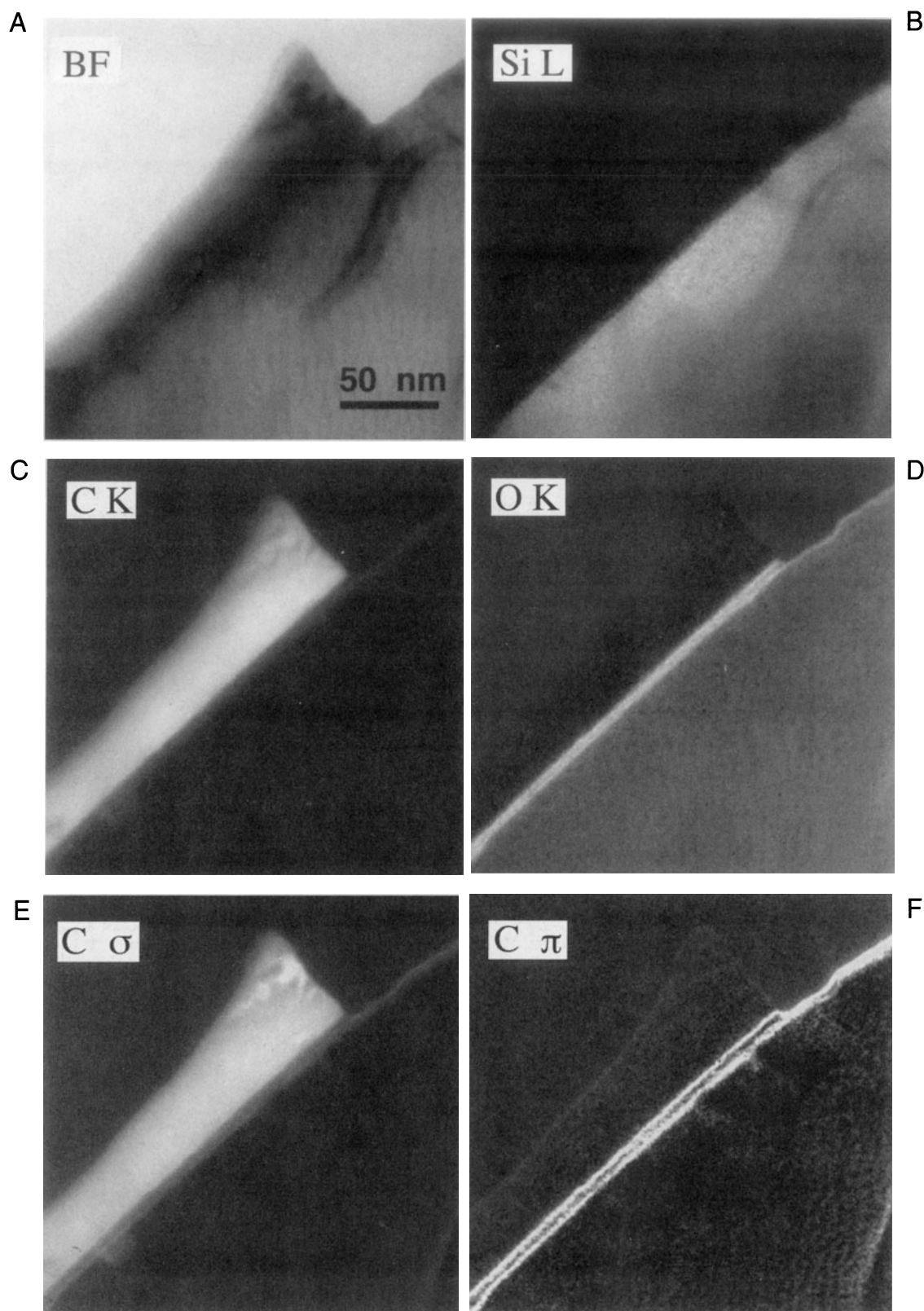


Figure 40.14. (A) TEM BF and (B–F) a series of electron spectroscopic images revealing the Si, C, and O elemental distributions and the carbon bonding maps at the interface between a diamond-like carbon film and a Si substrate. In the oxygen-rich amorphous layer at the interface the carbon atoms exhibit a double layer of π bonds while the carbon film itself is predominantly σ bonded, indicating a high degree of diamond-like character.

the electrons for this imaging (ESI), you shift the spectrum relative to the slit that is positioned after the filter but before the final projector lens. In the LEO instrument, you make the shift by increasing the accelerating voltage of the microscope by $+E$ in order to keep the energy-loss electrons of interest ($-E$) on the optic axis; this shift correction is pre-aligned for the chosen kV. You can filter either an image or DP simply by changing the strength of the intermediate lens preceding the Ω filter. In addition, you can also see the energy-loss spectrum on the TEM screen. This method of spectral display has the advantage that the angular distribution of the energy-loss electrons is spatially resolved, although the absolute intensity has to be determined by digitizing the spectrum or using a microdensitometer. However, this is not the major mode of operation of the instrument, which is optimized for electron spectroscopic imaging (ESI), and many examples are given in a special issue of the *Journal of Microscopy* (Knowles 1994).

For ESI, you adjust the energy window by varying the slit width. With a 20-eV window you can obtain images with a chromatic-aberration limit of ~ 2.5 nm, which compares well with normal TEM C_c -limited resolution. Resolution may be as good as 0.5 nm under ideal conditions. You can select the area to image via a selected-area aperture, or by using Kohler illumination conditions, in which a small parallel beam of electrons is created.

A drawback to this ESI process is that, while background-subtracted core-loss images are easily obtainable, they are not quantitative if significant changes in specimen thickness occur.

However, the images can be acquired in a few seconds, rather than many minutes or hours for a digital image, and a range of filtered images are compared with a conventional TEM BF image in Figure 40.14A–F. ESI is equally applicable to diffraction patterns; energy-filtered CBED is a very powerful technique for extracting more data from conventional CBED patterns, as shown in Figure 40.15. Deininger *et al.* (1994) have demonstrated how energy-filtered CBED patterns can be used to determine structure factors, lattice strains, and the accelerating voltage of the TEM. Removing the inelastic electrons removes much of the diffuse scattering from your diffraction patterns, making comparison of experimental and simulated patterns much easier. In addition to energy-filtered CBED patterns, as shown in Figure 40.15, SAD patterns can be similarly sharpened up, and used for RDF determination, as we already mentioned in Section 40.1.B

In summary, you can perform EELS imaging in two very different ways in a TEM and STEM. You can obtain a variety of images, depending on which portion of your

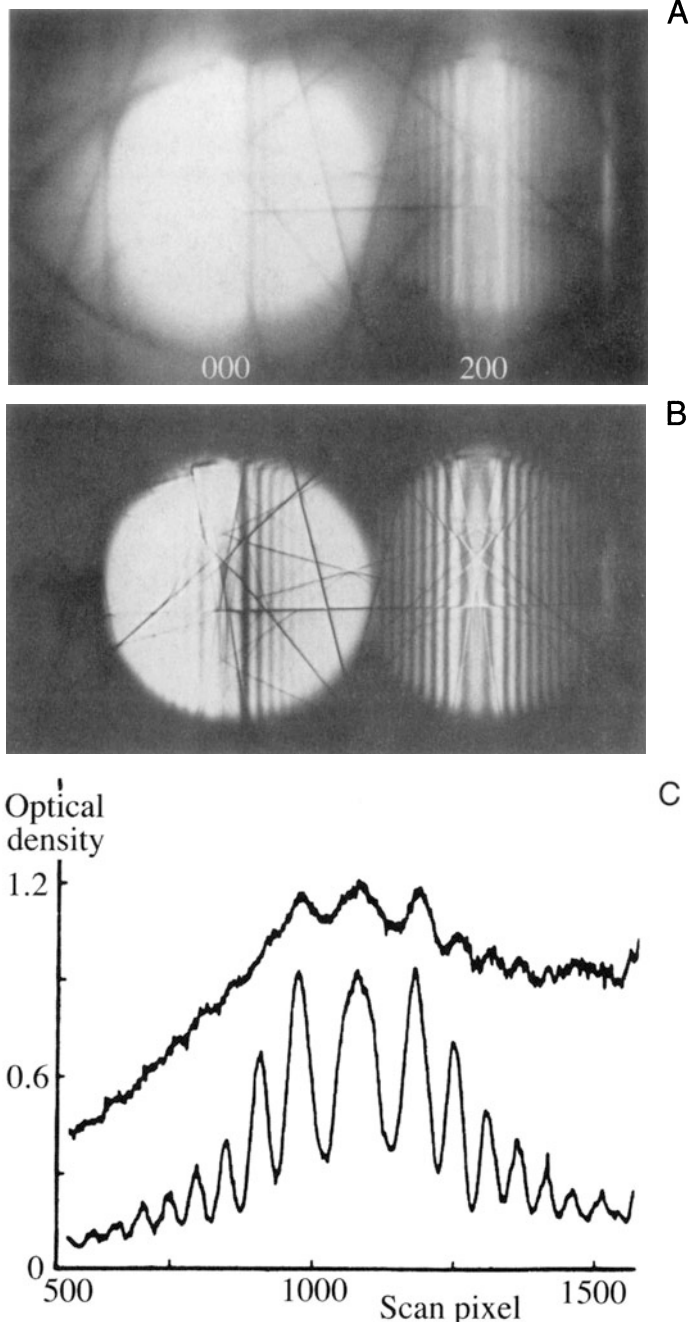


Figure 40.15. (A) Experimental CBED two-beam pattern (000 and 220) from a Si specimen, 270 nm thick. (B) The same pattern energy-filtered using the Zeiss Ω filter with an 8-eV window revealing the K-M fringes useful for thickness determination. (C) Densitometer traces across the 220 diffraction disk, unfiltered (above) and filtered (below).

spectrum is selected and the nature of your specimen. The strong forward-scattered EELS signal, combined with close to 100% detection efficiency, means that EELS imaging is much more statistically viable than thin-film X-ray mapping. This fact, combined with the enormous number

of signals available in the EELS spectrum, make EELS imaging an extremely attractive technique.

Combination of energy filtering with conventional TEM imaging and diffraction will increase as the development of digital TEM technology continues. It is likely that all images will routinely be filtered to remove chromatic aberration effects, which will be a tremendous aid to the materials scientist struggling to make thin specimens from complex multiphase materials. As digital storage becomes cheaper, the ability to save complete spectrum images of all your specimens will become the norm, thus enhancing

the claim that the TEM is *the* most versatile instrument for the characterization of materials.

As a final word, never forget to combine techniques wherever possible to characterize your material. If you are creative, you can even do simultaneous experiments, e.g., by constructing an STM in a TEM (Spence *et al.* 1990). We encourage you to experiment with the microscope at *all* opportunities. Don't think there is nothing new to discover; there is still ample room for you to exercise your imagination and innovation, and the TEM is a fascinating place in which to do just that.

CHAPTER SUMMARY

Both the experimental techniques and the theoretical understanding of EELS are still developing. We have introduced several specialized topics:

- Energy-loss near-edge structure (ELNES).
- Extended energy-loss fine structure (EXELFS).
- Low-loss fine structure.
- Angle-resolved (momentum transfer) EELS.
- Electron spectroscopic imaging (ESI) and spectrum imaging.

However, we have only given you a suspicion of the potential of these topics. If EELS becomes a technique you use in your research, or if you have the time, we recommend watching developments of the technique in the journals referenced at the end of this chapter. EELS, particularly fine structure and imaging, is one of the most dynamic areas of TEM development.

REFERENCES

General References

- Egerton, R.F. (1996) *Electron Energy-Loss Spectroscopy in the Electron Microscope*, 2nd edition. Plenum Press, New York.
 Raether, H. (1965) *Electron Energy-Loss Spectroscopy*. Springer Tracts in Modern Physics. Springer-Verlag, New York.
 Teo, B.K. and Joy, D.C. (1981) *EXAFS Spectroscopy: Techniques and Applications*. Plenum Press, New York.

Specific References

- Batson, P.E. (1995) *Ultramicroscopy* **59**, 63.
 Browning, N.D. and Pennycook, S.J. (1995) *J. Microsc.* **180**, 230.
 Bruley, J., Williams, D.B., Cuomo, J.J., and Pappas, D.P. (1995) *J. Microsc.* **180**, 22.
 Brydson, R. (1991) *EMSA Bulletin* **21**, 57.

- Cockayne, D.J.H., McKenzie, D., and Muller, D. (1991) *Microsc. Microanal. Microstruct.* **2**, 359.
 Deininger, C., Necker, G., and Mayer, J. (1994) *Ultramicroscopy* **54**, 15.
 Hunt, J.A. (1995) in *Microbeam Analysis-1995* (Ed. E.S. Etz), p. 215. VCH Publishers, New York.
 Hunt, J.A. and Williams, D.B. (1991) *Ultramicroscopy* **38**, 47.
 Jeanguillaume, C. and Colliex, C. (1989) *Ultramicroscopy* **28**, 252.
 Knowles, K.M., Ed. (1994) *J. Microsc.* **174**, 131.
 Leapman, R.D. and Silcox, J. (1979) *Phys. Rev. Lett.* **42**, 1362.
 Leapman, R.D., Grunes, L.A., and Fejes, P.L. (1982) *Phys. Rev.* **B26**, 614.
 Qian, M., Sarikaya, M., and Stern, E.A. (1995) *Ultramicroscopy* **59**, 137.
 Schattschneider, P. and Exner, A. (1995) *Ultramicroscopy* **59**, 241.
 Sklad, P., Angelini, P., and Sevely, J. (1992) *Phil Mag.* **A65**, 1445.
 Spence, J.C.H., Lo, W., and Kuwabara, M. (1990) *Ultramicroscopy* **33**, 69.
 Wang, Y.Y., Cheng, S.C., Dravid, V.P., and Zhang, F.C. (1995) *Ultramicroscopy* **59**, 109.
 Williams, D.B. and Edington, J.W. (1976) *J. Microsc.* **108**, 113.

Index

- A₃B ordered fcc, 245
Aberration, 97–98, 137, 352, 544; *see also*
 Chromatic aberration; Spherical
 aberration
aberration-free focus, 468
coma, 469, 473
function, 460
Absorption
 of electrons, 223, 374
 anomalous, 298, 375
 contrast 354
 distance, 397
 parameters, 395
of X-rays, 589
 absorption-free intensity ratio, 615
 correction, 610, 612, 613, 630
 edge, 604, 659
 extrapolation techniques for correction,
 614
 path length, 614
Accelerating voltage
 calibration of, 151
 continuous kV control for CBED, 338
 effect on Bloch waves, 217
 effect on EELS, 669, 702
 effect on Ewald sphere, 199
 effect on X-rays, 578, 583, 589, 609, 624
Adaptive filter, 523–524
Airy disk, 28, 100
ALCHEMI, 616
Allowed reflections, 272
Amorphous
 carbon, 354, 504, 582, 671; *see also* Holey
 carbon film
 germanium, 504, 511
 layer, 522
 materials, 274
 specimen, 353
Amplitude contrast, 349, 351–360, 372; *see
 also* Contrast
Amplitude of diffracted beam, 203, 207, 239,
 254, 405
Amplitude-phase diagrams, 430
Analog
 collection, 644
 to digital converter, 645
 images, 107
 pulse processing, 563
Analytical electron microscopy, 555–703
Angle, 30; *see also* Bragg; Collection
 semiangle; Convergence semiangle;
 Incidence semiangle
Angle-resolved EELS, 698
Angular-momentum quantum number, 691
Annular dark field (ADF), 352, 358, 364; *see
 also* Dark field
 detector
 image, 145
Anodic dissolution, 161
Anomalous
 X-ray generation, 601; *see also* Absorption
Anticontaminator, 121, 124
Antiphase (domain) boundaries, 245, 381, 389,
 478
Aperture, 21, 85–104, 502, 507, 524; *see also*
 Diaphragm
 condenser (C2), 78, 133, 135, 139, 305, 306,
 308, 542, 589, 683
 alignment of C2, 137
 virtual C2, 139
 differential pumping, 123, 641
 function, 460, 463
 objective, 103, 142, 351, 355, 358, 363, 373,
 425, 441, 486, 490, 502–503, 534, 647
 virtual, 466, 579
Artifact
 in EELS, 671
 in image, 10, 11, 494, 504, 512, 534
 of specimen preparation, 163, 170
 X-ray peak, 578, 582, 590, 591
Artificial color, 507
Artificial superlattice, 246
Ashby–Brown contrast, 417
Astigmatism, 98
 condenser, 138
 intermediate, 148
 objective, 147, 188, 463, 469, 473
Atomic
 basis, 242
 number, 39
 correction factor, 610
 scattering amplitude, 43, 240, 243, 276, 538,
 629
 scattering factor, 41, 239, 360
 structure, 441
Auger electron, 52, 658, 692
 spectrometer, 52
Automatic beam alignment, 511
Automatic peak identification, 590
Averaging images, 506
Axis-angle pair, 284, 285
Back focal plane, 90, 140, 186, 188, 307, 641;
 see also Lens
Background, *see also* Bremsstrahlung
 extrapolation, 673
 modeling, 602
 subtraction, 507, 601, 604, 609, 674
Backscattered electron (BSE), 23, 38, 211, 542,
 575, 576
 detection, 113
Baking, 123
Band gap (semiconductor), 195, 219, 229, 233,
 234, 236, 559
 image, 698
Bandwidth, 109, 110
Bar, 119
Barn, 24
Basal plane, 410
Basis vectors, 515–516

Note: all materials examples are indexed under “Materials examples in text.”

- Beam (electron)
 blanking, 567
 broadening, 623, 633
 coherence, 71, 72, 82, 450, 466, 485
 convergence, 139, 304, 360, 364, 490, 647;
see also Convergence semiangle
 current, 73, 78, 615, 669
 damage, 10, 61, 82, 149, 356, 469, 507, 589,
 632
 deflection, 95, 425
 diameter, 79, 82, 307, 623, 669
 diffracted, 203–212; *see also* Diffracted beam
 diffracted amplitude, 207, 239, 254, 405
 direct, 21, 45, 184, 204, 206, 207, 351
 direction, 280, 311, 324
 energy: *see* Accelerating voltage
 incident, 21, 181
 many-beam conditions: *see* Many-beam parallel, 133, 304
 shape, 626
 splitter, 544
 tilting, 135, 268, 505, 511, 518, 534
 translation, 135
 two-beam conditions: *see* Two-beam
- Beam-defining aperture, 112, 683
- Beam-sensitive materials, 507; *see also* Beam damage
- Beam-specimen interaction volume, 623
- Bend contour, 321, 369, 372–373, 376
- Beryllium
 grid, 581, 582
 oxide, 581
 specimen holder, 582
 window, 560, 576, 591, 610
 thickness, 611
- Bethe cross section, 54
- Bethe ridge, 662
- Bi-prism, 544
- Black cross, 338
- Black level, 356
- Black/white contrast, 411
- Bloch theorem, 219, 293
- Bloch wall, 536
- Bloch wave, 203, 209, 215–224, 227–231, 298,
 374, 375, 382, 385, 393, 436, 488, 516
 absorption, 394
 amplitude, 233
 coefficient, 219, 235
 kinematical condition, 616
- Body-centered lattice, 240, 325, 326
- Boersch effect, 645
- Bohr orbit, 658
- Bohr radius, 40
- Borrmann effect, 616, 682
- Boundary: *see* Grain, boundary; Interface;
 Phase, boundary
- Bragg, 45
 angle, 30, 46, 78, 182–185, 204, 315, 361,
 648
 beam, 204, 221, 227, 229, 232, 276, 485,
 486; *see also* Diffracted beam
- Bragg (*cont.*)
 condition, 196, 209, 254, 292, 321, 330, 372,
 376, 397, 403, 424, 428, 682
 diffraction, 184, 204, 291, 361, 655
 law, 46, 150, 181, 182, 193, 195, 239, 297,
 373, 464, 540, 570
 plane, 229
 reflection, 46, 182, 184, 204, 244, 359, 489
- Bravais lattice, 333
- Bremsstrahlung, 52, 56, 558, 575, 578, 581,
 582, 601; *see also* Background
 coherent, 583, 589, 590, 591, 594
- Bright field (BF)
 image 142, 355, 358, 361, 372, 386, 387, 524
 high-order BF, 541
 detector, 145
 in STEM, 144, 355
 symmetry, 329
- Brightness (gun), 70, 78, 472, 541
- Brillouin-zone boundary, 228–235, 262
- Bulk holder, 126; *see also* Specimen holder
- Bulk modulus, 418
- Burgers vector, 259, 381, 403, 405, 407, 409,
 411, 416, 418, 419, 433, 447; *see also*
 Dislocation
- Buxton's tables, 330
- c/a ratio, 241
- Calibration, 138, 148–153
 of accelerating voltage, 151
 of camera length, 150
 of focal increment, 152
 of illumination system, 138
 of image rotation, 151
 of magnification, 148
- Camera constant, 324
- Camera length, 142, 150, 199, 267, 280, 295,
 305, 306, 306, 331, 355, 356, 647, 649
- Carbon, *see also* Holey carbon film
 amorphous, 354, 504, 582, 671
 contamination, 303, 628
 film, 564
 nanotube, 342
- Cartesian-vector notation, 242
- Cathode-ray tube (CRT), 107, 145
- Cathodoluminescence, 59, 107, 113, 127, 543
- Cauliflower structure, 555
- Center of symmetry, 211, 218, 222, 328, 397
- Centrosymmetric point group, 328
- Channel-to-channel gain variation, 664, 676
- Channeling, 223, 616, 682
- Characteristic length, 204, 205, 218; *see also*
 Extinction distance
- Characteristic scattering angle, 655, 662
- Charge-collection microscopy, 59, 543
- Charge-coupled device (CCD), 107, 111
 camera, 189, 356, 396, 437, 472, 502, 508,
 509, 511, 546
- Chemical resolution, 590
- Chemical shift, 693
- Chemical wire/string saw, 159
- Chemically sensitive images, 538
- Chemically sensitive reflections, 243, 244, 244,
 245
- chi-squared, 604, 675
- Chromatic aberration, 98, 101, 138, 356, 471,
 472, 485, 639, 649, 657, 702; *see also*
 Aberration
- Chromium-film standard, 564, 576–579
- Clamping ring, 125
- Cleavage, 159, 168
- Cliff-Lorimer
 equation, 600, 605, 612, 674
 k factor, 600, 605–612, 633
- Coherence: *see* Beam coherence; Spatial coherence
- Coherent
 bremsstrahlung, 583, 589, 590, 591, 594
 Foucault imaging, 536
 Fresnel imaging, 536
 interference, 28
 particles, 417
 processing, 545
 scattering, 22
- Coincident-site lattice, 475
- Cold FEG, 473, 645
- Cold trap: *see* Anticontaminator
- Collection semiangle, 30, 101, 364, 655, 669,
 674, 675
- Collimator, 577
- Column approximation, 203, 210, 382, 385,
 395, 397, 398, 405, 419
- Coma-free alignment, 469
- Comis, 15, 418
- Composition
 measurement, 338, 626
 profile, 617
- Compton scattering, 699
- Computer simulation, 17, 418; *see also* Image, simulation of
- Condenser 1 lens, 78, 133–135, 144
- Condenser 2 lens, 133–135, 137; *see also* Lens aberration, 138, 580
 alignment, 136
 aperture, 137
 calibration, 138
 defocusing, 594
 diaphragm, 579
- Conduction band, 664
- Confidence limit, 607
- Conjugate plane, 89, 141
- Constructive interference: *see* Interference
- Contamination, 96, 114, 123, 303, 469, 540,
 582, 629, 632
- Continuum, 601; *see also* Background; Bremsstrahlung
- Contrast, 351, 406; *see also* Amplitude contrast; Diffraction, contrast; Phase, contrast
 Fresnel, 450–456
 inside-outside, 411, 434
 minimum, 467
 minimum defocus, 469, 473
 transfer function, 460, 462, 463

- Contrast (*cont.*)
 topographic, 540
 Convergence semiangle, 30, 78, 135, 305, 309, 314, 473, 669
 correction, 682
 Convergent beam, 78, 133, 142
 diffraction, 186, 267, 284, 303–342, 510; *see also* Higher-order Laue zone (HOLZ)
 energy-filtered, 702
 imaging, 340
 Cooling holder, 127; *see also* Specimen, holder
 Core-hole effect, 684
 Core-loss image, 702
 Coster-Kronig transition, 56, 692
 Coulomb force, 37
 Count rate, 563, 566, 567, 589, 593
 Coupled harmonic oscillator, 212
 Coupled pendulum, 436
 Critical energy: *see* Ionization
 Cross-correlating image, 512
 Cross-correlation function, 518, 519
 Cross section, 24, 655
 differential, 25, 239
 elastic, 39, 353
 experimental, 678
 generalized, 395, 418
 modified Bethe–Heitler, 603
 partial ionization, 674, 676
 phonon, 61
 plasmon differential, 60
 relativistic Hartree–Fock, 496
 Rutherford, 39, 357
 screened-relativistic Rutherford, 40
 Cross-section specimen preparation, 165
 Cross-tie wall, 536
 Cryogenic pump, 121
 Cryo-transfer holder, 127; *see also* Specimen, holder
 Crystal; *see also* Lattice
 A-face centered, 326
 B-face centered, 326
 I-centered, 326
 cubic, 270
 diamond cubic, 416
 imperfect, 486
 low-index
 high-symmetry pole, 316
 plane, 284
 pole, 295
 zone axis, 197, 514
 low-symmetry zone axis, 311
 noncentrosymmetric, 218, 397
 orientation of, 295
 orthorhombic, 195
 perfect, 217
 potential of, 217
 primitive, 239, 240, 325
 projected potential of, 490
 simple cubic, 240, 243, 244, 255
 tetragonal distortion of, 446
 Crystal Kit, 248
 Crystallographic convention, 212
 Crystallographic shear, 478
 Curie temperature, 391, 536
 Current, 468; *see also* Beam (electron), current centering, 147
 dark, 109, 665
 density, 71
 Curve fitting, 674
 Cut-off angle, 656
 Cyanide solution, 157
 Cyclotron radius, 94
 Dark field (DF), *see also* Weak-beam dark field
 external control for, 534
 image, 142, 143, 352, 355, 361, 369, 371, 372, 386, 387
 annular, 145
 centered, 143, 361–363, 533
 diffuse, 277
 displaced-aperture, 143, 386
 focus of, 467
 high-angle annular, 359
 multiple, 188, 307, 340
 STEM, 145, 356
 through focus (2D), 532
 tilt control, 363
 Dead layer, 109, 560
 Dead time, 563, 566, 590
 Debye–Waller factor, 485, 397
 Decision limit, 633
 Deconvolution, 626, 646, 669, 680, 694
 Defect, 235, 493; *see also* Dislocation; Grain, boundary; Stacking fault; Twin boundary
 computer modeling of 394
 core, 427
 unit cell, 491
 Defocus condition, 533
 Defocus image, 508
 Deformable-ion approximation, 409
 Delocalization, 683
 Delta (δ) fringe, 389
 Delta function, 680
 Density, 624
 Density of states, 664, 689, 694
 Depth
 distribution of X-ray production, 613, 625
 of field, 8, 102, 533
 of focus, 8, 102
 fringes, 431
 Desk-Top Spectrum Analyzer, 15, 570
 Desktop Microscopist, 15, 248, 270
 Detectability limits, 594, 633
 Detection quantum efficiency, 107, 643
 Detector (electron), 21, 107–115, 441; *see also*
 Spectrometer (EELS)
 depletion region of, 108
 envelope function, 472
 gain of, 109, 110, 356
 STEM, 113, 352
 Detector (X-ray): *see* Spectrometer (X-ray energy-dispersive); Spectrometer (X-ray wavelength-dispersive)
 Determination limit, 633
 Deviation parameter, 197, 279, 361, 375, 397; *see also* Excitation error
 Diamond-cubic structure, 416
 Diamond window, 561
 Diaphragm, 95; *see also* Aperture
 self-cleaning, 96
 top-hat C2, 579, 580
 Dielectric constant
 determination of, 691
 image, 700
 Dielectric response, 698
 Difference spectrum, 675
 Differential hysteresis imaging, 15, 356
 Differential pumping aperture, 123, 641
 Differentiating the image, 507
 Diffracted beam, 45, 181, 184, 201–213, 221
 amplitude of, 207–209, 239, 254, 405
 intensity of, 197, 203
 Diffracting plane, 181, 272; *see also* Bragg, plane
 Diffraction, 5, 9, 37, 140, 177–342, 237–249, 251–263
 camera, 179
 center, 147
 contrast, 5, 349, 361–437
 convergent beam: *see* Convergent-beam diffraction
 from dislocations, 259
 double, 278, 285, 335
 extra reflection, 246, 494
 Fraunhofer, 27
 Fresnel, 27
 grating, 148, 149, 254
 group, 330–333
 indexing, 185, 195, 267–287
 oblique-textured, 274
 ring, 273
 mode, 646
 multiple, 203
 nanodiffraction, 342
 pattern, 30, 89, 177–189
 180° inversion of, 151
 selected area: *see* Selected area diffraction (SAD)
 split spot in, 231
 spot spacing in, 258
 streak in, 235, 258
 systematic absence in, 273, 285
 systematic row in, 184, 335, 423
 rocking-beam, 341, 343
 rotation, 268, 363
 scanning-beam, 340
 single-crystal, 271
 vector (g), 182, 184, 194, 208, 272, 425, 430, 437
 Diffraction coupling, 646
 Diffractogram, 504–505, 511
 Diffuse scattering, 258–260, 291, 538; *see also* Scattering
 Diffusion pump, 120
 Diffusion coefficient, 618

- Digital
 filtering, 603
 image, 107, 501
 pulse processing, 563, 565, 567
 recording, 396
- Digital Micrograph, 15, 504, 521
- Dimpling, 160
- Diode array, 645, 650
 saturation of, 671
- Dipole selection rule, 692
- Direct beam: *see* Beam, direct
- Discommensurate structure, 259
- Discommensuration wall, 478
- Disk of least confusion, 79, 97, 101
- Dislocation, 256, 259, 403–419, 447; *see also*
 Burgers vector; Strain
 array, 414
 contrast from, 405
 core of, 260, 406, 409, 428, 454
 density, 403
 dipole, 409, 410, 434
 dissociated, 411, 432, 434, 435
 edge, 405, 406
 end-on, 453
 faulted dipole, 434
 faulted loop, 410
 inclined, 419
 interfacial, 414
 intersecting, 419
 line direction, 403, 405, 419
 loop, 409–411
 misfit, 414
 network, 409
 node, 409, 434
 ordered array of, 260
 pair, 411
 partial, 407, 411, 413, 432, 433
 screw, 405
 strain field of, 412
 superlattice, 407
 transformation, 414
- Disordered/ordered region, 245
- Dispersion
 diagram, 228
 plane (of spectrometer), 640, 642
 relation, 220
 surface 225–236, 261, 262, 375, 391, 437
 branches of 229, 232, 393
- Displacement
 damage, 63
 energy, 63
 field, 396, 403, 405, 408, 409, 418
 vector, 312, 419
- Display resolution, 563, 590, 643
- Double-period image, 515
- Double-tilt holder, 126, 304, 361; *see also*
 Specimen, holder
- Drift
 correction, 508, 628
 rate, 423, 472, 473
 tube, 642, 664
- Dwell time, 115, 642, 670
- Dynamic experiments, 546
- Dynamical diffraction, 185, 203–212, 256, 278;
see also Diffraction
 absence, 335, 336
 calculation of intensity, 256
 condition, 601
 contrast in CBED, 308
 coupling, 221, 185, 206
 scattering, 240
- Edge: *see* Ionization
- EELS: *see* Electron energy-loss spectrometry
 (EELS)
- Effective EELS aperture diameter, 648
- Elastic, *see also* Scattering
 constant, 418
 mean-free path, 612
 scattering, 23, 37–47, 655
 coherent, 184, 361
 cross section, 353
- Elasticity theory, 383
- ELD software, 15, 510
- Electric-field potential, 217
- Electro-discharge machining, 159
- Electron
 backscatter pattern (EBSP), 267, 297
 beam: *see* Beam (electron)
 beam-induced current (EBIC), 59, 543
 channeling, 223, 616, 682
 charge, 217
 crystallography, 303, 508
 detector: *see* Detector (electron)
 diffraction: *see* Diffraction
 dose, 62; *see also* Beam damage
 energy-loss spectrometry (EELS), 7, 291,
 639–703; *see also* Spectrometer
 (EELS)
 angle-resolved, 698
 collection efficiency of, 662
 collection mode, 646
 detectability limit of, 683
 diffraction mode, 646
 image mode, 646
 imaging, 437, 650, 639, 699–703
 microanalysis by, 669–683
 parallel collection, 644
 serial collection, 642
 spatial resolution of, 682
- energy-loss spectrum 655–664
 artifacts in, 664
 atlas of, 658
 channeling effect in, 682
 deconvolution of, 680
 extended fine structure in, 694
 extrapolation window in, 675
 families of edges in, 671
 fine structure in, 660, 663, 689
 near-edge structure in, 659, 689
 parameterization of, 610
 power-law fit, 675
- gun, 72, 472; *see also* Gun
 holography, 543
- Electron (*cont.*)
 interferometer, 451
 lens: *see* Lens
 microscope microanalyzer, 570, 599
 momentum, 220
 phase: *see* Phase,
 potential energy, 217
 rest mass, 13, 656
 scattering: *see* Diffraction; Scattering
 shell, 53
 source, 67–83; *see also* Gun
 structure factor, 397; *see also* Structure factor
 velocity of, 220
 wave vector, 204, 220
 wavelength of, 13, 205, 629
- Electron–electron interaction, 655
- Electron-hole pair, 59, 559, 564
- Electron-spectroscopic imaging, 650, 700–703
- Electropolishing, 161
- Electrostatic lens, 76; *see also* Lens
- ELP (energy-loss program), 15, 671
- EMS (electron microscope simulation
 program), 15, 248, 270, 522
- Empty state, 689
- Enantiomorphism, 340
- Energy, *see also* Electron, energy-loss
 spectrometry (EELS)
 resolution
 X-ray, 559, 562–564, 590, 591, 593, 594
 EELS, 670
 spread, 71, 82
 window, 674
- Energy-dispersive spectrometry, 558–634; *see
 also* Spectrometer (X-ray energy-
 dispersive)
- Energy-loss: *see* Electron, energy-loss
 spectrometry (EELS)
- Envelope function, 460, 466, 471
- Epitaxy, 278
- Errors in quantification, 606
- Escape peak, 568, 591
- Eucentric, 268, 531; *see also* Goniometer
 height, 139, 149, 534
 plane, 95, 305, 306, 307, 309, 577
 specimen, 577
- Ewald Sphere, 196–200, 223, 230–235, 255–
 262, 273, 279, 291, 309, 311, 372, 391,
 408, 425–429, 489, 510
- Excitation error, 197–198; *see also* Deviation
 parameter
 effective, 210, 369, 423
- Exciton, 63, 694
- Extended energy-loss fine structure (EXELFS):
 694
- Extended X-ray absorption fine structure
 (EXAFS), 694
- Exposure time, 423, 425
- Extinction distance, 204–205, 212, 233, 235,
 245, 262, 321–322, 374–375, 397, 411,
 416, 437, 452
- apparent, 397
- determination of, 423

- Extinction distance (*cont.*)
 effective, 233, 430, 629
- Extraction replica, 168, 357
- Extraction voltage, 76
- Extrinsic stacking fault, 387, 432
- Face-centered cubic, 240, 241, 325; *see also* Crystal; Lattice
- Fano factor, 564
- Faraday cup, 112, 567, 629, 645
- Fast Fourier transform (FFT), 487
- Fe^{55} source, 564
- Fermi
 energy, 689
 level, 664, 689
 surface, 259, 689
- Field-effect transistor, 558, 563
- Field emission, 70, 76–77, 134, 544, 589, 626, 670; *see also* Gun
- Filter mask, 523
- Fine structure: *see*, Electron energy-loss spectrometry (EELS)
- Fingerprinting, 658
- Fiori definition, 584, 632; *see also* Peak-to-background ratio
- First-difference spectrum, 675
- First-order Laue zone, 309; *see also* Higher-order Laue zone (HOLZ)
- Fitting parameter, 675
- Fixed-pattern readout noise, 665
- Flat-field correction, 521
- Fluorescence (light), 108
- Fluorescence (X-ray), 52, 628
 correction, 610, 615–616
 yield, 56, 560, 609, 659
- Flux lines, 536; *see also* Magnetic, flux lines
- Focus, 148; *see also* Lens; Overfocus;
 Underfocus
- Focusing circle (WDS), 570
- Forbidden electron energies, 229
- Forbidden reflection, 240, 247, 272, 342; *see also* Diffraction, pattern; Systematic absence
- Foucault image, 535
- Fourier
 analysis, 523
 coefficient, 228
 component, 397
 deconvolution (logarithmic, ratio), 680, 681
 fast (Fourier) transform (FFT), 487
 filtering, 502, 523
 inverse transform, 487
 reconstruction, 502
 series, 218, 220
 transform, 460, 487, 502, 503, 523–524
- Frame averaging, 423, 437
- Frame grabber, 502
- Frame time, 111
- Free electron, 657
- Free-electron density, 657, 696
- Fresnel
 biprism, 450
- Fresnel (*cont.*)
 contrast, 450, 451, 492
 diffraction, 27, 211, 486
 fringe, 82, 148, 492, 493
 image, 536
 zone construction, 211
- Friedel's law, 328
- Full Width at Half Maximum (FWHM), 79, 564, 602
- Full Width at Tenth Maximum (FWTM), 80, 565, 602, 623
- FWTM/FWHM ratio, 565
- G vector, 272; *see also* Diffraction, vector (g)
- g**b**** analysis, 416, 420
- g**r**** contrast, 388, 405
- Gas bubble, 451
- Gas-flow proportional counter, 570
- Gatan image filter (GIF), 639, 650, 664
- Gaussian
 curve fitting, 604
 diameter, 79
 image, 98
 image plane, 89
 intensity, 623, 625
 statistics, 606, 633
- Generalized-oscillator strength, 677
- Generated X-ray emission, 609
- Germanium detector, 559, 562, 590; *see also* Spectrometer (X-ray energy-dispersive)
- Ghost edge, 665, 671
- Gjønnes-Moodie (GM) line, 335, 338
- Glaser, 470
- Glass layer, 260, 453
- Glide plane (dislocation), 403, 406
- Glide plane (symmetry), 333, 335
- Goniometer, 124; *see also* Eucentric
- GP zone, 258
- Grain
 boundary, 197, 261, 277, 381, 414, 453, 491, 493, 494, 522, 523, 618; *see also* Stacking fault; Twin Boundary
 coincident-site lattice, 381
 high-angle, 381, 453
 low-angle, 381
 rotation, 391
 sigma ($\Sigma = 3$), 381
 small-angle, 415
 tilt, 453, 477
 twist, 445
 size, 267
 texture, 267
- Gray level, 507
- Gray scale, 521
- Great circle, 269; *see also* Stereographic projection
- Grid, 158, 166, 582
- Grigson scanning, 342
- Gun, 72–77; *see also* Electron source; Field emission
 alignment of, 137
 brightness of, 70, 78, 472, 541, 589
- Gun (*cont.*)
 crossover, 71
 emission current, 75, 78
 field-emission, 70, 76
 filament, 69
 flashing of, 76
 lanthanum hexaboride, 69
 saturation of, 73
 self-biasing, 73
 tungsten, 69
 undersaturated image of, 75, 468
 Wehnelt cylinder, 72, 73
- Hartree–Slater model, 496, 677
- Heisenberg's uncertainty principle, 692
- Hexagonal close-packed crystal, 241, 247; *see also* Crystal
- High-resolution TEM, 7, 457–482
- High voltage, 72, 471
- High-voltage electron microscope, 7, 128, 546
- Higher-order Laue zone (HOLZ); *see also* Convergent beam
 diffraction, 306, 309, 311, 323, 338
 Kikuchi line, 329
 indexing, 317
 line, 152, 198, 268, 297, 315, 329, 490
 plane, 309, 315
 ring, 311, 323, 338
 scattering, 309
 shift vector \mathbf{t} , 325
 simulation of, 338
- Higher-order reflection, 184, 272
- Higher-order waves, 45
- Higher-order X-ray lines, 571
- History of the TEM, 5
- Holder: *see* Specimen holder
- Hole-count, 579
- Holey carbon film, 81, 82, 148, 166
- Hollow-cone illumination, 361
- Holography, 543
- Howie detector, 359
- Howie–Whelan equations, 206, 207, 369, 374, 382, 383, 395, 396, 398, 403, 418
- Hydrocarbon contamination, 560, 565; *see also* Contamination
- Hydrogenic edge, 659, 662, 673, 677, 680
- Ice, 565
- Illumination system, 133–138, 578; *see also* Condenser 1 lens; Condenser 2 lens; Lens
- Image, 349–549
 analysis of, 15
 calculation of, 493
 contrast in, 351–364
 coupling, 646
 of defects, 381–419, 491
 delocalization in, 472
 distance, 90; *see also* Lens
 drift, 504
 of flux lines, 545
 formation, 88
 lattice-fringe, 441–443

- Image (*cont.*)
 matching, 398
 plane, 89; *see also* Lens
 processing of, 15, 437, 501–507
 rotation of, 95, 151, 363
 simulation of, 15, 375, 413, 418, 437, 483–498, 521
 of sublattice, 475
- Imaging system of TEM, 140–148
- In-hole spectrum, 580
- In-line holography, 544
- In situ* TEM, 128, 502, 546
- Incidence semiangle, 30; *see also* Angle
- Incoherent; *see* Scattering, incoherent
- Incommensurate structure, 478
- Incomplete charge collection, 564, 565, 604
- Incomplete read-out, 665
- Inelastic: *see* Scattering, inelastic
- Information limit, 467, 470
- Information theory, 470
- Inner potential, 218, 219, 221, 452, 454
 mean, 496
 scaled mean, 220
- Inner-shell ionization: *see* Ionization
- Instrument-response function, 680
- Instrument spectrum, 582
- Integration approach, 254
- Intensity, 351; *see also* Spectrum, electron energy-loss; Spectrum, X-ray
 integration, 603–604, 672, 676
 total, 631, 679
 window, 676
- Interaction constant, 461
- Interband scattering, 235
- Interband transition, 655, 656, 658, 698
- Interface, 381, 413, 476; *see also* Grain, boundary; Phase, boundary
 dislocation, 414
 interphase, 407, 626
 semicoherent, 416
 strain at, 447
- Interference, 44, 240
 constructive, 42, 45, 182
 destructive, 45, 182, 184
 fringe, 451
- Intergranular film, 453, 493
- Intermediate voltage electron microscope, 7, 71, 128, 559, 562, 578, 590
- Internal-fluorescence peak, 569, 582, 594
- International Tables, 247, 248, 335
- Internet, 13
- Intersecting-chord construction, 424
- Interstitial atom, 258
- Intershell scattering, 693
- Intraband transition, 655, 656, 658
- Intrashell scattering, 693
- Intrinsic Ge detector, 559, 562, 590; *see also* Spectrometer (X-ray energy-dispersive)
- Inversion-domain boundary, 382, 478
- Invisibility criterion, 21, 406, 410
- Ion beam blocker, 164
- Ion milling, 162–164
- Ion pump, 121
- Ionic crystal, 239
- Ionization, 52–55, 655, 658–663
 critical energy for, 53, 659, 671, 689
 cross section for, 53, 609, 659
 edge, 642, 659, 664, 670, 671
 integration of, 675, 676
 intensity of, 659, 672
 jump-ratio of, 671, 680
 onset of, 674, 676
 shape of, 672
- JCPDS files, 285
- $k (k_{AB})$ factor, 600, 605–611
 calculation of, 607–611
 error in, 607
 experimental values of, 607
- k space, 486, 694, 695
- K vector, 181, 193, 230, 291
- Kernel, 507
- Kikuchi diffraction, 291–298
 band, 291, 293, 296, 298, 306, 531
 line, 267, 268, 280, 291, 314, 315, 374, 376, 423, 425, 639
 3g, 424
 deficient, 292
 excess, 292, 315
 pair, 152
 map, 268, 293, 295
 pattern, 284, 291, 295, 298, 423
- Kinematical diffraction, 308, 541, 601
 approximation, 262, 422, 423
 crystallography, 510
 equation, 423
 integral, 428
 intensity, 276
- Kinematically forbidden reflection, 240, 247, 274, 335; *see also* Forbidden reflection; Systematic absence
- Kinetic energy, 217, 220
- Knock-on damage, 61, 589, 606; *see also* Beam (electron), damage
- Kohler illumination, 702
- Kossel, 329
 cone, 291, 292
 pattern, 306, 324
- Kossel-Möllenstedt (K-M)
 conditions, 307, 309, 323
 fringe, 305, 321, 330
 pattern, 305, 329
- Kramers' cross section, 56
- Kramers' Law, 602
- Kramers–Kronig analysis, 697
- Kurdjumov–Sachs, 285
- L_{12} structure, 389
- Laplacian filtering, 507
- Lattice; *see also* Crystal
 centering, 311, 325
 defect, 452; *see also* Dislocation
 fringe, 441, 442, 468
- Lattice (*cont.*)
 imaging, 441–443
 misfit, 415
 parameter, 205, 245, 258, 271, 286, 338, 381, 416, 491
 point, 239, 241
 strain, 403–419, 702
 vector, 193, 195, 217, 383
- von Laue, 45
 condition, 181, 196
 equations, 45, 182, 195
 groups, 328
 X-ray pattern, 199
 zone, 419, 583; *see also* Higher-order Laue zone (HOLZ); Zero-order Laue zone
- Leak detection, 123
- Least-squares refinement, 518
- Lens, 87–104, 640
 aberration of, 683; *see also* Chromatic aberration; Spherical aberration
 astigmatism, 98; *see also* Astigmatism
 asymmetric, 641
 auto-focusing, 140
 auxiliary, 135, 136
 bore of, 91
 condenser: *see* Condenser 1 lens; Condenser 2 lens
 condenser-objective, 135, 343
 current, 92
 defects, 97
 demagnification, 90
 focal length of, 90
 focal plane of, 89, 90
 focus of, 89, 188; *see also* Overfocus; Underfocus
 gap, 91, 576
 hysteresis, 149
 immersion, 92
 intermediate, 536, 650
 low-field, 536
 mini-lens, 343
 Newton's equation, 90
 objective: *see* Objective lens
 octupole, 93
 optic axis of, 88
 pincushion distortion, 99
 polepiece of, 91
 post-spectrometer, 645
 projector, 641
 projector crossover, 646, 647, 649
 ray diagram, 88
 rotation center of, 147
 sextupole, 642
 snorkel, 92
 superconducting, 93
 symmetric plane of, 140
 thin, 88
 wobbling of, 137, 147
- Library standard, 604, 658
- Light element, 570, 589, 664
- Line of no contrast, 417–418
- Linear elasticity, 403

- Liquid N₂
dewar, 565
holder, 309, 558, 559
- Lithography, 169
- Long-period superlattice, 246
- Long-range ordering, 245, 260, 475
- Lorentz
force, 93
microscopy, 451, 535–537
- Low-dose microscopy, 356, 507
- Low-loss, *see also* Electron energy-loss spectrometry (EELS); Plasmon fingerprinting, 697
intensity, 674
spectrum, 644, 656, 670, 696
- Magnetic
correction, 534
domain wall, 451
flux lines, 546
induction, 536
prism spectrometer, 639, 640
recording media, 534
specimen, 534
- Magnification, 90, 148
- Many-beam
calculation, 398, 485
conditions, 222, 227, 235
images, 429, 432, 442
- Mask, 502
- Mass-absorption coefficient, 610–614; *see also* Absorption of X-rays
- Mass-thickness contrast, 349, 353–358; *see also* Contrast
- Materials examples in text
- Ag, 386, 579
 - Ag₂Al, 295
 - Ag₂Se, 274
 - Al, 32, 42, 52, 322, 341, 373, 412, 449, 557, 657, 658, 698
 - Al-Ag, 8
 - AlAs, 518
 - Al-Cu, 365
 - Al_xGa_{1-x}As, 245, 246, 376, 377, 518, 538, 616
 - Al₃Li, 244, 363, 675, 697, 700
 - Al-Li-Cu, 9, 480
 - Al-Mn-Pd, 480, 494–496
 - AlN, 382, 658
 - Al₂O₃, 247, 260, 278, 371, 374, 538, 658, 699
 - Al-Zn, 618
 - Au, 26, 32, 40, 41, 386, 414, 452, 475, 511, 543
 - Au₄Mn, 475
 - B, 62, 582
 - BaTiO₃, 571
 - Be, 561
 - Bi-Sr-Ca-Cu-O, 478
 - biotite, 8, 604
 - BN, 662, 681
 - carbon, 32, 41, 81, 276, 505, 557, 681; *see also* Amorphous; Holey carbon film
- Materials examples in text (*cont.*)
- carbon nanotube, 342
 - Ca, 665
 - CaZrO₃, 337
 - catalyst particles, 277, 619
 - CdTe, 165
 - Co, 545
 - CoGa, 244, 447
 - Co-Cr-Ta, 537
 - Cr film, 62, 564, 576–584, 602, 677
 - CsCl, 244
 - Cu, 26, 40–42, 314, 317, 381, 386, 408, 411, 427, 435, 436, 583, 592, 618, 681
 - Cu-Al, 339
 - CuAu, 381
 - Cu₃Au, 244
 - CuCl₆PC, 509
 - Cu-Co, 417
 - CuZn, 244
 - diamond, 453, 701
 - Fe, 535, 624, 681, 698; *see also* Stainless steel; Steel
 - FeAl, 244
 - Fe₃Al, 244
 - Fe-Cr-O, 593
 - Fe-Mo, 259
 - Fe-Ni, 535
 - Fe-Ni-Cr, 412, 627
 - Fe₂O₃, 278, 477
 - Fe₃O₄, 540
 - ferrite, 416
 - ferroelectric, 534
 - GaAs, 9, 218, 240, 243, 245, 246, 272, 370, 376, 377, 382, 386, 390, 518, 538, 541, 616
 - Ge, 360, 386, 415, 444, 477, 504, 511, 547, 557
 - glass
metallic, 274
oxide, 274, 594
silica, 276, 557
silicate, 538, 562
 - graphite, 409; *see also* Carbon
 - hematite, 416
 - high-T_c superconductor, 478, 534
 - hydrofluoric acid, 157
 - icosahedral quasicrystal, 480, 494–496
 - InAs, 444
 - K₂O·7Nb₂O₅, 509
 - latex particle, 149, 354, 629
 - Mg, 569
 - MgO, 81, 273, 295, 370, 427, 448
 - Mo, 246
 - MoO₃, 152, 342
 - Na, 276
 - NaCl, 243
 - nanocrystals, 274, 277
 - Nb, 478, 522
 - Nb-Al, 615
 - Nb₁₂O₂₉, 491
 - Ni, 240, 410, 675
 - NiAl, 243, 244, 389
 - Ni₃Al, 240, 244, 389, 391, 408
- Materials examples in text (*cont.*)
- Ni-Cr-Mo, 617
 - NiFe₂O₄, 475
 - NiO, 391, 414, 416, 443, 446, 453, 475, 477, 503, 613, 643, 663
 - NiO-CaO, 341
 - NiO-ZrO₂, 698
 - nitric acid, 157
 - ordered intermetallic alloy, 245, 475
 - Pb, 546
 - perchloric acid, 157
 - perovskite, 478
 - polybutadiene, 699
 - polymer, 62, 167, 353–357
 - polystyrene, 699
 - polytype, 479
 - polytypoid, 479
 - Pt, 359
 - quantum-well heterostructure, 538
 - quartz, 10, 340
 - quasicrystal, 479, 494
 - Sb, 592
 - Si, 32, 111, 205, 239, 243, 246, 304, 360, 370, 386, 416, 434, 443, 516, 538, 544, 592, 692, 701, 702
 - SiC, 382
 - Si₃N₄, 477
 - SiO₂, 62, 356, 692, 699
 - Sigma (σ) phase, 308, 618
 - Si/Mo superlattice, 246
 - SnTe, 447
 - SnSe₂, 413
 - spinel, 7, 201, 390, 415, 431, 443, 455, 468, 475, 503, 658
 - SrTiO₃, 360
 - stainless steel, 333, 381, 595, 656
 - steel, 357, 388, 533
 - superconductor, 546
 - Ta, 592
 - Th, 683
 - Ti, 592
 - TiAl, 244
 - Ti₃Al, 381
 - TiC, 672
 - TiN, 672
 - TiO₂, 390
 - U, 480
 - vanadium carbide, 245, 246, 259, 260, 475
 - wurtzite, 243
 - Y, 592
 - YBCO, 448
 - yttrium–aluminum garnet, 110
 - Zn, 410
 - ZnO, 382, 493
 - ZnS, 108
- Material safety data sheet, 157
- Mean-free path, 25, 40, 623, 631, 679
elastic, 612, 623
inelastic, 623
plasmon, 657, 679
- Mean-square vibrational amplitude, 397
- Mechanical punch, 159

- Microanalysis, *see also* Spectrometer (EELS);
 Spectrometer (X-ray energy-dispersive);
 Spectrometer (X-ray wavelength-dispersive)
 qualitative, 589–594, 671–672
 quantitative, 599–618, 672–678
- Microdensitometer, 502
- Microdiffraction, 303, 342; *see also*
 Convergent-beam, diffraction
- Microdomain, 538
- Miller indices, 43, 185, 194, 195
- Miller–Bravais notation, 241, 242
- Minimum
 contrast, 467
 detectability, 631–635, 683
 detectable mass, 632, 634
 detectable signal-to-noise ratio, 472
 mass fraction, 632
 resolvable distance, 99
- MINIPACK-1, 522
- Mirror plane, 326, 328; *see also* Point group; Symmetry
- Mirror prism, 650
- Modulated structure, 478
- Moiré fringes, 267, 278, 279, 417, 444–449
 complex, 448
 general, 445
 rotational, 444, 445, 447
 translational, 444, 445, 446
- Möllenstedt spectrometer, 696
- Momentum transfer, 699
- Monte-Carlo simulation, 15, 25, 624
- Moseley’s Law, 55
- Muffin-tin potential, 693
- Multi-channel analyzer (MCA), 558, 590, 593, 643, 670
- Multi-element spectrum, 603
- Multi-phase specimen, 625
- Multiple domains, 285
- Multiple least-squares fitting, 676, 681
- Multiple scattering: *see* Scattering, multiple
- Multislice calculation, 485, 488, 489, 522
- Murphy’s law, 114, 680
- Near-field calculation, 486
- Near-field regime, 211, 450
- Néel wall, 536
- NIST
 multi-element glass, 606
 oxide glass, 594
 Sandia/JCPDS electron diffraction database, 285
 thin-film standard (SRM 2063), 606
- Noise, 560, 664; *see also* Signal-to-noise ratio analysis, 516
 reduction, 507, 516
- O-ring, 123, 124
- Objective lens, 92, 267, 534, 544, 576; *see also* Lens
 aperture, 103, 142, 351, 355, 358, 363, 373, 425, 441, 486, 490, 502–503, 534, 647
 astigmatism, 147, 425
- Objective lens (*cont.*)
 collection semiangle of, 98, 358, 364, 465
 defocus, 463, 467, 485, 504, 505, 512, 516, 544
 diaphragm, 578, 581, 582
 focal increment of, 152
 instability of, 471
 polepiece, 580
 rotation alignment of, 147
 transfer function of, 462
- Oblique-textured electron DP, 274
- Omega (Ω) filter, 639, 650
- On-axis image, 510–511
- Optic axis, 88; *see also* Lens
- Optical bench, 524
- Optical system, 459
- Ordering, 538
 long-range 245, 260, 475
 short-range, 258, 538
- Orientation imaging, 297
- Orientation relationship, 280–285
 cube/cube, 284
 Kurdjumov–Sachs, 285
 Nishiyama–Wasserman, 285
 precipitate-matrix, 284
- Overfocus, 91, 148, 188, 307, 460, 533, 534; *see also* Lens; Underfocus
- Overvoltage, 53, 533, 534
- Oxide layer, 540
- p-i-n device, 560
- p–n junction, 108, 543
- Parallax shift, 531, 532, 629
- Paraxial-ray condition, 94, 98, 101
- Particle on a substrate, 374
- Pascal, 119
- Passband, 467
- Path difference, 27, 182, 183
- Path length, 577; *see also* Absorption of X-rays
- Pathological overlap, 591
- Pattern recognition, 513
- Pauli exclusion principle, 691
- Peak (X-ray characteristic)
 deconvolution of, 593
 integration of, 603
 overlap of, 590
 visibility of, 593
- Peak-to-background ratio, 570, 577, 582, 583, 584, 589, 632
- Periodic-continuation method, 494
- Phase
 boundary, 381, 391, 47; *see also* Interface
 contrast, 349, 439–455, 463, 535; *see also*
 Contrast
 difference, 240
 distortion function, 463
 of electron wave, 207
 factor, 206, 207, 243, 384
 grating, 485, 486
 negative, 463
 object approximation, 461
 reconstructed, 508
 shift, 463
- Phase (*cont.*)
 transformation, 416, 546
- Phasor diagram, 27, 383, 430
- Phonon, 61, 656
- Phosphorescence, 108
- Photodiode array, 644; *see also* Diode array
- Photographic dodging, 501
- Photographic emulsion, 114
- Photomultiplier, 110, 643; *see also* Scintillator; photomultiplier detector
- pi (π)
 fringe, 389
 orbital, 658
 peak, 671
 state, 692
- Pixel, 472
- Planar defect, 256, 257, 379–399, 413, 419, 431; *see also* Grain, boundary; Stacking fault; Twin boundary inclined, 629
- Planar interface, 578
- Plane normal, 269, 284
- Plane wave, 44, 231
 amplitude, 221
- Plasma ashing, 123
- Plasmon, 60, 656–657, 696–697
 energy, 657, 696
 excitation, 655
 frequency, 657
 loss, 696; *see also* Low-loss spectrum
 microanalysis, 696
 peak, 664, 674
 mean-free path, 657, 679
- Plural elastic scattering, 23, 468, 655, 669, 674, 678, 679, 689, 694; *see also* Elastic, scattering; Scattering, elastic
- Point defect, 259, 476; *see also* Interstitial atom; Vacancy
- Point group, 323, 328, 331, 332, 334
 determination of, 330
 symmetry of, 326
 two-dimensional, 330
- Point-spread function, 459, 462, 646, 680
- Point-to-point resolution, 443, 468
- Poisson statistics, 564
- Poisson’s ratio, 418
- Polepiece: *see* Lens
- Polycrystalline material, 273
- Polymer, 62, 167, 353–357
- Polytype, 479
- Polytypoid, 479
- Post-specimen lens, 316, 352, 359, 641; *see also* Lens
- Potential
 inner, 218, 219, 221, 452, 454, 496
 periodic, 217
 projected, 492, 514, 531
 well, 493
- Precision ion milling, 164
- Precision ion polishing, 164
- Primitive great circle, 269, 270; *see also* Stereogram

- Primitive lattice, 239, 240, 325; *see also* Crystal; Lattice
 Principal quantum number, 691
 Probability map, 486
 Probe, 134; *see also* Beam (electron) current, 582
 size, 589
 Processing HRTEM image: *see* Image, processing of
 Propagator matrix, 384
 Pulse processing, 563
 Pump, vacuum, 119–122
 cryogenic, 121
 diffusion, 120
 dry, 120
 ion, 121
 roughing, 119
 turbomolecular, 120
- Quadrupole, 93, 642; *see also* Lens
 Qualitative microanalysis, 587–595, 671
 Quantifying HRTEM images, 499–527
 Quantitative
 chemical lattice imaging, 514–518
 defect contrast imaging, 396
 HRTEM, 469, 485–526
 image analysis, 512
 mass-thickness contrast, 357
 microanalysis, 599–618, 672–677
 QUANTITEM, 514–516
 Quantum-mechanical convention, 212
 Quantum number, 691
 Quasicrystal structure, 480, 695
- Radial-distribution function (RDF), 276, 695
 Radiation damage, 61, 409; *see also* Beam (electron) damage
 Radiolysis, 61; *see also* Beam (electron) damage
 Ray diagram, 87–90
 Rayleigh criterion, 6, 79, 100, 466
 Rayleigh disk, 459
 Real space, 523
 approach, 488, 514
 crystallography, 373
 patching method, 494
 unit cell, 245
 vector, 217
 Reciprocal lattice, 193–196, 200, 223, 240, 241, 245, 260, 262, 273, 309, 391, 485, 486, 504, 510, 523
 formulation of, 486
 origin of, 193, 197
 point, 244
 rod, 196, 254; *see also* Relrod
 spacing, 490
 vector, 182, 193–195, 273, 279, 280, 459; *see also* Diffraction vector
 Reciprocity theorem, 365
 Recombination center, 543
 Reference spectra, 604, 671
 Reflection electron microscopy, 540
 Reflection high-energy electron diffraction, 540
 Refractive index, 207, 212, 220
 Relative-transition probability, 609
 Relative transmission, 629
 Relativistic effect, 13
 Relrod, 196, 253, 255, 256, 257, 258, 261, 262, 272, 310, 371, 391, 392, 403; *see also* Reciprocal lattice rod
 Replica, 148, 168, 357
 Resolution, 6, 99–101
 atomic level, 360
 limit, 5, 6, 100
 theoretical, 99
 Resolving power, 99
 Reverse-bias detector, 109, 560
 Richardson's Law, 69
 Right-hand rule, 94
 Rigid-body translation, 381
 Rose corrector, 470
- Safety, 10, 157
 Scan coil, 136, 309
 Scanning image, 115, 146
 Scanning transmission electron microscope (STEM), 8, 480, 647
 annular dark-field image, 356
 bright-field image, 144, 355
 dark-field image, 145, 356
 detectors in, 351, 364
 diffraction contrast in, 364
 digital imaging, 700
 image magnification in, 148
 mass-thickness contrast in, 355
 mode, 555
 Z contrast in, 358; *see also* Z contrast
 Scattering, 21–66, 309; *see also* Angle; Coherent; Elastic
 coherent, 22
 cross-section, 589
 elastic, 22, 37–45, 624, 655
 factor: *see* Atomic scattering factor
 forward, 23, 26, 207
 incoherent, 22, 361
 inelastic, 23, 51–66, 409, 639
 intershell, 693
 intrashell, 693
 matrix, 383, 384
 multiple, 23, 468, 486, 655, 693
 multiple-scattering calculations, 693–694
 nuclear, 42
 plural, 23, 655
 post-specimen, 580
 Rutherford, 39–41, 353, 358
 semiangle of, 30, 184, 655
 single, 23, 274, 624, 655, 679, 681–682, 689, 694, 697, 699
 strength, 204
 thermal-diffuse, 189, 309
 Scherzer, 470
 defocus, 465, 466, 467, 469, 470, 505
 Schottky
 diode, 109; *see also* Detector (electron)
- Schottky (*cont.*)
 emitter, 70, 473
 Schrödinger equation, 212, 217–219, 221, 470, 676
 Scintillation, 108
 Scintillator-photomultiplier detector, 110, 451, 541, 643, 644
 after-glow, 670
 shield, 645
 Screw axis, 333, 335; *see also* Space Group; Symmetry, screw axis
 Secondary electron, 57
 detector, 113
 fast, 57
 imaging of, 541
 slow, 57
 types of, 541
 Selected area diffraction (SAD), 140, 185, 187, 267, 272, 277, 285, 303, 314, 363, 374, 508
 aperture, 141, 186
 error, 186, 187
 pattern exposure, 188
 Selection rules, 240, 272
 Semiangle: *see* Angle; Bragg; Collection semiangle; Convergence semiangle; Incidence semiangle
 Semiconductor detector, 108, 559
 Semi-quantitative analysis, 672
 Shadowing, 168, 354, 493
 Shape effect, 253, 273
 Short-range ordering, 538
 Silicon dumbbells, 442
 Si(Li) detector, 559–562, 590, 591; *see also* Spectrometer (X-ray energy-dispersive)
 SI units, 13
 Side-entry holder, 124, 125, 268; *see also* Specimen, holder
 SIGMAK(L) program, 676
 Signal processing, 356
 Signal-to-background ratio (jump ratio), 683
 Signal-to-noise ratio, 473, 507, 521, 541, 543, 559, 562
 Single-atom detection, 684
 Single-atom imaging, 480
 Single-electron counting, 644
 Single-electron interaction, 658
 Single-period image, 514
 Single scattering: *see* Scattering, single
 Single-sideband holography, 544
 Slow-scan CCD, 504, 510, 521, 650; *see also* Charge-coupled device (CCD)
 Small circle, 269; *see also* Stereogram
 Smearing function, 459; *see also* Point-spread function
 Space group, 332, 491
 Spatial coherence, 72, 82, 450, 466
 Spatial resolution, 308, 590, 623–631, 633, 649, 682
 Specimen
 90°-wedge, 169
 artifacts in, 10, 172, 493, 676
 cooling of, 127, 164

- Specimen (*cont.*)**
- damage to, 639; *see also* Beam (electron) damage
 - density of, 614
 - drift of, 628, 632
 - height of, 95, 139, 306, 532; *see also* z control
 - holder, 117–129
 - bulk, 126
 - cooling, 127
 - double tilt, 126
 - EBIC, 127
 - heating, 127, 502
 - low-background, 127
 - low-background, double-tilt, cooling, 304
 - multiple, 126
 - quick change, 126
 - single-tilt, 125
 - spring clips for, 125
 - straining, 127, 502
 - tilt-rotation, 127, 304
 - top-entry, 124, 125
 - orientation of, 280
 - preparation of, 11, 157–173
 - rotation of, 164
 - self-supporting, 158, 579, 582
 - surface of, 258, 371, 381, 470
 - thickness of, 308, 353, 485, 516, 613, 614, 657, 669, 675, 679; *see also* Thickness
 - tilt axis, 152
 - tilting of, 268
 - transmission function, 461
 - vibration, 472
 - wedge-shaped, 212, 256, 369, 371, 391
- Spectrometer (EELS) 639–651; *see also* Electron, energy-loss spectrometry (EELS)**
- aberrations of, 641
 - artifacts in, 664
 - calibration of, 642
 - collection semiangle of, 647
 - dispersion of, 645, 670
 - entrance aperture of, 647, 648, 649, 669
 - entrance slit of, 642, 646
 - focusing of, 641
 - object plane of, 641
 - post-spectrometer slit, 650
 - resolution of, 645
- Spectrometer (X-ray energy-dispersive), 558–569**
- artifacts of, 568–570
 - Au absorption edge, 582
 - escape peak, 568, 591
 - incomplete-charge collection, 564, 565, 604
 - internal-fluorescence peak, 569, 582, 594
 - sum peak, 569, 591, 594
 - system peaks, 590
 - Au contact layer, 610
 - automatic shutter, 581
 - clock time, 564, 567
 - collection angle of, 559, 562, 575, 578
- Spectrometer (X-ray energy-dispersive) (*cont.*)**
- contamination of, 565
 - dead layer, 560, 610
 - dead time, 563, 566, 590
 - efficiency of, 610
 - leakage current of, 564
 - live time, 564
 - performance criteria for, 564
 - residuals in, 605
 - shutter, 565, 578
 - take-off angle of, 575, 576, 578, 613, 614
 - time constant, 563, 590, 593, 567
 - window, 560–562, 575,
- Spectrometer (X-ray wavelength-dispersive), 570, 599**
- Spectrum**
- electron energy-loss, 655–666, 689–703
 - X-ray, 52–56, 555, 590–592
- Spectrum imaging, 700**
- Sphere of projection 269; *see also* Stereographic projection**
- Spherical aberration, 79, 97, 138, 187, 463, 504–505, 541, 544, 646; *see also* Aberration**
- broadening, 683
 - coefficient, 79, 98, 267
 - error, 100
- Spin quantum number, 691**
- Spin-orbit splitting, 691**
- Spinodal decomposition, 479, 538**
- Spurious peak, 590**
- Spurious X-ray, 575, 578**
- Sputtering, 61, 606**
- Stacking fault, 232, 257, 262, 381, 383, 385, 386, 407, 478; *see also* Planar defect**
- contrast, 411
 - energy, 407, 410, 419, 432
 - fringes, 386–387, 395
 - inclined, 431
 - intrinsic, 387, 432
 - overlapping, 388, 432
- Stage 124, 576**
- Staining, 355**
- Standard Cr film, 574, 576–579, 581, 583, 602, 677**
- Standard specimen, 599, 605**
- Stationary-phase method, 429**
- Statistical criterion, 593, 632**
- Statistically significant peak, 593–594**
- Stereogram, 284, 285**
- Stereographic projection, 269, 280, 295, 311, 326**
- Stereology, 532**
- Stereomicroscopy, 268, 403, 412, 531–532**
- Stigmators, 99; *see also* Astigmatism**
- Strain, 403**
- analysis of, 338
 - contrast, 417
 - field, 403–420, 427
 - lattice, 702
 - measurement of, 338
- Straining holder, 127, 502; *see also* Specimen, holder**
- Stress, 403**
- Stress field, 403**
- Strong-beam image, 361, 383, 433, 435**
- Structure correlation, 277**
- Structure factor, 43, 204, 239, 240, 243, 248, 253, 256, 267, 354, 496, 702**
- Structure-factor-modulus restoration, 510**
- Student *t* value, 607**
- Substitutional atom, 258**
- Substitutional site, 616**
- Substrate, 284**
- Sum peak, 569, 591, 594**
- Summation approach, 253**
- Superlattice, 381, 478, 538; *see also* Ordering dislocation, 407**
- reflection, 244, 245, 389, 538
- Surface**
- barrier detector, 108, 109
 - diffusion, 546
 - dislocation, 413, 414
 - faceting, 444
 - groove, 492
 - imaging, 540
 - layer, 413
 - plasmon, 658
 - reconstruction, 258, 540
 - relaxation, 538
 - of specimen, 258, 371, 381, 470
- Symmetry; *see also* Mirror plane; Point group; Space group**
- bright-field projection, 330, 331, 393
 - determination of, 323, 326
 - elements of, 270, 286
 - glide plane, 332
 - inversion, 326
 - projection-diffraction, 330
 - rotation axis, 328
 - rotational, 326
 - screw axis, 332, 495
 - three dimensional, 311, 315
 - translational, 326, 338
 - whole-pattern (WP), 329–331
 - zone-axis, 334
- System peaks, 590**
- Systematic absence, 273, 285; *see also* Forbidden reflection**
- Systematic row, 184, 335, 423; *see also* Diffraction pattern**
- Transmission electron microscope, 5–14, 131–153**
- Template, 514**
- Temporal coherence, 71; *see also* Spatial coherence**
- Texture, 273; *see also* Grain**
- Thermal-contraction coefficient, 339**
- Thermal-diffuse scattering, 189, 309**
- Thermionic gun 69, 76, 589; *see also* Gun**
- Thickness of specimen, 419, 610, 624, 628 dependence, 405**
- determination of, 321, 372, 518, 628–631, 678
 - effective, 375, 628

- Thickness of specimen (*cont.*)
 effect on contrast, 367–378
 fringe, 369, 371, 412, 416, 628
 simulation of, 375
 image, 700
- Thin-foil criterion, 600; *see also* Cliff-Lorimer
- Thin-foil effect 197, 255; *see also* Shape effect
- Threshold energy, 63; *see also* Beam
 (electron), damage
- Through-focus dark-field, 533; *see also* Dark field (DF) through focus (2 $\frac{1}{2}$)
- Through-focus image, 473, 481, 491, 510
- Tie line, 229, 230, 232, 235; *see also*
 Dispersion, surface
- Tilted-beam condition, 442
- Top-bottom effect, 278, 279
- Top-hat filter function, 603, 676
- Topotaxy, 278
- Torr, 119
- Trace element, 594, 680
- Transfer function, 462, 470, 504; *see also*
 Contrast, transfer function
 effective, 466
- Translation boundary, 381
- Tripod polisher, 160
- TV camera, 426; *see also* Charge-coupled device (CCD)
- Twin boundary, 258, 414, 415, 455, 478; *see also*
 Grain, boundary; Stacking fault
- Twin-jet apparatus, 162
- Two-beam
 approximation, 206, 437, 441
 calculation, 397, 418
 condition, 206, 209, 212, 223, 228, 234, 321,
 359, 361, 364, 371, 382, 384, 395, 423,
 616, 628
- Ultrahigh vacuum, 76, 119, 561
- Ultramicrotomy, 167
- Ultrasonic cleaning, 159
- Ultra-thin window, 591; *see also* Spectrometer (X-ray energy-dispersive)
- Uncollimated electrons, 578
- Underfocus, 91, 148, 188, 307, 533, 534; *see also* Lens; Overfocus
- Unfilled states, 689
- Unit cell, 204, 239, 311, 382, 508, 522; *see also* Crystal; Lattice
 determination of, 323
 image, 516
 scattering amplitude from, 240
 volume of, 194, 629
- Vacancy, 65
 loop, 410, 411; *see also* Dislocation loop
 ordered array, 245
- Vacuum, 119–122
- Vacuum (*cont.*)
 backing valve, 122
 high, 119
 low, 119
 pumps, 119–122
 rough, 119
 tweezers, 158, 170
 ultrahigh, 76, 119, 561
 wave vector in, 230
- Vacuum level, 689
- Valence-state image, 700
- V  g  rd's law, 338
- Video image, 502; *see also* Charge-coupled device (CCD)
- Viewing screen, 6, 107, 108
- Visible-light microscope, 6, 87
- Void, 451
- Voltage centering, 147, 468, 469
- Wafering saw, 159
- Water vapor, 560
- Wave
 equation, 217
 function, 452, 486
 matching construction, 229
 total amplitude of, 209, 253
 total function, 204, 218, 233
 vector, 181, 206, 220, 227, 228, 232, 452
 diffracted, 181
 incident, 181, 197
- Wavefront, 181
- Wavelength-dispersive spectrometer (WDS), 570, 599; *see also* Spectrometer (X-ray wavelength dispersive)
- Weak-beam dark field, 269, 362, 423–437; *See also* Dark field (DF)
 3g reflection, 424
 condition, 414
 of dislocation, 427
 thickness fringes in, 426
- Weak phase-object approximation , 462, 463, 489
- Wedge specimen, 212, 256, 369, 371, 391
- Wehnelt; *see also* Gun; Thermionic gun
 bias, 75
 cylinder, 72, 73
- Weighting factor, 240
- Weiss zone law, 185, 272, 309, 311
- White line, 671, 691
- White noise, 523
- White radiation, 197
- Wien Filter, 696
- Window (X-ray energy-dispersive spectrometer), 560, 561, 576
- Window polishing, 166, 582
- Windowless (X-ray energy-dispersive spectrometer) detector, 561, 576, 672
- Wobbling (lens), 137, 147
- Work function, 69
- World Wide Web, 13
- Wulff net, 269, 270, 280
- X-ray, 51–57, 555–635; *see also*
 Microanalysis; Spectrometer (X-ray energy-dispersive); Spectrometer (X-ray wavelength-dispersive)
 absorption of, 560, 577, 612, 630; *see also* Absorption (X-ray)
 absorption near-edge structure, 693
 atomic-number correction, 599, 610
 bremsstrahlung, 56, 558, 578–583, 601–602
 characteristic, 52, 558, 590
 count rate, 628
 depth distribution of, 609
 detector: *see* Spectrometer (X-ray energy-dispersive)
 diffraction, 179, 180
 emission of, 51, 609
 energy of, 55, 565
 energy-dispersive spectrometry (XEDS): *see*
 Microanalysis; Spectrometer (X-ray energy-dispersive)
 families of lines, 53, 591
 fluorescence, 582
 image, 618
 interaction volume, 625
 map, 619
 peak-to-background ratio, 582
 scattering factor, 397
 spectra, 52–56, 555, 590
- YAG scintillator, 644, 646
- Young's modulus, 418
- Young's slits, 11, 27, 182, 261
- Z contrast, 41, 353, 358–361, 693
- z control, 139, 307
- ZAF correction, 599
- Zero-loss
 integral, 676
 peak, 631, 642, 645, 646, 656, 670, 679
- Zero-order Laue zone, 198, 227, 279, 293, 309, 311, 323, 419, 424
- Zero-order wave, 45
- Zone axis, 185, 270, 272, 273, 293, 296, 445, 490, 516
 high-symmetry, 311
 image, 489
 low-symmetry, 311
 orientation, 316, 359, 583
 pattern, 284, 297, 304, 306, 321, 328, 331, 335, 373
 symmetry, 334

Acknowledgments for Reproduction of Figures

TEM is a visual science, and any TEM text is heavily dependent on figures and halftones to transmit its message. We have been fortunate to work with many colleagues over the years who have generously given us fine examples of the art and science of TEM; we would like to acknowledge them here. We have also used the work of others, whose permission has been sought as listed below.

Chapter 1

Figure 1.1: From Ruska, E. (1980) *The Early History of the Electron Microscope*, Fig. 6, reproduced by permission of S. Herzl Verlag GmbH & Co.

Figures 1.4A: Courtesy of S.M. Zemyan.

Figures 1.4B,C: Courtesy of S.M. Merchant.

Figure 1.6: Courtesy K.S. Vecchio.

Figure 1.7: Courtesy T. Hayes, from Hayes, T. (1980) in Johari, O. (Ed.) SEM—1980 1, 1, Fig. 8, reproduced by permission of Scanning Microscopy International.

Figure 1.9A: Courtesy of JEOL USA Inc.

Figure 1.9B: Courtesy of NSA Hitachi Scientific Instruments, Ltd.

Figure 1.9C: Courtesy of Philips Electronic Instruments, Inc.

Figure 1.9D: Courtesy of V.G. Scientific.

Chapter 2

Figure 2.4: Courtesy of J. Bruley and V.J. Keast.

Figure 2.8: Modified from Hecht, E. (1988) *Optics* Fig. 10.21, Addison-Wesley.

Figure 2.11A,D: Courtesy of K.S. Vecchio.

Figure 2.11C: Courtesy of D.W. Ackland.

Chapter 3

Figure 3.3: Courtesy of D.E. Newbury, from Newbury, D.E. (1986) in Joy, D.C., et al. (Eds.) *Principles of Analytical*

Electron Microscopy, p. 6, Fig. 2, reproduced by permission of Plenum Press.

Figure 3.4: Courtesy of D.E. Newbury, from data in Newbury D.E. (1986) in Joy, D.C., et al. (Eds.) *Principles of Analytical Electron Microscopy*, p. 8, Table II, reproduced by permission of Plenum Press.

Chapter 4

Figure 4.1: Courtesy of D.E. Newbury, from Newbury, D.E. (1986) in Joy, D.C., et al. (Eds.) *Principles of Analytical Electron Microscopy*, p. 20, Fig. 4, reproduced by permission of Plenum Press.

Figure 4.3: From Woldseth, R. (1973) *X-ray Energy Spectrometry*, Fig. 3, reproduced by permission of Kevex Instruments.

Figure 4.4: From Williams, D.B. (1987) *Practical Analytical Electron Microscopy in Materials Science*, 2nd Edition, Fig. 4.3, reproduced by permission of Philips Electron Optics.

Figure 4.11: Courtesy of L.W. Hobbs, from Hobbs, L.W. (1979) in Hren, J.J., et al. (Eds.) *Introduction to Analytical Electron Microscopy*, Fig. 17.2, reproduced by permission of Plenum Press.

Figure 4.12: Courtesy of L.W. Hobbs, from Hobbs, L.W. (1979) in Hren, J.J., et al. (Eds.) *Introduction to Analytical Electron Microscopy*, Fig. 17.4, reproduced by permission of Plenum Press.

Table 4.1: Courtesy of J.I. Goldstein, from Goldstein, J.I., et al. (1992) *Scanning Electron Microscopy and X-ray Microanalysis*, 2nd edition, Table 3.11, reproduced by permission of Plenum Press.

Table 4.2: Courtesy of N.J. Zaluzec and J.F. Mansfield, from Zaluzec, N.J. and Mansfield, J.F. in Rajan, K. (Ed.) *Intermediate Voltage Electron Microscopy and Its Ap-*

plication to Materials Science (1987), p. 29, Table 1, reproduced by permission of Philips Electron Optics.

Chapter 5

Figure 5.1: Modified from Hall, C.E. (1966) *Introduction to Electron Microscopy*, Fig. 7.8, McGraw-Hill.

Figure 5.4B: Courtesy of J.I. Goldstein, from Goldstein, J.I., et al. (1992) *Scanning Electron Microscopy and X-ray Microanalysis*, 2nd edition, Fig. 2.7, reproduced by permission of Plenum Press.

Figure 5.5: Courtesy of D.W. Ackland.

Figure 5.6: Courtesy of D.W. Ackland.

Figure 5.7A: Modified from Crewe, A.V., et al. (1969) *Rev. Sci. Instrum.* **40**, 241, Fig. 2.

Figure 5.7B: Courtesy of D.W. Ackland.

Figure 5.10: Courtesy of J.R. Michael, from Michael, J.R. and Williams, D.B. (1987) *J. Microsc.* **147**, 289, Fig. 3, reproduced by permission of the Royal Microscopical Society.

Figure 5.11A: Modified from Williams, D.B. (1987) *Practical Analytical Electron Microscopy in Materials Science*, 2nd Edition, Fig. 2.12b, Philips Electron Optics.

Figure 5.12: Courtesy of J.R. Michael, from Michael, J.R. and Williams, D.B. (1987) *J. Microsc.* **147**, 289, Fig. 2, reproduced by permission of the Royal Microscopical Society.

Figure 5.13A: Courtesy of D.W. Ackland.

Figure 5.13B: Courtesy of NSA Hitachi Scientific Instruments Ltd.

Chapter 6

Figure 6.7: Courtesy of D.W. Ackland.

Figure 6.8A: Courtesy of Philips Electronic Instruments Inc.

Figure 6.8B: Courtesy of Kratos Ltd.

Figure 6.8C: From Mulvey, T. (1974) *Electron Microscopy—1974*, p. 17, Fig. 1, reproduced by permission of the Australian Academy of Science.

Figure 6.8D: From Reimer, L. (1993) *Transmission Electron Microscopy*, 3rd edition, Fig. 2.12, reproduced by permission of Springer Verlag.

Figure 6.9: Modified from Reimer, L. (1993) *Transmission Electron Microscopy*, 3rd edition, Fig. 2.3, Springer Verlag.

Figure 6.10B: Courtesy of A.O. Benscoter.

Figure 6.11: Modified from Reimer, L. (1993) *Transmission Electron Microscopy*, 3rd edition, Fig. 2.13, Springer Verlag.

Figure 6.14: Modified from Reimer, L. (1993) *Transmission Electron Microscopy*, 3rd edition, Fig. 4.23, Springer Verlag.

Chapter 7

Figure 7.1: Modified from Stephen, J., et al. (1975) *J. Phys. E* **8**, 607, Fig. 2.

Figure 7.5: Modified from Williams, D.B. (1987) *Practical Analytical Electron Microscopy in Materials Science*, 2nd Edition, Fig. 1.2, Philips Electron Optics.

Figure 7.6: From Berger, S.D., et al. (1985) *Electron Microscopy and Analysis*, p. 137, Fig. 1, reproduced by permission of The Institute of Physics Publishing.

Chapter 8

Figure 8.1: Courtesy of W.C. Bigelow, from Bigelow, W.C. (1994) *Vacuum Methods in Electron Microscopy*, Fig. 4.1, reproduced by permission of Portland Press, Ltd.

Figure 8.2: Courtesy of W.C. Bigelow, from Bigelow, W.C. (1994) *Vacuum Methods in Electron Microscopy*, Fig. 5.1, reproduced by permission of Portland Press, Ltd.

Figure 8.3: Courtesy of Leybold Vacuum Products Inc.

Figure 8.4: Courtesy of W.C. Bigelow, from Bigelow, W.C. (1994) *Vacuum Methods in Electron Microscopy*, Fig. 7.1, reproduced by permission of Portland Press, Ltd.

Figure 8.6: Courtesy of Gatan Inc.

Figure 8.7: From Valdrè, U., and Gorringe, M.J. (1971) in Valdrè, U. (Ed.) *Electron Microscopy in Materials Science*, p. 217, Fig. 6, reproduced by permission of Academic Press Inc.

Figure 8.8: Courtesy of NSA Hitachi Scientific Instruments Ltd.

Figure 8.9A,B: Courtesy of Gatan Inc.

Figure 8.10A,B: Courtesy of Gatan Inc.

Figure 8.11: Courtesy of Gatan Inc.

Figure 8.12: From Komatsu, M., et al. (1994) *Journal of the American Ceramic Society* **77**, 839, Fig. 1, reproduced by permission of The American Ceramic Society.

Figure 8.13: Courtesy of NSA Hitachi Scientific Instruments Ltd.

Chapter 9

Figure 9.6: Modified from Reimer, L. (1993) *Transmission Electron Microscopy*, 3rd edition, Fig. 4.14a, Springer Verlag.

Figure 9.16: From Williams, D.B. (1987) *Practical Analytical Electron Microscopy in Materials Science*, 2nd Edition, Fig. 1.7, reproduced by permission of Philips Electron Optics.

Figure 9.18B,C,D: Courtesy of D.W. Ackland.

Figure 9.19: From Edington, J.W. (1976) *Practical Electron Microscopy in Materials Science*, Fig. 1.5, reproduced by permission of Philips Electron Optics.

Figure 9.20: Courtesy of S. Ramamurthy.

Figure 9.21: Courtesy of D.W. Ackland.

Figure 9.23: Courtesy of D.W. Ackland.

Figure 9.24: Courtesy of D.W. Ackland.

Figure 9.25: Courtesy of S. Ramamurthy.

Table 9.1: From Williams, D.B. (1987) *Practical Analytical Electron Microscopy in Materials Science*, 2nd Edition, Table 2.4, reproduced by permission of Philips Electron Optics.

Table 9.2: From Williams, D.B. (1987) *Practical Analytical Electron Microscopy in Materials Science*, 2nd Edition, Table 2.2, reproduced by permission of Philips Electron Optics.

Chapter 10

Figure 10.1: Modified from Médard, L., et al. (1949) *Rev. Met.* **46**, 549, Fig.5.

Figure 10.2: Courtesy of SPI Inc.

Figure 10.3: Courtesy of Gatan Inc.

Figure 10.4: Courtesy of VCR Inc.

Figure 10.7A: From Thompson-Russell, K.C. and Edington, J.W. (1977) *Electron Microscope Specimen Preparation Techniques in Materials Science*, Fig. 9, reproduced by permission of Philips Electron Optics.

Fig. 10.7b: From Thompson-Russell, K.C. and Edington, J.W. (1977) *Electron Microscope Specimen Preparation Techniques in Materials Science*, Fig. 7, reproduced by permission of Philips Electron Optics.

Figure 10.8: From Thompson-Russell, K.C. and Edington, J.W. (1977) *Electron Microscope Specimen Preparation Techniques in Materials Science*, Fig. 12, reproduced by permission of Philips Electron Optics.

Figure 10.9: Modified from Thompson-Russell, K.C. and Edington, J.W. (1977) *Electron Microscope Specimen Preparation Techniques in Materials Science*, Fig. 11, Philips Electron Optics.

Figure 10.10: Courtesy of R. Alani, Gatan Inc.

Figure 10.11: Courtesy of A.G. Cullis, from Cullis, A.G., et al. (1985) *Ultramicroscopy* **17**, 203, Figs. 1a, 3, reproduced by permission of Elsevier Science B.V.

Figure 10.12: From van Hellemont, J., et al. (1988) in Bravman, J., et al. (Eds.) *Specimen Preparation for Transmission Electron Microscopy of Materials*, Mat. Res. Soc. Symp. **115**, 247, Fig. 1, reproduced by permission of MRS.

Figure 10.15: From Thompson-Russell, K.C. and Edington, J.W. (1977) *Electron Microscope Specimen Preparation Techniques in Materials Science*, Figs. 20, 21, reproduced by permission of Philips Electron Optics.

Figure 10.16: From Thompson-Russell, K.C. and Edington, J.W. (1977) *Electron Microscope Specimen Preparation*

Techniques in Materials Science, Fig. 25, reproduced by permission of Philips Electron Optics.

Figure 10.17: From Hetherington, C.J.D. (1988) in Bravman, J., et al. (Eds.) *Specimen Preparation for Transmission Electron Microscopy of Materials*, Mat. Res. Soc. Symp. **115**, 143, Fig. 1, reproduced by permission of MRS.

Figure 10.18: Modified from Dobisz, E.A., et al. (1986) *J. Vac. Sci. Technol. B* **4**, 850, Fig. 1, reproduced by permission of MRS.

Figure 10.19: From Fernandez, A. (1988) in Bravman, J., et al. (Eds.) *Specimen Preparation for Transmission Electron Microscopy of Materials*, Mat. Res. Soc. Symp. **115**, 119, Fig. 1, reproduced by permission of MRS.

Figure 10.20: Courtesy of P. Goodhew, from Goodhew, P.J. (1988) in Bravman, J., et al. (Eds.) *Specimen Preparation for Transmission Electron Microscopy of Materials*, Mat. Res. Soc. Symp. **115**, 52, reproduced by permission of MRS.

Table 10.1: Courtesy of T. Malis.

Chapter 11

Table 11.1: Modified from Hirsch, P.B., et al. (1977) *Electron Microscopy of Thin Crystals*, 2nd edition, p. 19, Krieger.

Chapter 13

Table 13.2: Modified from Reimer, L. (1993) *Transmission Electron Microscopy*, 3rd edition, Table 7.2, p. 296, Springer Verlag.

Chapter 14

Figure 14.2: Modified from Hashimoto, H., et al. (1962) *Proc. Roy. Soc. (London)* **A269**, 80, Fig. 2.

Table 14.2: Modified from Reimer, L. (1993) *Transmission Electron Microscopy*, 3rd edition, Table 3.2, p. 58, Springer Verlag.

Chapter 16

Figure 16.5: Courtesy of M.L. Jenkins, from Jenkins, M.L., et al. (1976) *Phil. Mag.* **34**, 1141, Fig. 2, reproduced by permission of Taylor and Francis.

Figure 16.6: Courtesy of B.C. De Cooman.

Figure 16.7: From Dodsworth, J., et al. (1983) *Adv. Ceram.* **6**, 102, Fig. 3, reproduced by permission of the American Ceramic Society.

Figure 16.8: Courtesy of B.C. De Cooman.

Figure 16.9: From Gajdardziska-Josifovska, M., et al. (1995) *Ultramicroscopy* **58**, 65, Fig. 1, reproduced by permission of Elsevier Science B.V.

Figure 16.10: Courtesy of S. McKernan.

Figure 16.11: From Hahn, T. (Ed.) *International Tables for Crystallography A*, pp. 538–539, No. 164, reproduced by permission of The International Union of Crystallography.

Table 16.1: Modified from Edington, J.W. (1976) *Practical Electron Microscopy in Materials Science*, Appendix 8, Van Nostrand Reinhold.

Chapter 17

Figure 17.2: From Edington, J.W. (1976) *Practical Electron Microscopy in Materials Science*, Fig. 2.16, reproduced by permission of Philips Electron Optics.

Figure 17.9: Modified from Hirsch, P.B., et al. (1977) *Electron Microscopy of Thin Crystals*, 2nd edition, Fig. 4.11, Krieger.

Figure 17.7: From Carter, C.B., et al. (1981) *Phil. Mag.* **A43**, 441, Fig. 5c, reproduced by permission of Taylor and Francis.

Figure 17.10: From Driver, J.H., et al. (1972) *Phil Mag.* **26**, 1227, Fig. 3, reproduced by permission of Taylor and Francis.

Figure 17.11A–C: From Lewis, M.H., and Billingham, J. (1972) *JEOL News* **10e**(1), 8, Fig. 3, reproduced by permission of JEOL USA Inc.

Figure 17.11D: Modified from Sauvage, M. and Parthè, E. (1972) *Acta Cryst.* **A28**, 607, Fig. 2.

Figure 17.12: Modified from Carter, C.B., et al. (1981) *Phil. Mag.* **A43**, 441, Figs. 5a, b.

Figure 17.13: Modified from Carter, C.B., et al. (1980) *J. Electron Microsc.* **63**, 623, Fig. 8.

Figure 17.14: Modified from Carter, C.B. (1984) *Phil. Mag.* **A50**, 133, Figs. 1–3.

Chapter 18

Figure 18.2: From Edington, J.W. (1976) *Practical Electron Microscopy in Materials Science*, Fig. A1.7, reproduced by permission of Philips Electron Optics.

Figure 18.7: Courtesy of S. Ramamurthy.

Figure 18.9: Courtesy of S. McKernan.

Figure 18.10A,C: Courtesy of S. McKernan.

Figure 18.10B,D,E: From Vainshtein, B.K., et al. (1992) in Cowley, J.M. (Ed.) *Electron Diffraction Techniques 1*, Fig. 6.13, reproduced by permission of Oxford University Press.

Figure 18.11: Modified from James, R.W. (1965) in Bragg, L. (Ed.) *The Optical Principles of the Diffraction of X-ray*, Vol. II of the Crystalline State, Figs. 170, 184, Cornell University Press.

Figure 18.12: Courtesy of D.J.H. Cockayne, from Sproul, A.,

et al. (1986) *Phil. Mag.* **B54**, 113, Fig. 1, reproduced by permission of Taylor and Francis.

Figure 18.13: From Graczyk, J.F. and Chaudhari, P. (1973) *Phys. stat. sol. (b)*, **58**, 163, Fig. 10a, reproduced by permission of Akademie Verlag GmbH.

Figure 18.14: Courtesy of A. Howie, from Howie, A. (1988) in Buseck, P.R., et al. (Eds.) *High-Resolution Transmission Microscopy and Associated Techniques*, p. 607, Fig. 14.12, reproduced by permission of Oxford University Press.

Figure 18.15: From Tietz, L.A., et al. (1995) *Ultramicroscopy* **60**, 241, Figs. 2, 3, 4, reproduced by permission of Elsevier Science B.V.

Figure 18.16: From Tietz, L.A., et al. (1995) *Ultramicroscopy* **60**, 241, Fig. 5, reproduced by permission of Elsevier Science B.V.

Figure 18.17: From Andrews, K.W., et al. (1971) *Interpretation of Electron Diffraction Patterns*, 2nd edition, Fig. 41, reproduced by permission of Plenum Press.

Figure 18.18: From Andrews, K.W., et al. (1971) *Interpretation of Electron Diffraction Patterns*, 2nd edition, Fig. 41, reproduced by permission of Plenum Press.

Figure 18.19: From Andrews, K.W., et al. (1971) *Interpretation of Electron Diffraction Patterns*, 2nd edition, Fig. 41, reproduced by permission of Plenum Press.

Figure 18.20: From Edington, J.W. (1976) *Practical Electron Microscopy in Materials Science*, Fig. 2.20, reproduced by permission of Philips Electron Optics.

Chapter 19

Figure 19.6A: Courtesy of G. Thomas, from Levine, E., et al. (1966) *J. Appl. Phys.* **37**, 2141, Fig. 1a, reproduced by permission of the American Institute of Physics.

Figure 19.7: Modified from Okamoto, P.R., et al. (1967) *J. Appl. Phys.* **38**, 289, Fig. 5.

Figure 19.8: Courtesy of S. Ramamurthy.

Figure 19.9A: Modified from Thomas, G. and Goringe, M.J. (1979) *Transmission Electron Microscopy of Metals*, Fig. 2.30, John Wiley & Sons Inc.

Figure 19.9B: Modified from Edington, J.W. (1976) *Practical Electron Microscopy in Materials Science*, Fig. 2.27, Van Nostrand Reinhold.

Figure 19.11: Modified from Thomas, G. and Goringe, M.J. (1979) *Transmission Electron Microscopy of Metals*, Fig. 2.29, John Wiley & Sons Inc.

Chapter 20

Figure 20.2A: Courtesy of K.S. Vecchio, from Williams, D.B., et al. (Eds.) (1992) *Images of Materials*, Fig. 6.5, reproduced by permission of Oxford University Press.

- Figure 20.2B: Courtesy of K.S. Vecchio, from Williams, D.B., et al. (Eds.) (1992) *Images of Materials*, Fig. 6.17, reproduced by permission of Oxford University Press.
- Figure 20.3: Modified from Williams, D.B. (1987) *Practical Analytical Electron Microscopy in Materials Science*, 2nd Edition, Fig. 6.6, Philips Electron Optics.
- Figure 20.5: From Lyman, C.E., et al. (Eds.) (1990) *Scanning Electron Microscopy, X-ray Microanalysis and Analytical Electron Microscopy—a Laboratory Workbook*, Fig. A27.2, reproduced by permission of Plenum Press.
- Figure 20.6: Courtesy of J.F. Mansfield, from Mansfield, J.F. (1984) *Convergent Beam Diffraction of Alloy Phases*, Fig. 5.3, reproduced by permission of Institute of Physics Publishing.
- Figure 20.7C: Courtesy of R. Ayer.
- Figure 20.8A: Modified from Ayer, R. (1989) *J. Electron Microscop. Tech.* **13**, 3, Fig. 3.
- Figure 20.9: From Williams, D.B. (1987) *Practical Analytical Electron Microscopy in Materials Science*, 2nd Edition, Fig. 6.13, reproduced by permission of Philips Electron Optics.
- Figure 20.10: From Williams, D.B. (1987) *Practical Analytical Electron Microscopy in Materials Science*, 2nd Edition, Fig. 6.14, reproduced by permission of Philips Electron Optics.
- Figure 20.11: Courtesy of W.A.T. Clark, from Heilman, P., et al. (1983) *Acta Met.* **31**, 1293, Fig. 4, reproduced by permission of Elsevier Science B.V.
- Figure 20.12: From Williams, D.B. (1987) *Practical Analytical Electron Microscopy in Materials Science*, 2nd Edition, Fig. 6.9, reproduced by permission of Philips Electron Optics.
- Figure 20.13: From Williams, D.B. (1987) *Practical Analytical Electron Microscopy in Materials Science*, 2nd Edition, Fig. 6.16, reproduced by permission of Philips Electron Optics.
- Figure 20.14: Courtesy of C.M. Sung.
- Figure 20.15: Courtesy of B. Ralph, from Williams, D.B. (1987) *Practical Analytical Electron Microscopy in Materials Science*, 2nd Edition, Fig. 6.18, reproduced by permission of Philips Electron Optics.
- Figure 20.16: Courtesy of K.S. Vecchio, from Williams, D.B., et al. (Eds.) (1992) *Images of Materials*, Fig. 6.14, reproduced by permission of Oxford University Press.
- lytical Electron Microscopy in Materials Science, 2nd Edition, Figs. 4.29b, c, reproduced by permission of Philips Electron Optics.
- Figure 21.4: Courtesy of R. Ayer, from Raghavan, M., et al. (1984) *Met. Trans.* **15A**, 783, Fig. 6, reproduced by permission of ASM International.
- Figure 21.5A: Courtesy of K.S. Vecchio, from Williams, D.B., et al. (Eds.) (1992) *Images of Materials*, Fig. 6.23, reproduced by permission of Oxford University Press.
- Figure 21.5B: Courtesy of R. Ayer, from Ayer, R. (1989) *J. Electron Microscop. Tech.* **13**, 3, Fig. 7, reproduced by permission of John Wiley & Sons Inc.
- Figure 21.7: Courtesy of K.S. Vecchio, from Williams, D.B., et al. (Eds.) (1992) *Images of Materials*, Fig. 6.19, reproduced by permission of Oxford University Press.
- Figure 21.8: Courtesy of V.P. Dravid.
- Figure 21.9A–D: Courtesy of J.W. Steeds, from Chapman J.N. and Craven, A.J. (Eds.) (1984) *Quantitative Electron Microscopy*, p. 68, Fig. 8, reproduced by permission of the Scottish Universities Summer School in Physics.
- Figure 21.9E: Courtesy of K.S. Vecchio, from Williams, D.B., et al. (Eds.) (1992) *Images of Materials*, Fig. 6.25, reproduced by permission of Oxford University Press.
- Figure 21.10: Courtesy of K.S. Vecchio, from Williams, D.B., et al. (Eds.) (1992) *Images of Materials*, Fig. 6.24, reproduced by permission of Oxford University Press.
- Figure 21.11: Courtesy of K.S. Vecchio and V.P. Dravid, from Williams, D.B., et al. (Eds.) (1992) *Images of Materials*, Figs. 6.27, 6.28, reproduced by permission of Oxford University Press.
- Figure 21.12: Courtesy of K.S. Vecchio, from Williams, D.B., et al. (Eds.) (1992) *Images of Materials*, Fig. 6.29, reproduced by permission of Oxford University Press.
- Figure 21.13: Courtesy of K.S. Vecchio and V.P. Dravid, from Williams, D.B., et al. (Eds.) (1992) *Images of Materials*, Fig. 6.30, reproduced by permission of Oxford University Press.
- Figure 21.14: Courtesy of R. McConville, from Williams, D.B., et al. (Eds.) (1992) *Images of Materials*, Fig. 6.33, reproduced by permission of Oxford University Press.
- Figure 21.15: Courtesy of J.M. Cowley, from Liu, M. and Cowley, J.M. (1994) *Ultramicroscopy* **53**, 333, Figs. 1, 2, reproduced by permission of Elsevier Science B.V.
- Figure 21.16: Courtesy of W.D. Riecke, from Williams, D.B. (1987) *Practical Analytical Electron Microscopy in Materials Science*, 2nd Edition, Fig. 6.2, reproduced by permission of Philips Electron Optics.
- Figure 21.17: Courtesy of J.R. Michael.

Chapter 21

- Figure 21.1: From Williams, D.B. (1987) *Practical Analytical Electron Microscopy in Materials Science*, 2nd Edition, Fig. 4.29a, reproduced by permission of Philips Electron Optics.
- Figure 21.3: From Williams, D.B. (1987) *Practical Ana-*

- lytical Electron Microscopy in Materials Science*, 2nd Edition, p. 79, reproduced by permission of Philips Electron Optics.

Table 21.2: Data from Williams, D.B. (1987) *Practical Analytical Electron Microscopy in Materials Science*, 2nd Edition, p. 79, reproduced by permission of Philips Electron Optics.

Table 21.3: Courtesy of B.F. Buxton, from Buxton, B.F., et al. (1976) *Phil. Trans. Roy. Soc. (London)* **281**, 181, Table 2, reproduced by permission of The Royal Society.

Table 21.4: Courtesy of B.F. Buxton, from Buxton, B.F., et al. (1976) *Phil. Trans. Roy. Soc. (London)* **281**, 181, Table 3, reproduced by permission of The Royal Society.

Table 21.6: Courtesy of B.F. Buxton, from Buxton, B.F., et al. (1976) *Phil. Trans. Roy. Soc. (London)* **281**, 181, Table 4, reproduced by permission of The Royal Society.

Table 21.7: Courtesy of J.W. Steeds, from Steeds, J.W., et al. (1983) *J. Appl. Cryst.* **16**, 317, Tables 5, 6, reproduced by permission of the International Union of Crystallography.

Chapter 22

Figure 22.5: Courtesy of K.A. Repa.

Figure 22.6: From Williams, D.B. (1987) *Practical Analytical Electron Microscopy in Materials Science*, 2nd Edition, Fig. 3.7d, reproduced by permission of Philips Electron Optics.

Figure 22.7: Courtesy of K.B. Reuter.

Figure 22.8: From Williams, D.B. (1987) *Practical Analytical Electron Microscopy in Materials Science*, 2nd Edition, Fig. 3.7c, reproduced by permission of Philips Electron Optics.

Figure 22.9A,B: Courtesy of H. Tsai, from Williams, D.B. (1987) *Practical Analytical Electron Microscopy in Materials Science*, 2nd Edition, Fig. 1.19a, b, reproduced by permission of Philips Electron Optics.

Figure 22.9C: Courtesy of K.-R. Peters.

Figure 22.10: Modified from Williams, D.B. (1983) in Krawkow, W., et al. (Eds.) *Electron Microscopy of Materials*, Mat. Res. Soc. Symp. **31**, 11, Figs. 3a, b, MRS.

Figure 22.11A,B: Courtesy of I.M. Watt, from Watt, I.M. (1996) *The Principles and Practice of Electron Microscopy*, 2nd edition, Figs. 5.5a, b, reproduced by permission of Cambridge University Press.

Figure 22.12: Courtesy of M.M.J. Treacy, from Williams, D.B. (1987) *Practical Analytical Electron Microscopy in Materials Science*, 2nd Edition, Fig. 5.26b, reproduced by permission of Philips Electron Optics.

Figure 22.14: Courtesy of S.J. Pennycook, from Pennycook, S.J., et al. (1986) *J. Microsc.* **144**, 229, Fig. 8, reproduced by permission of the Royal Microscopical Society.

Figure 22.15A,B: Courtesy of S.J. Pennycook, from Lyman, C.E. (1992) *Microscopy: The Key Research Tool*, special publication of the EMSA Bulletin **22**, 7, Fig. 7, reproduced by permission of MSA.

Figure 22.15C: Courtesy of S.J. Pennycook, from Browning, et al. (1995) *Interface Science* **2**, 397, Fig. 4d, reproduced by permission of Kluwer.

Figure 22.16A: From Edington, J.W. (1976) *Practical Electron Microscopy in Materials Science*, Fig. 2.34, reproduced by permission of Philips Electron Optics.

Figure 22.17: Courtesy of D. Cohen.

Chapter 23

Figure 23.1: Courtesy of S. Ramamurthy.

Figure 23.2: From Edington, J.W. (1976) *Practical Electron Microscopy in Materials Science*, Fig. 3.2a, reproduced by permission of Philips Electron Optics.

Figure 23.3B: Courtesy of D. Cohen.

Figure 23.3C: Courtesy of S. King.

Figure 23.5: Courtesy of D. Susnitzky.

Figure 23.7: Modified from Edington, J.W. (1976) *Practical Electron Microscopy in Materials Science*, Fig. 3.3, Van Nostrand Reinhold.

Figure 23.8: Modified from Edington, J.W. (1976) *Practical Electron Microscopy in Materials Science*, Figs. 3.4b, d, Van Nostrand Reinhold.

Figure 23.9: Courtesy of S. Ramamurthy.

Figure 23.10: From Hashimoto H., et al. (1962) *Proc. Roy. Soc. (London)* **A269**, 80, Fig. 11, reproduced by permission of The Royal Society.

Figure 23.11A: Courtesy of NSA Hitachi Scientific Instruments Ltd.

Figure 23.11B,C: Courtesy of D. Cohen.

Figure 23.12: From Edington, J.W. (1976) *Practical Electron Microscopy in Materials Science*, Fig. 3.3d, reproduced by permission of Philips Electron Optics.

Figure 23.13B,C: From De Cooman, B.C., et al. (1987) in J.D. Dow and I.K. Schuller (Eds.) *Interfaces, Superlattices, and Thin Films*, Mat. Res. Soc. Symp. **77**, 187, Fig. 1, reproduced by permission of MRS.

Chapter 24

Figure 24.4A–D: Courtesy of D. Cohen.

Figure 24.4 E,F: Modified from Gevers, R., et al. (1963) *Phys. stat. sol.* **3**, 1563, Table 3.

Figure 24.5: From Föll, H., et al. (1980) *Phys. stat. sol. (a)* **58**, 393, Figs. 6a, c, reproduced by permission of Akademie Verlag GmbH.

Figure 24.7A,B: From Lewis, M.H. (1966) *Phil. Mag.* **14**, 1003, Fig. 9, reproduced by permission of Taylor and Francis.

Figure 24.7C,D: Courtesy of S. Amelinckx, from Amelinckx, S. and Van Landuyt, J. (1978) in S. Amelinckx, et

- al. (Eds.) *Diffraction and Imaging Techniques in Material Science I*, p. 107, Figs. 3, 18, North-Holland.
- Figure 24.8: From Rasmussen, D.R., et al. (1991) *Phys. Rev. Lett.* **66**, (20), 262, Fig. 2, reproduced by permission of The American Physical Society.
- Figure 24.9: Courtesy of S. Summerfelt.
- Figure 24.13: Modified from Metherell, A.J.F. (1975) in Valdrè, U. and Ruedl, E. (Eds.) *Electron Microscopy in Materials Science II*, 397, Fig. 13, Commission of the European Communities.
- Figure 24.14: From Hashimoto, H., et al. (1962) *Proc. Roy. Soc. (London)* **A269**, 80, Fig. 15, reproduced by permission of The Royal Society.
- Figure 24.16: Modified from Rasmussen, R., et al. (1991) *Phil. Mag.* **63**, 1299, Fig. 4.

Chapter 25

- Figure 25.2B: Modified from Amelinckx, S. (1964) *Solid State Physics Suppl.* **6**, Fig. 76.
- Figure 25.6A–C: Modified from Carter, C.B. (1980) *Phys. stat. sol. (a)* **62**, 139, Fig. 4.
- Figure 25.6f: From Van Landuyt, J., et al. (1970) *Phys. stat. sol.* **41**, 271, Fig. 19, reproduced by permission of Akademie Verlag GmbH.
- Figure 25.6G–H: Courtesy of B.C. De Cooman.
- Figure 25.7: Modified from Hirsch, P.B., et al. (1977) *Electron Microscopy of Thin Crystals*, 2nd edition, Fig. 7.8, Krieger.
- Figure 25.8: From Delavignette, P. and Amelinckx, S. (1962) *J. Nucl. Mat.* **5**, 17, Fig. 7, reproduced by permission of Elsevier Science B.V.
- Figure 25.10: From Urban, K. (1971) in Koda, S. (Ed.) *The World Through the Electron Microscope*, Metallurgy V, p. 26, reproduced by permission of JEOL USA Inc.
- Figure 25.11: Courtesy of A. Howie, from Howie, A. and Whelan, M.J. (1962) *Proc. Roy. Soc. (London)* **A267**, 206, Fig. 14, reproduced by permission of The Royal Society.
- Figure 25.12: Modified from M. Wilkens (1978) in Amelinckx, S., et al. (Eds.) *Diffraction and Imaging Techniques in Material Science I*, p. 185, Fig. 4, North-Holland.
- Figure 25.14: From Dupouy G. and Perrier, F. (1971) in Koda, S. (Ed.) *The World Through the Electron Microscope*, Metallurgy V, p. 100, reproduced by permission of JEOL USA Inc.
- Figure 25.15A: From Modeer, B. and Lagneborg, R. (1971) in Koda, S. (Ed.) *The World Through the Electron Microscope*, Metallurgy V, p. 44, reproduced by permission of JEOL USA Inc.
- Figure 25.15B: Courtesy of D.A. Hughes, from Hansen, N. and Hughes, D.A. (1995) *Phys. stat. sol. (a)* **149**, 155,

- Fig. 5, reproduced by permission of Akademie Verlag GmbH.
- Figure 25.16A: From Siems, F., et al. (1962) *Phys. stat. sol.* **2**, 421, Fig. 5a, reproduced by permission of Akademie Verlag GmbH.
- Figure 25.16C: From Siems, F., et al. (1962) *Phys. stat. sol.* **2**, 421, Fig. 15a, reproduced by permission of Akademie Verlag GmbH.
- Figure 25.17A: Modified from Whelan, M.J. (1958–59) *J. Inst. Met.* **87**, 392, Fig. 25a.
- Figure 25.17B: Courtesy of K. Ostyn.
- Figure 25.18: From Takayanagi, L. (1988) *Surface Science* **205**, 637, Fig. 5, reproduced by permission of Elsevier Science B.V.
- Figure 25.19A: From Tunstall, W.J., et al. (1964) *Phil. Mag.* **9**, 99, Fig. 9, reproduced by permission of Taylor and Francis.
- Figure 25.19B: From Amelinckx, S. in Merli, P.G. and Antissari, V.M. (Eds.) *Electron Microscopy in Materials Science*, p. 128, Fig. 45, reproduced by permission of World Scientific.
- Figure 25.20: Courtesy of W. Skrotsky.
- Figure 25.21: Courtesy of W. Skrotsky.
- Figure 25.22: From Carter, C.B., et al. (1986) *Phil. Mag.* **A55**, 21, Fig. 2, reproduced by permission of Taylor and Francis.
- Figure 25.23: From Carter, C.B., et al. (1981) *Phil. Mag.* **A43**, 441, Fig. 3, reproduced by permission of Taylor and Francis.
- Figure 25.24: Courtesy of K. Ostyn.
- Figure 25.25: Courtesy of L. Tietz.
- Figure 25.26A: Courtesy of L.M. Brown, from Ashby, M.F. and Brown, L.M. (1963) *Phil. Mag.* **8**, 1083, Fig. 10, reproduced by permission of Taylor and Francis.
- Figure 25.26B: Modified from Whelan, M.J. (1978) in Amelinckx, S., et al. (Eds.) *Diffraction and Imaging Techniques in Material Science I*, p. 43, Fig. 36, North-Holland.
- Figure 25.26C: Courtesy of L.M. Brown, from Ashby, M.F. and Brown, L.M. (1963) *Phil. Mag.* **8**, 1083, Fig. 12, reproduced by permission of Taylor and Francis.
- Figure 25.27: From Rasmussen, D.R. and Carter, C.B. (1991) *J. Electron Microsc. Technique* **18**, 429, Fig. 2, reproduced by permission of John Wiley & Sons Inc.
- Figure 25.27: From Rasmussen, D.R. and Carter, C.B. (1991) *J. Electron Microsc. Technique* **18**, 429, Fig. 2, reproduced by permission of John Wiley & Sons Inc.

Chapter 26

- Figure 26.7: Courtesy of S. King.
- Figure 26.10: Courtesy of D.J.H. Cockayne, from Cockayne,

- D.J.H. (1972) *Z. Naturforschung* **27a**, 452, Fig. 6c, reproduced by permission of Verlag der Zeitschrift für Naturforschung, Tübingen.
- Figure 26.13: Modified from Carter, C.B., et al. (1986) *Phil. Mag.* **A55**, 1, Fig. 9.
- Figure 26.15: Modified from Föll, H., et al. (1980) *Phys. stat. sol. (a)* **58**, 393, Figs. 6b, c.
- Figure 26.17: From Heidenreich, R.D. (1964) *Fundamentals of Transmission Electron Microscopy*, Fig. 9.20, reproduced by permission of John Wiley & Sons Inc.
- Figure 26.18: Courtesy of D.J.H. Cockayne, from Ray, I.L.F. and Cockayne, D.J.H. (1971) *Proc. Roy. Soc. (London A* **A325**, 543, Fig. 10, reproduced by permission of The Royal Society.
- Figure 26.23: Modified from Carter, C.B. (1979) *J. Phys. (A)* **54** (1) 395 Fig. 8a.

Chapter 27

- Figure 27.3A: From Izui, K.J., et al. (1977) *J. Electron Microsc.* **26**, 129, Fig. 1, reproduced by permission of the Japanese Society of Electron Microscopy.
- Figure 27.3C: Courtesy of J.C.H. Spence, from Spence, J.C.H. *Experimental High-Resolution Electron Microscopy*, Fig. 5.15, reproduced by permission of Oxford University Press.
- Figure 27.4B: Courtesy of J.L. Hutchison, from Hutchison, J.L., et al. (1991) in Heydenreich, J. and Neumann, W. (Eds.) *High-Resolution Electron Microscopy—Fundamentals and Applications*, p. 205, Fig. 3, reproduced by permission of Halle/Saale.
- Figure 27.4C: Courtesy of S. McKernan.
- Figure 27.4D: From Carter, C.B., et al. (1989) *Phil. Mag.* **A63**, 279, Fig. 3, reproduced by permission of Taylor and Francis.
- Figure 27.8: From Tietz, L.A., et al. (1992) *Phil. Mag.* **A65**, 439, Figs. 3a, 12a, c, reproduced by permission of Taylor and Francis.
- Figure 27.10: Courtesy of J. Zhu.
- Figure 27.12: Modified from Vincent, R. (1969) *Phil. Mag.* **19**, 1127, Fig. 4.
- Figure 27.13: Modified from Norton, M.G. and Carter, C.B. (1995) *J. Mat. Sci.* **30**, Fig. 6.
- Figure 27.14: Courtesy of U. Dahmen, from Hetherington, C.J.D. and Dahmen, U. (1992) in Hawkes, P.W. (Ed.) *Signal and Image Processing in Microscopy and Microanalysis, Scanning Microscopy Supplement* **6**, 405, Fig. 9, reproduced by permission of Scanning Microscopy International.
- Figure 27.15: From Heidenreich, R.D. (1964) *Fundamentals of Transmission Electron Microscopy*, Figs. 5.4, 5.6, reproduced by permission of John Wiley & Sons Inc.

- Figure 27.16A: From Heidenreich, R.D. (1964) *Fundamentals of Transmission Electron Microscopy*, Fig. 11.2, reproduced by permission of John Wiley & Sons Inc.
- Figure 27.16B: From Boersch, H., et al. (1962) *Z. Phys.* **167**, 72, Fig. 4, reproduced by permission of Springer-Verlag.
- Figure 27.17: Courtesy of M. Rühle.
- Figure 27.18: Modified from Kouh, Y.M., et al. (1986) *J. Mat. Sci.* **21**, 2689, Fig. 9.
- Figure 27.19: Courtesy of M. Rühle, from Rühle, M. and Sass, S.L. (1984) *Phil. Mag.* **A49**, 759, Fig. 2, reproduced by permission of Taylor and Francis.
- Figure 27.20B–E: From Carter, C.B., et al. (1986), *Phil. Mag.* **A55**, 21, Fig. 11, reproduced by permission of Taylor and Francis.

Chapter 28

- Figure 28.4: Courtesy of R. Gronsky, from Gronsky, R. (1992) in Williams, D.B., et al. (Eds.) *Images of Materials*, Fig. 7.6, reproduced by permission of Oxford University Press.
- Figure 28.5: Courtesy of S. McKernan.
- Figure 28.6: Courtesy of S. McKernan.
- Figure 28.7: Modified from Cowley, J.M. (1988) in Buseck, P.R., et al. (Eds.) *High-Resolution Electron Microscopy and Associated Techniques*, Fig. 1.9, Oxford University Press.
- Figure 28.8: Courtesy of J.C.H. Spence, from Spence, J.C.H. (1988) *Experimental High-Resolution Electron Microscopy*, 2nd Ed., Fig. 4.3, reproduced by permission of Oxford University Press.
- Figure 28.9: Modified from Rose, H. (1991) in Heydenreich, J. and Neumann, W. (Eds.) *High-Resolution Electron Microscopy—Fundamentals and Applications*, p. 6, Fig. 3, Halle/Saale.
- Figure 28.10: From de Jong, A.F. and Van Dyck, D. (1993) *Ultramicroscopy* **49**, 66, Fig. 1, reproduced by permission of Elsevier Science B.V.
- Figure 28.11: Courtesy of M.T. Otten, from Otten, M.T. and Coene, W.M.J. (1993) *Ultramicroscopy* **48**, 77, Fig. 8, reproduced by permission of Elsevier Science B.V.
- Figure 28.12: Courtesy of M.T. Otten, from Otten, M.T. and Coene, W.M.J. (1993) *Ultramicroscopy* **48**, 77, Fig. 11, reproduced by permission of Elsevier Science B.V.
- Figure 28.13: Courtesy of M.T. Otten, from Otten, M.T. and Coene, W.M.J. (1993) *Ultramicroscopy* **48**, 77, Fig. 10, reproduced by permission of Elsevier Science B.V.
- Figure 28.14A,B: From Amelinckx, S., et al. (1993) *Ultramicroscopy* **51**, 90, Fig. 2, reproduced by permission of Elsevier Science B.V.
- Figure 28.15: From Amelinckx, S., et al. (1993) *Ultramicro-*

- copy* 51, 90, Fig. 3, reproduced by permission of Elsevier Science B.V.
- Figure 28.16: From Rasmussen, D.R., *et al.* (1995) *J. Microsc.* **179**, 77, Figs. 2c, d, reproduced by permission of the Royal Microscopical Society.
- Figure 28.18A: Courtesy of S. McKernan.
- Figure 28.18B: From Berger, A., *et al.* (1994) *Ultramicroscopy* **55**, 101, Fig. 4b, reproduced by permission of Elsevier Science B.V.
- Figure 28.18C: Courtesy of S. Summerfelt.
- Figure 28.18D: Courtesy of S. McKernan.
- Figure 28.19: Courtesy of D.J. Smith.
- Figure 28.21B: From Van Landuyt, J., *et al.* (1991) in Heydenreich, J. and Neumann, W. (Eds.) *High-Resolution Electron Microscopy—Fundamentals and Applications*, p. 254, Fig. 6, reproduced by permission of Halle/Saale.
- Figure 28.21D: From Van Landuyt, J., *et al.* (1991) in Heydenreich, J. and Neumann, W. (Eds.) *High-Resolution Electron Microscopy—Fundamentals and Applications*, p. 254, Fig. 8, reproduced by permission of Halle/Saale.
- Figure 28.22: From Nissen H.-U. and Beeli, C. (1991) in Heydenreich, J. and Neumann, W. (Eds.) *High-Resolution Electron Microscopy—Fundamentals and Applications*, p. 272, Fig. 4, reproduced by permission of Halle/Saale.
- Figure 28.23: From Nissen H.-U. and Beeli, C. (1991) in Heydenreich, J. and Neumann, W. (Eds.) *High-Resolution Electron Microscopy—Fundamentals and Applications*, p. 272, Fig. 2, reproduced by permission of Halle/Saale.
- Figure 28.24: From Parsons, J.R., *et al.* (1973) *Phil. Mag.* **29**, 1359, Fig. 2, reproduced by permission of Taylor and Francis.
- Table 28.1: Modified from de Jong, A.F. and Van Dyck, D. (1993) *Ultramicroscopy* **49**, 66, Table 1.

Chapter 29

- Figure 29.2A,B: Courtesy of M.A. O'Keefe, from O'Keefe, M.A. and Kilaas, R. (1988) in Hawkes, P.W., *et al.* (Eds.) *Image and Signal Processing in Electron Microscopy, Scanning Microscopy Supplement 2*, p. 225, Fig. 1, reproduced by permission of Scanning Microscopy International.
- Figure 29.3: From Kambe, K. (1982) *Ultramicroscopy* **10**, 223, Figs. 1a-d, reproduced by permission of Elsevier Science B.V.
- Figure 29.4: Courtesy of M.A. O'Keefe, from O'Keefe, M.A. and Kilaas, R. (1988) in Hawkes, P.W., *et al.* (Eds.) *Image and Signal Processing in Electron Microscopy, Scanning Microscopy Supplement 2*, p. 225, Fig. 4, re-

- produced by permission of Scanning Microscopy International.
- Figure 29.5: Modified from Rasmussen, D.R. and Carter, C.B. (1990) *Ultramicroscopy* **32**, 337, Figs. 1 and 2.
- Figure 29.8: From Beeli, C. and Horiuchi, S. (1994) *Phil. Mag.* **B70**, 215, Figs. 6a-d, reproduced by permission of Taylor and Francis.
- Figure 29.9: From Beeli, C. and Horiuchi, S. (1994) *Phil. Mag.* **B70**, 215, Figs. 7a-d, reproduced by permission of Taylor and Francis.
- Figure 29.10: From Beeli, C. and Horiuchi, S. (1994) *Phil. Mag.* **B70**, 215, Fig. 8, reproduced by permission of Taylor and Francis.
- Figure 29.11: From Jiang, J., *et al.* (1995) *Phil. Mag. Lett.* **71**, 123, Fig. 4, reproduced by permission of Taylor and Francis.

Chapter 30

- Figure 30.1: Courtesy of J. Heffelfinger.
- Figure 30.2: From Rasmussen, D.R., *et al.* (1995) *J. Microsc.* **179**, 77, Fig. 1b, reproduced by permission of The Royal Microscopical Society.
- Figure 30.3: From Rasmussen, D.R., *et al.* (1995), *J. Microsc.* **179**, 77, Fig. 5, reproduced by permission of The Royal Microscopical Society.
- Figure 30.4: Courtesy of O.L. Krivanek, from Krivanek, O.L. (1988) in Buseck, P.R., *et al.* (Eds.) *High-Resolution Electron Microscopy and Associated Techniques*, Fig. 12.6, reproduced by permission of Oxford University Press.
- Figure 30.5: Courtesy of O.L. Krivanek, from Krivanek, O.L. (1988) in Buseck, P.R., *et al.* (Eds.) *High-Resolution Electron Microscopy and Associated Techniques*, Fig. 12.7, reproduced by permission of Oxford University Press.
- Figure 30.6A: Courtesy of J.C.H. Spence, from Spence, J.C.H. and Zuo, J.M. (1992) *Electron Microdiffraction*, Fig. A1.3, reproduced by permission of Plenum Press.
- Figure 30.6B: Courtesy of O.L. Krivanek, from Krivanek, O.L. (1988) in Buseck, P.R., *et al.* (Eds.) *High-Resolution Electron Microscopy and Associated Techniques*, Fig. 12.8, reproduced by permission of Oxford University Press.
- Figure 30.7: Courtesy of S. McKernan.
- Figure 30.8: Courtesy of Z.C. Lin, from Lin, Z.C. (1993) Ph.D. dissertation, Fig. 4.15, University of Minnesota.
- Figure 30.9: Courtesy of O. Saxton, from Kirkland, A.I. (1992) in Hawkes, P.W. (Ed.) *Signal and Image Processing in Microscopy and Microanalysis, Scanning Microscopy Supplement 6*, 139, Figs. 1, 2, 3, reproduced by permission of Scanning Microscopy International.

- Figure 30.10: From Zou, X.D. and Hovmöller, S. (1993) *Ultramicroscopy* **49**, 147, Fig. 1, reproduced by permission of Elsevier Science B.V.
- Figure 30.11A: From Kirkland, A.I., et al. (1995) *Ultramicroscopy* **57**, 355, Fig. 1, reproduced by permission of Elsevier Science B.V.
- Figure 30.11B: From Kirkland, A.I., et al. (1995) *Ultramicroscopy* **57**, 355, Fig. 3, reproduced by permission of Elsevier Science B.V.
- Figure 30.12A–C: From Kirkland, A.I., et al. (1995) *Ultramicroscopy* **57**, 355, Fig. 8, reproduced by permission of Elsevier Science B.V.
- Figure 30.13: Courtesy of O.L. Krivanek, from Krivanek, O.L. and Fan, G.Y. (1992) in Hawkes, P.W. (Ed.) Signal and Image Processing in Microscopy and Microanalysis, *Scanning Microscopy Supplement* **6**, p. 105, Fig. 4, reproduced by permission of Scanning Microscopy International.
- Figure 30.14: Courtesy of O.L. Krivanek, from Krivanek, O.L. and Fan, G.Y. (1992) in Hawkes, P.W. (Ed.) Signal and Image Processing in Microscopy and Microanalysis, *Scanning Microscopy Supplement* **6**, p. 105, Fig. 5, reproduced by permission of Scanning Microscopy International.
- Figure 30.15: Courtesy of U. Dahmen, from Paciornik, S., et al. (1996) *Ultramicroscopy* **62**, 15, Fig. 1, reproduced by permission of Elsevier Science B.V.
- Figure 30.16: Courtesy of U. Dahmen, from Paciornik, S., et al. (1996) *Ultramicroscopy* **62**, 15, Fig. 5, reproduced by permission of Elsevier Science B.V.
- Figure 30.17: Courtesy of A. Ourmazd, from Kisielowski, C., et al. (1995) *Ultramicroscopy* **58**, 131, Figs. 2–4, reproduced by permission of Elsevier Science B.V.
- Figure 30.18: Courtesy of A. Ourmazd, from Kisielowski, C., et al. (1995) *Ultramicroscopy* **58**, 131, Figs. 8, 10, 12, reproduced by permission of Elsevier Science B.V.
- Figure 30.19A–D: Courtesy of A. Ourmazd, from Ourmazd, A., et al. (1990) *Ultramicroscopy* **34**, 237, Figs. 1, 1, 2, 5, reproduced by permission of Elsevier Science B.V.
- Figure 30.20A–F: Courtesy of A. Ourmazd, from Kisielowski, C., et al. (1995) *Ultramicroscopy* **58**, 131, Figs. 15a–f, reproduced by permission of Elsevier Science B.V.
- Figure 30.21: Courtesy of U. Dahmen, from Paciornik, S., et al. (1996) *Ultramicroscopy*, in press, Fig. 2, reproduced by permission of Elsevier Science B.V.
- Figure 30.22: From King, W.E. and Campbell, G.H. (1994) *Ultramicroscopy* **56**, 46, Fig. 1, reproduced by permission of Elsevier Science B.V.
- Figure 30.23: From King, W.E. and Campbell, G.H. (1994) *Ultramicroscopy* **56**, 46, Fig. 6, reproduced by permission of Elsevier Science B.V.

- Figure 30.24: Courtesy of M. Rühle, from Möbus, G., et al. (1993) *Ultramicroscopy* **49**, 46, Fig. 6, reproduced by permission of Elsevier Science B.V.
- Figure 30.25: From Thon, F. (1970) in Valdrè, U. (Ed.) *Electron Microscopy in Materials Science*, p. 571, Fig. 36, reproduced by permission of Academic Press.
- Figure 30.26: Courtesy of J. Heffelfinger.

Chapter 31

- Figure 31.2: Courtesy of R. Sinclair, from Sinclair, R., et al. (1981) *Met. Trans.* **12A**, 1503, Figs. 13, 14, reproduced by permission of ASM International.
- Figure 31.4A,B: From Marcinkowski, M.J. and Poliak, R.M. (1963) *Phil. Mag.* **8**, 1023, Figs. 1a, b, reproduced by permission of Taylor and Francis.
- Figure 31.4C,D: Courtesy of J. Silcox, from Silcox, J. (1963) *Phil. Mag.* **8**, 7, Fig. 7, reproduced by permission of Taylor and Francis.
- Figure 31.5: Courtesy of A.J. Craven, from Buggy, T.W., et al. (1981) *Analytical Electron Microscopy—1981*, p. 231, Fig. 5, reproduced by permission of San Francisco Press.
- Figure 31.6D,E: Courtesy of NSA Hitachi Scientific Instruments Ltd. and S. McKernan.
- Figure 31.7: Courtesy of R. Sinclair.
- Figure 31.8: From Kuesters, K.-H., et al. (1985) *J. Cryst. Growth* **71**, 514, Fig. 4, reproduced by permission of Elsevier Science, B.V.
- Figure 31.9: Courtesy of M. Mallamaci.
- Figure 31.10A: From De Cooman, B.C., et al. (1985) *J. Electron Microsc. Tech.* **2**, 533, Fig. 1, reproduced by permission of John Wiley & Sons Inc.
- Figure 31.10B: Courtesy of S.M. Zemyan.
- Figure 31.10C–E: Courtesy of B.C. De Cooman.
- Figure 31.12: Courtesy of G. Thomas, from Bell, W.L. and Thomas, G. (1972) in Thomas G., et al. (Eds.) *Electron Microscopy and Structure of Materials*, p. 53, Fig. 28, reproduced by permission of University of California Press.
- Figure 31.13: Courtesy of K.-R. Peters, from Peters, K.-R. (1984) in Kyser, D.F., et al. (Eds.) *Electron Beam Interactions with Solids for Microscopy, Microanalysis and Lithography*, p. 363, Fig. 1, reproduced by permission of Scanning Microscopy International.
- Figure 31.14: Courtesy of R. McConvilie, from Williams, D.B. (1987) *Practical Analytical Electron Microscopy in Materials Science*, 2nd Edition, Fig. 3.11, reproduced by permission of Philips Electron Optics.
- Figure 31.15: Courtesy of Philips Electronic Instruments, from Williams, D.B. (1987) *Practical Analytical Electron Microscopy in Materials Science*, 2nd Edition, Fig.

- 3.10, reproduced by permission of Philips Electron Optics.
- Figure 31.16: Courtesy of H. Lichte, from Lichte, H. (1992) *Scanning Microscopy*, p. 433, Fig. 1, reproduced by permission of Scanning Microscopy International.
- Figure 31.17: Modified from Lichte, H. (1992) *Ultramicroscopy* **47**, 223, Fig. 1.
- Figure 31.18: Modified from Tonomura, A.: Courtesy of NSA Hitachi Scientific Instruments Ltd.
- Figure 31.19A–C: From Tonomura, A. (1992) *Adv. Phys.* **41**, 59, Fig. 29, reproduced by permission of Taylor and Francis.
- Figure 31.19D: From Tonomura, A. (1987) *Rev. Mod. Phys.* **59**, 639, Fig. 41, reproduced by permission of The American Physical Society.
- Figure 31.20A: From Tonomura, A. (1992) *Adv. Phys.* **41**, 59, Fig. 38, reproduced by permission of Taylor and Francis.
- Figure 31.20B: From Tonomura, A. (1992) *Adv. Phys.* **41**, 59, Fig. 42, reproduced by permission of Taylor and Francis.
- Figure 31.20C: From Tonomura, A. (1992) *Adv. Phys.* **41**, 59, Fig. 44, reproduced by permission of Taylor and Francis.
- Figure 31.21: Courtesy of R. Sinclair, from Sinclair, R., et al. (1994) *Ultramicroscopy* **56**, 225, Fig. 5, reproduced by permission of Elsevier Science B.V.
- Figure 32.1: Courtesy of J.E. Yehoda, from Messier, R and Yehoda, J.E. (1985) *J. Appl. Phys.* **58**, 3739, Fig. 1, reproduced by permission of the American Institute of Physics.
- Figure 32.2: Courtesy of S.M. Zemyan.
- Figure 32.3B: Courtesy of JEOL USA Inc.
- Figure 32.4: Modified from Woldseth, R. (1973) *X-ray Energy Spectrometry*, Kevex Instruments.
- Figures 32.5–8: Courtesy of S.M. Zemyan.
- Figure 32.10: Courtesy of S. M. Zemyan, from Zemyan, S. and Williams, D.B. (1995) in Williams, D.B., et al. (Eds.) *X-ray Spectrometry in Electron Beam Instruments*, Fig. 12.9, reproduced by permission of Plenum Press.
- Figure 32.11: Courtesy of S. M. Zemyan, from Zemyan, S. and Williams, D.B. (1995) in Williams, D.B., et al. (Eds.) *X-ray Spectrometry in Electron Beam Instruments*, Fig. 12.10, reproduced by permission of Plenum Press.
- Figure 32.12A: Courtesy of J.J. Friel, from Mott, R.B. and Friel, J.J. (1995) in Williams, D.B., et al. (Eds.) *X-ray Spectrometry in Electron Beam Instruments*, Fig. 9.8, reproduced by permission of Plenum Press.
- Figure 32.12B: Courtesy of C.E. Lyman, from Lyman C.E., et al. (1994) *J. Microsc.* **176**, 85, Fig. 9, reproduced by permission of the Royal Microscopical Society.
- Figure 32.13: Courtesy of S.M. Zemyan.
- Figure 32.14: Courtesy of S.M. Zemyan.
- Figure 32.15: Courtesy of D.E. Newbury, from Newbury, D.E. (1995) in Williams, D.B., et al. (Eds.) *X-ray Spectrometry in Electron Beam Instruments*, Fig. 11.18, reproduced by permission of Plenum Press.
- Figure 32.16: Courtesy of J.I. Goldstein, from Goldstein, J.I., et al. (1992) *Scanning Electron Microscopy and X-ray Microanalysis*, 2nd edition, Fig. 5.3, reproduced by permission of Plenum Press.
- Figure 32.17A,B: Courtesy of S.M. Zemyan.

Chapter 33

- Figure 33.1: From Williams, D.B. (1987) *Practical Analytical Electron Microscopy in Materials Science*, 2nd Edition, Fig. 4.5a, reproduced by permission of Philips Electron Optics.
- Figure 33.2: Courtesy of W.A.P. Nicholson, from Nicholson, W.A.P., et al. (1982), *J. Microsc.* **125**, 25, Fig. 4, reproduced by permission of the Royal Microscopical Society.
- Figure 33.3: From Williams, D.B. (1987) *Practical Analytical Electron Microscopy in Materials Science*, 2nd Edition, Fig. 4.30, reproduced by permission of Philips Electron Optics.
- Figure 33.4: Courtesy of S.M. Zemyan.
- Figure 33.5A,B: Courtesy of G. Cliff, from Cliff, G. and Kenway, P.B. (1982) *Microbeam Analysis—1982*, p. 107, Figs. 5, 4, reproduced by permission of San Francisco Press.
- Figure 33.6: Modified from Williams D.B. and Goldstein, J.I. (1981) in Heinrich, K.F.J., et al. (Eds.) *Energy-Dispersive X-ray Spectrometry*, p. 346, Fig. 7a, NBS.
- Figure 33.7: Courtesy of S.M. Zemyan.
- Figure 33.8: Courtesy of S.M. Zemyan.
- Figure 33.9A: Courtesy of S.M. Zemyan.
- Figure 33.9B: Courtesy of K.S. Vecchio, from Vecchio, K.S. and Williams, D.B. (1987) *J. Microsc.* **147**, 15, Fig. 1, reproduced by permission of the Royal Microscopical Society.
- Figure 33.10A: Courtesy of S.M. Zemyan.
- Figure 33.10B: Courtesy of S.M. Zemyan, from Zemyan, S. and Williams, D.B. (1994) *J. Microsc.* **174**, 1, Fig. 6, reproduced by permission of the Royal Microscopical Society.

Chapter 34

- Figures 34.1–5: Courtesy of S.M. Zemyan.

Chapter 35

Figures 35.1–4: Courtesy of S.M. Zemyan.

Figure 35.5A: From Williams, D.B. (1987) *Practical Analytical Electron Microscopy in Materials Science*, 2nd Edition, Fig. 4.20, reproduced by permission of Philips Electron Optics.

Figure 35.5B,C: Courtesy of S.M. Zemyan.

Figure 35.6: Courtesy of S.M. Zemyan.

Figure 35.7: From Wood, J.E., et al. (1984) *J. Microsc.* **133**, 255, Figs. 2, 8, reproduced by permission of the Royal Microscopical Society.

Figure 35.8: From Bender, B.A., et al. (1980) *J. Amer. Ceram. Soc.* **63**, 149, Fig. 1, reproduced by permission of the American Ceramic Society.

Figure 35.10: Courtesy of S. Vivekenand and K. Barmak.

Figure 35.11A: Courtesy of J.A. Eades, from Christenson, K.K. and Eades, J.A. (1986) *Proc. 44th EMSA Meeting*, p. 622, Fig. 2, reproduced by permission of MSA.

Figure 35.12: Courtesy of R. Ayer, from M. Raghavan, et al. (1984) *Met. Trans.* **15A**, 783, Figs. 4, 11, reproduced by permission of ASM International.

Figure 35.13: Courtesy of A.W. Nicholls, from Nicholls, A.W. and Jones, I.P. (1983) *J. Chem. Phys.* **44**, 671, Figs. 3, 6a, reproduced by permission of The American Physical Society.

Figure 35.14A: Courtesy of V.J. Keast.

Figure 35.14B: Courtesy of J.R. Michael, from Michael J.R. and Williams, D.B. (1987) *Met. Trans.* **15A**, Fig. 7, Reproduced by permission of ASM International.

Figure 35.15: Courtesy of C.E. Lyman, from Lyman C.E. (1986) *Ultramicroscopy* **20**, 119, Figs. 1b, c, reproduced by permission of Elsevier Science B.V.

Tables 35.1, 35.2: From Williams, D.B. (1987) *Practical Analytical Electron Microscopy in Materials Science*, 2nd Edition, Tables 4.2a, b, reproduced by permission of Philips Electron Optics.

Tables 35.3A,B: From Wood, J.E., et al. (1984) *J. Microsc.* **133**, 255, Tables 9,11, reproduced by permission of the Royal Microscopical Society.

Chapter 36

Figure 36.1A,B: Courtesy of V.J. Keast.

Figure 36.2: Courtesy of J.R. Michael, from Williams D.B., et al. (1992) *Ultramicroscopy* **47**, 121, Fig. 1, reproduced by permission of Elsevier Science B.V.

Figure 36.3: Courtesy of J.R. Michael, from Williams D.B., et al. (1992) *Ultramicroscopy* **47**, 121, Fig. 2, reproduced by permission of Elsevier Science B.V.

Figure 36.4: Courtesy of R. Ayer, from Michael, J.R., et al. (1989) *J. Microsc.* **160**, 41, Fig. 2, reproduced by permission of the Royal Microscopical Society.

Figure 36.5.: Courtesy of R. Ayer, from Michael, J.R., et al. (1989) *J. Microsc.* **160**, 41, Figs. 3, 4, reproduced by permission of the Royal Microscopical Society.

Figure 35.8A,B: From Williams, D.B. (1987) *Practical Analytical Electron Microscopy in Materials Science*, 2nd Edition, Fig. 4.27, reproduced by permission of Philips Electron Optics.

Figure 36.9: Courtesy of C.E. Lyman, modified from Lyman C.E. (1987) in Kirschner, J., et al. (Eds.) *Physical Aspects of Microscopic Characterization of Materials*, p. 123, Fig. 1, Scanning Microscopy International.

Figure 36.10: Courtesy of C.E. Lyman, modified from Lyman C.E. (1987) in Kirschner, J., et al. (Eds.) *Physical Aspects of Microscopic Characterization of Materials* p. 123, Fig. 7, Scanning Microscopy International.

Chapter 37

Figure 37.1: Courtesy of R.F. Egerton, modified from Egerton, R.F. (1996) *Electron Energy-Loss Spectroscopy in the Electron Microscope*, 2nd edition, Fig. 2.2, Plenum Press.

Figure 37.2: Courtesy of Gatan Inc.

Figure 37.3: Courtesy of D.C. Joy, from Joy, D.C. in Joy, D.C., et al. (Eds.) (1986) *Principles of Analytical Electron Microscopy*, Fig. 5, p. 259, reproduced by permission of Plenum Press.

Figure 37.4: Courtesy of J. Bruley.

Figure 37.5: Courtesy of Gatan Inc.

Figure 37.6: Courtesy of J.A. Hunt, from Hunt, J.A. and Williams, D.B. (1994) *Acta Microsc.* **3**, 1, Fig. 7, reproduced by permission of the Venezuelan Society for Electron Microscopy.

Figure 37.10: Courtesy of R.F. Egerton, from Egerton, R.F., et al. (1993) *Ultramicroscopy* **48**, 239, Fig. 2, reproduced by permission of Elsevier Science B.V.

Figure 37.11: Courtesy of O.L. Krivanek, modified from Krivanek, O.L., et al. (1991) *Microsc. Microanal. Microstruct.* **2**, p. 315, Fig. 8.

Chapter 38

Figures 38.1–3: Courtesy of J. Bruley.

Figure 38.4: Courtesy of O.L. Krivanek, modified from Ahn, C.C. and Krivanek, O.L. (1983) *EELS Atlas* p. iv, Gatan Inc.

Figure 38.5: Courtesy of J. Bruley, modified from Joy, D.C. (1986) in Joy D.C., et al. (Eds.) *Principles of Analytical Electron Microscopy*, p. 249, Fig. 8, Plenum Press.

Figure 38.6: Courtesy of J. Bruley.

Figure 38.7: Courtesy of C.E. Lyman, from Lyman C.E. (1987) in Kirschner, J., et al. (Eds.) *Physical Aspects of Microscopic Characterization of Materials*, p. 123, Fig.

- 2, reproduced by permission of Scanning Microscopy International.
- Figure 38.8: Courtesy of D.C. Joy, modified from Joy, D.C. in Hren, J.J., et al. (Eds.) (1979) *Introduction to Analytical Electron Microscopy*, p. 235, Fig. 7.6, Plenum Press.
- Figure 38.9: Courtesy of M. Kundmann.
- Figure 38.10: Courtesy of J.A. Hunt, from Hunt, J.A. and Williams, D.B. (1994) *Acta Microsc.* **3**, 1, Fig. 5, reproduced by permission of the Venezuelan Society for Electron Microscopy.
- Figure 38.11: Courtesy of J.A. Hunt, from Hunt, J.A. and Williams, D.B. (1994) *Acta Microsc.* **3**, 1, Fig. 4, reproduced by permission of the Venezuelan Society for Electron Microscopy.
- Figure 38.12: Courtesy of J. Bruley, from Hunt, J.A. and Williams, D.B. (1994) *Acta Microsc.* **3**, 1, Fig. 6, reproduced by permission of the Venezuelan Society for Electron Microscopy.
- Table 38.2: Courtesy of R.F. Egerton, from Egerton R.F. (1996) *Electron Energy-Loss Spectroscopy in the Electron Microscope*, 2nd edition, p. 157, Table 3.2, reproduced by permission of Plenum Press.
- ## Chapter 39
- Figure 39.1: Courtesy of J. Bruley.
- Figure 39.2: Courtesy of K. Sato and Y. Ishiguro, modified from Sato K. and Ishiguro Y. (1996) *Materials Transactions Japan Institute of Metals* **37**, 643, Figs. 1 and 7.
- Figure 39.3: Courtesy of J. Bruley.
- Figure 39.4: Courtesy of J.A. Hunt, from Hunt, J.A. and Williams, D.B. (1994) *Acta Microsc.* **3**, 1, Fig. 14, reproduced by permission of the Venezuelan Society for Electron Microscopy.
- Figure 39.5: Courtesy of J.A. Hunt, from Williams, D.B. and Goldstein, J.I. (1992) *Microbeam Analysis* **1**, 29, Fig. 11, reproduced by permission of VCH.
- Figure 39.6: Courtesy of J.A. Hunt, from Hunt, J.A. and Williams, D.B. (1994) *Acta Microsc.* **3**, 1, Fig. 17a, reproduced by permission of the Venezuelan Society for Electron Microscopy.
- Figure 39.7: Courtesy of J.A. Hunt, from Hunt, J.A. and Williams, D.B. (1994) *Acta Microsc.* **3**, 1, Fig. 17b, reproduced by permission of the Venezuelan Society for Electron Microscopy.
- Figure 39.8: Courtesy of D.C. Joy, from Joy, D.C. in Joy, D.C., et al. (Eds.) (1986) *Principles of Analytical Electron Microscopy*, p. 288, Figs. 6,7, reproduced by permission of Plenum Press.
- Figure 39.9: Courtesy of R.F. Egerton, modified from Egerton R.F. (1993) *Ultramicroscopy* **50**, Fig. 6.
- Figure 39.10: From Liu D.R. and Williams, D.B. (1989) *Proc. Roy. Soc. (London)* **A425**, Fig. 7, reproduced by permission of The Royal Society.
- Figure 39.11: Courtesy of J. Bruley.
- Figure 39.12: Courtesy of D.C. Joy, from Joy, D.C. in Joy, D.C., et al. (Eds.) (1986) *Principles of Analytical Electron Microscopy*, p. 293, Fig. 10, reproduced by permission of Plenum Press.
- Figures 39.13, 14, 15: Courtesy of J. Bruley.
- Figure 39.16: Courtesy of J.A. Hunt, from Hunt, J.A. and Williams, D.B. (1994) *Acta Microsc.* **3**, 1, Fig. 16, reproduced by permission of the Venezuelan Society for Electron Microscopy.
- Figure 39.17: Courtesy of R.F. Egerton, from Egerton, R.F. (1996) *Electron Energy-Loss Spectroscopy in the Electron Microscope*, 2nd edition, Fig. 1.11, reproduced by permission of Plenum Press.
- Figure 39.18: Courtesy of O.L. Krivanek, modified from Krivanek, O.L., et al. (1991), *Microsc. Microanal. Microstruc.* **2**, 257, Fig. 5.
- ## Chapter 40
- Figure 40.4: Courtesy of N.J. Zaluzec, modified from Zaluzec, N.J. (1982) *Ultramicroscopy* **9**, 319, Fig. 3.
- Figure 40.5A,B: Courtesy of J. Bruley.
- Figure 40.5C: Courtesy of P.E. Batson, from Batson, P.E. (1993) *Nature* **366**, 727, Fig. 1, reproduced by permission of Macmillan Journals Ltd.
- Figure 40.7: Courtesy of R. Brydson, modified from Hansen, P.L., et al. (1994) *Microsc. Microanal. Microstruc.* **5**, 173, Figs. 1, 2.
- Figure 40.8: Courtesy of J. Bruley.
- Figure 40.9: From Williams D.B. and Edington, J.W. (1976) *Acta Met.* **24**, 323, Fig. 7, reproduced by permission of Elsevier Science B.V.
- Figure 40.9C: Courtesy of A.J. Strutt.
- Figure 40.10A,B: Courtesy of J. Bruley.
- Figure 40.10C: Courtesy of J.A. Hunt from Hunt J.A. and Williams, D.B. (1991) *Ultramicroscopy* **38**, 47, Fig. 11, reproduced by permission of Elsevier Science B.V.
- Figure 40.11: Courtesy of J. Bruley, from Müllejans H., et al. (1993) *Electron Microscopy and Analysis—1993*, p. 62, Fig. 4, reproduced by permission of the Institute of Physics Publishing.
- Figures 40.12, 13: Courtesy of J.A. Hunt.
- Figure 40.14: Courtesy of J. Bruley and J. Mayer.
- Figure 40.15: Courtesy of J.C.H. Spence and J. Mayer, from Mayer, et al. (1991) *Proc. 49th EMSA Meeting*, p. 787, Figs. 2, 3, San Francisco Press, reproduced by permission of MSA.
- Table 40.1: From Williams D.B. and Edington, J.W. (1976) *J. Microsc.* **108**, 113, Table 1, reproduced by permission of The Royal Microscopical Society.